UNIVERSITY OF CALIFORNIA, MERCED

Effect of lipid membranes on intracellular cargo transport by teams of molecular motors

A dissertation submitted in partial satisfaction of the
requirements for the degree
Doctor of Philosophy

in

Physics

by

Niranjan Sarpangala

Committee in charge:

Professor Linda S. Hirst, Chair
Professor Ajay Gopinathan, Advisor
Professor Kinjal Dasbiswas
Professor Jing Xu

2023

The dissertation of Niranjan Sarpangala is approved, and it is acceptable in quality and form for publication on microfilm and electronically:

(Professor Ajay Gopinathan, Advisor)

(Professor Kinjal Dasbiswas)

(Professor Jing Xu)

(Professor Linda S. Hirst, Chair)

University of California, Merced

2023

DEDICATION

To Amma and Appa

EPIGRAPH

"Where the mind is without fear and the head is held high;
Where knowledge is free;
Where the world has not been broken up into fragments by narrow domestic walls;
...
Into that heaven of freedom, my Father, let our world awake."
— Rabindranath Tagore, Gitanjali

TABLE OF CONTENTS

Signature Page . . . iii

Dedication . . . iv

Epigraph . . . v

Table of Contents . . . vi

List of Figures . . . ix

List of Tables . . . xxvi

Acknowledgements . . . xxvii

Curriculum Vitae . . . xxx

Abstract . . . xxxvii

Chapter 1 Introduction . . . 1
1.1 Transport of materials in cells . . . 1
1.2 Active transport using molecular motors . . . 2
1.3 Multi-motor transport . . . 3
1.4 Effect of lipid membranes on multi-motor transport . . . 4
1.5 Outline . . . 5

Chapter 2 Computational Model . . . 9
2.1 Introduction . . . 9
2.2 Brownian dynamics model of cargo transport by teams of motors . . . 11
2.3 Conclusions . . . 16

Notes . . . 19
2.A Notes on the assumptions in the computational model . . . 19
2.A.1 We neglect the deformation of vesicle due to motor forces. . . . 19
2.A.2 Estimation of rotational diffusion of cargo. . . . 20

Chapter 3 Effect of surface fluidity on cargo transport by identical motor teams . . . 23
3.1 Introduction . . . 23
3.2 Results and Discussion . . . 29
3.2.1 Surface fluidity reduces negative interference between bound kinesin motors . . . 29

3.2.2 On-rate of a motor increases with the number of bound motors for fluid cargo . . . 33
3.2.3 Surface fluidity increases the availability of motors for binding . . . 36
3.2.4 Fluid cargo have longer run lengths than rigid cargo 40
3.2.5 Contributions of different effects to overall run length . . . 41
3.2.6 Motor teams under external load . . . 44
3.3 Conclusion . . . 49

Notes . . . 54
3.A Estimation of relevant timescales . . . 54
3.A.1 τ_{bind} and τ_{off} . . . 54
3.A.2 Conditional on-rate . . . 55
3.B Analytical estimation of run length for a rigid cargo . . . 57
3.C Discussion on how the runlength of cargo can be different even though the average number of motors is the same . 58
3.D Details of different force-related metrics used to characterize negative interference . . . 59
3.E Supplementary Figures . . . 63

Chapter 4 Heterogenous teams of motors on the cargo . . . 80
4.1 Introduction . . . 80
4.2 Methods . . . 82
4.3 Results and Discussions . . . 84
4.3.1 Heterogeneity is essential to explain experimentally observed differences in rigid and lipid cargo velocities . . . 84
4.3.2 Enhanced lipid cargo velocity is explained by delay in strain generation between slow and fast. . . 87
4.3.3 Runlengths increase as the fraction of slow motors increases. . . . 92
4.4 Conclusion . . . 95

Notes . . . 98
4.A Supplementary Figures . . . 98

Chapter 5 Cargo transport across roadblocks . . . 104
5.1 Introduction . . . 104
5.2 Results and Discussions . . . 106
5.2.1 Lipid membranes have negligible influence on the probability of small kinesin teams crossing single-binding-site-sized roadblocks. . . . 106

5.2.2 Lipid membranes enhance the probability of crossing ringlike roadblocks around microtubules. . . . 111
5.3 Conclusion 116

Notes 121
5.A Runlength decreases non-linearly as a function of roadblock probability P 121
5.B Approximate Probability of Crossing Hurdle 122
5.C Supplementary Figures 124

Chapter 6 Three-dimensional microtubule structure and motor properties 126
6.1 Introduction 126
6.2 Results and Discussion 128
6.2.1 Implementation of 3d microtubule lattice 128
6.2.2 Dependence of on-rate with distance from microtubule is sensitive to the mechanical model of kinesin. 129
6.3 Conclusions 130

Notes 135
6.A Time taken for cargo to rotate by 90^o around microtubule due to entropic force of motor. 135

Chapter 7 Conclusion and Future Directions 136

Bibliography 141

LIST OF FIGURES

Figure 1.1: Cartoon of molecular motor carrying a lipid cargo and walking on a filament. Created with BioRender.com 2

Figure 1.2: **Electron micrograph images showing evidence for multi-motor transport in cells.** Mitochondria with 1, 2 and 4 microtubule bound motors. Scale bar = 0.1 μm. Reprinted with permissions from Ashkin et. al., *Nature*, 1990. [11] 3

Figure 2.1: **Schematic of the model.** X is the center of mass of the cargo, A_i and H_i represent motor anchor and motor head positions. Motors exert spring like forces only when their lengths L_i exceed their rest length L_{mot}. Here, motor 1 experiences a hindering load (f_1 is negative), while motor 2 experiences an assistive force (f_2 is positive). Microtubule is modeled as a one-dimensional line. Cargo is an undeformable sphere. Motor anchor positions, A_i diffuse on the cargo surface. 10

Figure 2.2: **The flow chart of the simulation.** The cargo is held near the microtubule until at least one motor is bound. Once a motor is bound, we loop over the series of steps shown in the middle until either all motors are unbound or maximum time is reached. At regular time intervals, we record relevant data like the cargo center of mass, anchor positions of motors on cargo surface, head positions of bound motors on the microtubule. . . 17

Figure 2.A.1: **Benchmark test to verify correct implementation of rotational diffusion.** We ran simulations of cargo dynamics with just rotational diffusion (no motor bound to MT, no translational diffusion of cargo, no diffusion of motor on cargo surface) and measured the mean-squared-angular-displacement (MSAD, $< \Delta\vec{\Theta}^2 >$) of motor anchor point. Ensemble size = 200. Then we fit MSAD to $4D_R t$ and extracted the rotational diffusion constant, D_R, to verify that we implement the desired rotational diffusion. 22

Figure 3.1.1: **Schematics of cargoes considered in the study. (a)** Rigid cargo (membrane-free cargo). Molecular motors are permanently attached to random locations on the cargo surface. **(b)** Fluid/Lipid cargo (membrane-enclosed cargo). Molecular motors diffuse on the cargo surface. Inset of Fig. 1(b) The lipid bilayer that forms the fluid cargo surface. Reprinted with permissions from Sarpangala and Gopinathan, *PLos Comput. Biol.*, 2022 [125]. CC-BY-4.0. 26

Figure 3.2.0: **Surface fluidity reduces the negative interference between bound kinesin motors which leads to reduction in motor off-rate.** **(a)** Typical trajectories for a rigid (top row) and a lipid cargo (second row). Motor head position subplots (middle column) include the x-positions of the center of mass of cargo (black lines) and head positions of motors on the microtubule (colored lines). The corresponding x-component of motor anchor positions (right column) on the cargo are also shown. **(b)** Distributions of the absolute magnitude of the force experienced by motors in rigid and lipid cargoes (including without cargo rotation) at a fixed number of bound motors ($n = 3$). Distribution for singly bound motor carrying a rigid cargo is also shown for comparison. We first collect $S = 10000$ force values randomly drawn from 200 cargo runs. We then bootstrap this (bootstrap sample size = 1,000 and the number of bootstrap samples = 10) to get the mean distribution and standard error of the mean. **(c)** Distribution of magnitude of motor forces when they specifically experience hindering loads ($f < 0$) and assistive loads ($f > 0$). Cartoon inside shows a possible scenario where the colored motor experiences hindering and assistive load. **(d)** The mean variance of forces among bound motors in rigid ($D = 0$) and lipid cargoes ($D = 1\,\mu m^2 s^{-1}$) with (triangles) and without cargo rotation (circles). Mean variance was calculated as $\frac{1}{S}\sum_{i=1}^{S}\sigma^2_{|f|}(i)$ where the summation is over all the sample time points when the number of bound motors is n. $\sigma^2_{|f|}(i)$ is the variance in the magnitude of force experienced by the n bound motors at i^{th} sample. Sample size $S = 10000$ drawn from 200 cargo runs. **(e)** Mean value of the correlation between the x-components of motor forces, $\langle F_x^j F_x^k \rangle$, averaged over motor pairs and time points with (triangles) and without cargo rotation (circles). Sample size $S = 10000$ drawn from 200 cargo runs. **(f)** Average value of motor off-rate as a function of fluidity of cargo surface with (triangles) and without cargo rotation (circles). ($S = 580$ from 200 cargo runs). Data for all the plots were obtained from the simulation of transport of cargoes with $N = 16$ motors at high ATP concentration of 2 mM. Data sampling rate was 100 s^{-1}. Reprinted with permissions from Sarpangala and Gopinathan, *PLos Comput. Biol.*, 2022 [125]. CC-BY-4.0. 28

Figure 3.2.1: **On-rate of a motor increases with the number of bound motors for fluid cargo. (a)** Average measured distance (H) of the center of mass of cargo from MT as a function of the number of bound motors and fluidity. Horizontal line indicates the height below which the cargo experiences steric interaction from the MT. Data were obtained from the simulation of transport of cargoes with $N = 16$ motors at high ATP concentration of 2 mM. Data sampling rate was 100 s^{-1}. **(b)** Computational measurements of single motor on-rate (green diamonds) and analytical approximation (black dashed line with diamond). ($D = 1\,\mu m^2 s^{-1}$, $S = 10000$) using the cargo height for a given n from the data in (a). Error bars for all plots represent the standard error of the mean. Rotation of cargo was not considered in the on-rate measurement simulations for (b). Reprinted with permissions from Sarpangala and Gopinathan, *PLos Comput. Biol.*, 2022 [125]. CC-BY-4.0. 34

Figure 3.2.2: **Surface fluidity increases the availability of motors for binding. (a)** Ensemble average of the number of bound motors, $\bar{n}$ as a function of time (s). Error bars represent the standard error of the mean. **(b)** Spatial distribution of the kinesin motors on cargo, computed as the probability of locating motors as a function of the polar angle θ and time, t. θ is the polar angle of the motor, measured with respect to z axis perpendicular to the microtubule and passing through the center of the cargo. Data was obtained from the transport of cargoes with a total of $N = 16$ motors at [ATP]=2 mM. Reprinted with permissions from Sarpangala and Gopinathan, *PLos Comput. Biol.*, 2022 [125]. CC-BY-4.0. 37

Figure 3.2.3: **Fluid cargo have longer run lengths than rigid cargo.** **(a)** Average number bound motors, **(b)** Runlength as a function of diffusivity (D) for two different numbers of motors on the cargo (N) and three different ATP concentrations. 200 cargo runs were considered for each parameter set. Error bars represent the standard error of the mean (SEM). The average number of bound motors in (a) was calculated as the mean of the number of bound motors (n) in all time samples (with data sampling rate = 100 s^{-1}) of these 200 cargo runs. Rotational diffusion of cargo was not considered in these simulations. Thus the sample size was large and hence the error bars obtained as the standard error of the mean is very small. **(c)** Comparison between run lengths from our simulations ($N = 4$, [ATP] = 4.9 μM, yellow circles) and analytical estimates (maroon triangle, solid, dashed and dash-dotted lines) as described in the text. *Left cartoon*: A lipid cargo, with access area (S_a, green) and influx area (S_I, yellow) shown. Influx area is defined as the region within $\sqrt{2D\tau_{off}^m}$ from the access area. Reprinted with permissions from Sarpangala and Gopinathan, *PLos Comput. Biol.*, 2022 [125]. CC-BY-4.0. 39

Figure 3.2.4: **Motors dynamically cluster at specific locations on the lipid cargoes.** Average distribution of bound motors on the cargo surface at different hindering loads on the cargo (f_h). Only multiple bound motor cases were considered. Data is from 200 cargo runs with N = 16, high [ATP]= 2 mM with anchor positions of bound motors recorded at a sampling rate of 100 s^{-1}). Anchor positions are measured relative to the body coordinate axis of the cargo (schematic at top-right). Diffusion constant of motors on lipid cargoes was 1 $\mu m^2 s^{-1}$. Reprinted with permissions from Sarpangala and Gopinathan, *PLos Comput. Biol.*, 2022 [125]. CC-BY-4.0. 47

Figure 3.2.5: **Motor teams in fluid cargoes generate higher collective forces.** **(a)** Schematic of the optical trap set up that we used in simulation. **(b)** Rescaled average collective force $\tilde{F_a} = \frac{\left\langle .9513.6 \sum_{i=1}^{N} F_x^i \right\rangle}{NF_s}$ as a function of unloaded motor velocity (v_0) and stall force of motor (F_s) in rigid (left) and lipid (right) cargo. (c) Ratio of $\tilde{F_a}$ between lipid and rigid cargo. 200 cargo runs were used for each parameter set. For each cargo run, data of motor forces for each microtubule bound motors were recorded at a sampling rate of 100/s for a maximum time of 10 s for each cargo run. Average collective force is calculated as the average of the total x-component of motor forces over all time samples and cargo runs and then rescaled by NF_s. N=4 and [ATP] = 2 mM. Reprinted with permissions from Sarpangala and Gopinathan, *PLos Comput. Biol.*, 2022 [125]. CC-BY-4.0. . 50

Figure 3.D.1: **Schematic with the motor forces.** $\vec{X}$ is the center of mass of the cargo. $\vec{A}_i$ are the anchor position vectors of motors. $\vec{H}_i$ are the position vectors of the microtubule-bound motor heads. Corresponding motor forces are represented by $\vec{F}_i$. 59

Figure 3.D.2: **Schematic diagram of a cargo with 1 motor under a fixed hindering load.** It is assumed that motor diffuses until the tangential component of force on the cargo surface reduces to 0. 61

Figure 3.E.1: **Motor and cargo position and corresponding forces.** Variables and the simulation parameters same as Fig. 3.2.0(a) Reprinted with permissions from Sarpangala and Gopinathan, *PLos Comput. Biol.*, 2022 [125]. CC-BY-4.0. 63

Figure 3.E.2: **The fraction of the force distribution with a magnitude of force f greater than or equal to $0.01F_s$, as a function of the diffusion constant for the different number of bound motors n.** Error bars represent the standard error of the mean obtained by the bootstrap method. F_s is the stall force of kinesin. The fraction increases as a function of n for rigid cargo but decreases for lipid cargo. Required force distributions as a function of n and D were obtained using the same procedure as explained in Fig. 3.2.0(b) (simulations without rotational diffusion, N=16, [ATP] = 2 mM).Reprinted with permissions from Sarpangala and Gopinathan, *PLos Comput. Biol.*, 2022 [125]. CC-BY-4.0. 64

Figure 3.E.3:**Fraction of force distribution with force magnitude greater than $0.01F_s$ in the assistive direction.** Required force distributions as a function of n and D were obtained using the same procedure as explained in Fig. 3.2.0(b) (simulations without rotational diffusion, N=16, [ATP] = 2 mM). Reprinted with permissions from Sarpangala and Gopinathan, *PLos Comput. Biol.*, 2022 [125]. CC-BY-4.0. 65

Figure 3.E.4:**Mean value motor force (in Newtons) experienced by a bound motor as a function of the number of bound motors n and diffusion constant D.** Mean force magnitude is negative which means on an average the motor is in the hindering direction, as one would expect because of active motion of motor on MT. The magnitude of mean force decreases with an increase in the number of bound motors due to load sharing. (simulations without rotational diffusion, N=16, [ATP] = 2mM) Reprinted with permissions from Sarpangala and Gopinathan, *PLos Comput. Biol.*, 2022 [125]. CC-BY-4.0. 65

Figure 3.E.5:**The mean variance of forces (in units of N^2) among bound motors.** Calculated as $\frac{1}{S}\sum_{i=1}^{S}\sigma^2_{|f|}(i)$ where the summation is over all the sample time points where the number of bound motors is n. $\sigma^2_{|f|}(i)$ is the variance in the magnitude of force experienced by the n bound motors at i^{th} data sample. $S = 10000$ except for (i) $D = 0$ $n = 3$, $S = 7360$ (ii) $D = 0$ $n = 4$, $S = 1083$ (iii) $D = 0.001$ $n = 4$, $S = 3754$ (iv) $D = 0.01$ $n = 4$, $S = 6396$ (v) $D = 0.01$ $n = 4$, $S = 3508$ (vi) $D = 0.1$ $n = 4$, $S = 4883$. (simulations without rotational diffusion, N = 16 [ATP] = 2 mM). Reprinted with permissions from Sarpangala and Gopinathan, *PLos Comput. Biol.*, 2022 [125]. CC-BY-4.0. 66

Figure 3.E.6:**Simulation results for different cargo radii**. (a) Distribution of the absolute magnitude of motor forces in rigid and lipid cargoes for two different cargo radii, without considering rotational diffusion of cargo. (b) Distribution of the absolute magnitude of motor forces in rigid and lipid cargoes for two different cargo radii, including rotational diffusion of cargo. (c) Mean force correlation between x-components of motor forces (d) Mean single motor off-rate. N=16, [ATP]= 2 mM. Reprinted with permissions from Sarpangala and Gopinathan, *PLos Comput. Biol.*, 2022 [125]. CC-BY-4.0. 67

Figure 3.E.7:**Distribution of cargo displacements (position fluctuations) measured in 0.01 s time intervals along (a) x-axis (b) y-axis and the (c) z-axis.** In general, fluctuations increase with the increase in the fluidity of the cargo surface. Vertical lines indicate the mean values of fluctuations, interpreted as $v_{eff}\delta t$ where v_{eff} is the effective velocity of cargo and δt is the time interval used for measuring fluctuations (0.01 s). Fluctuations along the x-axis have a positive mean ($v_{eff}\delta t \approx 8\,nm$) because of the active motion due to molecular motors. Fluctuations along the y-axis and z-axis have a 0 mean. Fluctuations along the z-axis are much narrower than fluctuations along the y-axis and x-axis because of the steric force due to the microtubule. Data were obtained from the transport of cargoes (without rotational diffusion) with a total of $N = 16$ motors at [ATP] = 2 mM. 200 cargo runs were considered for each diffusion constant. Reprinted with permissions from Sarpangala and Gopinathan, *PLos Comput. Biol.*, 2022 [125]. CC-BY-4.0. . . . 68

Figure 3.E.8:**Standard deviation (nm) of the position fluctuations as a function of diffusivity and the number of bound motors.** Data were obtained from the simulation of the transport of cargoes (without rotational diffusion) with a total of $N = 16$ motors at [ATP] = 2 mM. 200 cargo runs were considered for each diffusion constant. Reprinted with permissions from Sarpangala and Gopinathan, *PLos Comput. Biol.*, 2022 [125]. CC-BY-4.0. 69

Figure 3.E.9: **(a) Conditional on-rate measured from the simulation trajectories.** We simulated 200 cargo runs (without rotational diffusion) for N = 16 [ATP] = 2 mM case and recorded the value of the number of bound motors at a sampling rate of 100 s^{-1}. With this data, we identified all the n bound motors to $n+1$ bound motor transitions, calculated the mean time for such transitions, and then the mean rate (1/meantime). We then divided this rate by the number of unbound motors $N-n$ to obtain the conditional on-rate per motor. We then repeated the analysis process for a different number of bound motors n and diffusion constants D. **(b) Comparing the measured conditional on-rate with analytical expressions.** Black triangles with dashed lines provide conditional on-rate where we consider the increase in on-rate of a single motor with an increase in the number of bound motors. Grey circles with a dashed line provide conditional on rate assuming a constant single motor on-rate. It can be inferred that if we measure this quantity in experiments one can expect to see only a slight increase as the cargo comes closer to the microtubule. This is because as the number of bound motors increases, the effective detachment rate of the n-bound state increases, hence the gating time decreases. Our analysis shows that the decrease in gating time contributes more to the increase in the conditional on-rate than the increase in the single motor on-rate. See Appendix 3.A for more details. Reprinted with permissions from Sarpangala and Gopinathan, *PLos Comput. Biol.*, 2022 [125]. CC-BY-4.0. . 70

Figure 3.E.10 **Ensemble average (± SEM) of the number of bound motors for three different cargo-motor systems.** Vertical lines indicate the estimated time-scales, mean time for a new motor to bind - τ_{bind} (dashed lines) and mean unbinding time of a kinesin motor - τ_{off} (solid black line). N is the total number of motors on cargo, High [ATP] = 2 mM, Low [ATP] = 4.9 μM. The averaging was performed over 200 cargo runs (without rotational diffusion) each. Please refer to Table 1 in Appendix 3.A for more information on τ_{bind} and τ_{off}. Reprinted with permissions from Sarpangala and Gopinathan, *PLos Comput. Biol.*, 2022 [125]. CC-BY-4.0. 71

Figure 3.E.11 **The distribution of the angular distance ($\Delta\Theta$) between the anchor positions of microtubule bound motors along the great circles connecting them ($\Delta\Theta$).** 200 cargo runs were considered for each parameter set with data sampling rate = 100 s^{-1}). Reprinted with permissions from Sarpangala and Gopinathan, *PLos Comput. Biol.*, 2022 [125]. CC-BY-4.0. . . . 71

Figure 3.E.12 **(a) Average number of motors (± SEM) (b) Runlength (± SEM) for more values of diffusion constants.** Averaging was performed over 200 cargo runs in each case. Reprinted with permissions from Sarpangala and Gopinathan, *PLos Comput. Biol.*, 2022 [125]. CC-BY-4.0. 72
Figure 3.E.13 **Probability distribution of the number of bound motors in three different cargo-motor systems. High [ATP] = 2 mM, Low [ATP] = 4.9 μM.** Data were obtained from 200 cargo runs for each case. Reprinted with permissions from Sarpangala and Gopinathan, *PLos Comput. Biol.*, 2022 [125]. CC-BY-4.0. 72
Figure 3.E.14 **Velocity of cargo along x-axis, v_x^{eff} as a function of the number of bound motors and diffusion constant.** Velocity is measured as the ratio of mean displacement along x-axis in a given time window (we took $\delta t = 0.1s$) to δt. Cargo position data was obtained from the simulations of the transport of cargoes with a total of $N = 16$ motors at [ATP] = 2 mM. 200 cargo runs were considered each for each diffusion constant. We recoreded data at a sampling rate of 100 s^{-1}. Data in (b) is for N= 16, [ATP] = 2 mM without rotational diffusion. Error bars represent the standard error of the mean. For figure (a) we considered 10000 random time windows over 200 cargo runs to get the mean displacement for each diffusion constant. For figure (b) we considered all the time window samples with given n over all the cargo runs. Reprinted with permissions from Sarpangala and Gopinathan, *PLos Comput. Biol.*, 2022 [125]. CC-BY-4.0. 73
Figure 3.E.15 **Average value of motor off-rate as a function of fluidity of cargo surface for N = 4 [ATP] = 4.9 μM.** (Sample size = 530 from 200 cargo runs) Reprinted with permissions from Sarpangala and Gopinathan, *PLos Comput. Biol.*, 2022 [125]. CC-BY-4.0. 74
Figure 3.E.16 **Comparison between run lengths from our simulations (circles) and analytical estimates (maroon triangle, solid, dashed and dash-dotted lines) as described in the main text.** Reprinted with permissions from Sarpangala and Gopinathan, *PLos Comput. Biol.*, 2022 [125]. CC-BY-4.0. 75

Figure 3.E.17 **Analytically estimated runlengths for different cargo radii for a fixed number of motors on cargo.** The general method for calculating runlength analytically is described in the main text. We have numerically computed the access area, S_a, considering the typical distance between cargo surface and MT for 1 motor bound case. τ^m_{off} for computing influx area, $S_I(D) = \sqrt{2D\tau^m_{off}}$, was taken to be 1 s which is the typical motor unbinding time at saturating ATP concentration. Yellow vertical bands in (a) and (b) correspond to the range of physiologically relevant diffusion constants of motors. Reprinted with permissions from Sarpangala and Gopinathan, *PLos Comput. Biol.*, 2022 [125]. CC-BY-4.0. 76

Figure 3.E.18 **Analytically estimated runlengths as a function of cargo radius (R) for a fixed surface motor density (σ).** The general method for calculating runlength analytically is described in the main text. We have numerically computed access area, S_a, considering the typical distance between cargo surface and MT for 1 motor bound case. τ^m_{off} for computing influx area, $S_I(D) = \sqrt{2D\tau^m_{off}}$, was taken to be 1 s which is the typical motor unbinding time at saturating ATP concentration. Yellow vertical bands in (a) and (b) correspond to the range of physiologically relevant diffusion constants of motors. Reprinted with permissions from Sarpangala and Gopinathan, *PLos Comput. Biol.*, 2022 [125]. CC-BY-4.0. 77

Figure 3.E.19 **Comparison of the number of bound motors and cargo runlength without and with rotational diffusion in the model**. (a) Average number of bound motors (b) Runlength. Error bars represent the standard error of the mean. [ATP] = 2 mM. Reprinted with permissions from Sarpangala and Gopinathan, *PLos Comput. Biol.*, 2022 [125]. CC-BY-4.0. 78

Figure 3.E.20 **Simulation results for different cargo radii**. Runlength, and average number of bound motors in rigid and lipid cargoes as a function of the cargo radius. N=16, [ATP]= 2 mM. Reprinted with permissions from Sarpangala and Gopinathan, *PLos Comput. Biol.*, 2022 [125]. CC-BY-4.0. 78

Figure 3.E.21 **Simulation results for different motor stiffness (k_{mot}).** Runlength, average number of motors and motor off-rate for different motor stiffness. N=16 [ATP]= 2 mM. Darkgreen is lipid cargo ($D = 1\mu m^2 s^{-1}$) and grey is rigid cargo ($D = 0$). Reprinted with permissions from Sarpangala and Gopinathan, *PLos Comput. Biol.*, 2022 [125]. CC-BY-4.0. 79

Figure 4.2.1: **Schematic of the heterogeneous motor teams model.** The velocity of a motor v_{mot} depends on the force that it is experiencing and its intrinsic unloaded motor velocity $v_{o,mot}$. The unloaded motor velocity $v_{o,mot}$ is different for each motor, and they are drawn randomly from a given probability distribution like the one shown on the left. Created with BioRender.com . . 83

Figure 4.3.1: **Heterogeneity is essential to explain experimentally observed differences in rigid and lipid cargo velocities.** (a) The three different single motor velocity distributions considered in our study, normal distributions with σ= 20 nm/s, σ = 250 nm/s and bi-delta distribution - two different velocity populations with velocities 350 nm/s and 800 nm/s at the population ratio of 0.3:0.7. When we initialize cargoes, we assign to each motor its unloaded velocity drawn from these distributions. (b) The resultant cargo velocity for three different input single motor velocity distribution. To measure velocity, we obtained cargo position data from the simulations of transport of cargo by teams of motors with the given single motor velocity distribution. For each cargo run, we recorded the cargo position data at a sampling rate of 100 s^{-1}. 200 such cargo runs were considered for each parameter set. Cargo velocity was then measured as the ratio of mean displacement along the x-axis in a given time window to δt (we took δt = 0.1 s). Error bars denote the standard error of the mean (error bars are very small and hence not visible in the figure). For all cases, the number of motors on the cargo was N = 16 and ATP concentration in the medium, [ATP] = 2 mM. For lipid cargoes, we considered a motor diffusion constant of $D = 1\ \mu m^2 s^{-1}$. 85

Figure 4.3.2: **Cargo recentering mechanism doesn't account for the observed velocity difference between slow and fast motors** (a) Schematic of the cargo-motor system considered in this section. Single motor velocities of motors were 350 nm/s (slow) and 800 nm/s (fast) at a population ratio of 0.3 to 0.7 (a bi-delta distribution) (b) Illustration (left) and quantification (right) of the contribution to cargo velocities from cargo recentering mechanism. Error bars are calculated from the error propagation method described in the text. Created with BioRender.com . . 88

Figure 4.3.3: **Evidence for the delay in strain generation between slow and fast motors in lipid cargoes.** (a) Fraction of time and (b) Mean cargo velocity when cargo is being carried by only fast, only slow, and a mixture of slow and fast motors. To get data in (a) and (b), we first ran simulations of cargo transport with N=16, [ATP]= 2 mM and recorded data at a sampling rate of 100 s^{-1} for 200 independent cargo runs each for rigid and lipid cargo. From this data set, we filtered out time windows where microtubule-bound motors were (i) all fast motors, (ii) all slow motors, and (iii) a mixture of fast and slow motors. To get fraction of time data in (a), we computed the ratio of the cumulative size for each filtered group to the total size of the trajectory data. To get the velocity data in (b), we measured the cargo velocity by computing mean displacements in short time windows (Δt =0.01 s) among each filtered group. Error bars indicate the standard error of the mean. p values were computed from the students-t test. * represents p $\leq$ 0.05 and ns represents p $>$ 0.05. 90

Figure 4.3.4: **Lipid cargo achieves given runlength with a lower fraction of slower motors or with higher overall cargo velocity.** (a) Runlength of the cargo. Circular markers show the mean runlength measured over 200 cargo runs. The solid lines are analytical estimations of cargo runlength by considering the weighted average of the velocity and unloaded motor unbinding rate. (b) Mean velocity of cargoes. We measured velocity using the same method as we followed for the previous figures. Error bars indicate the standard error of the mean. We considered the parameters, $N = 16$ and $[ATP] = 2$ mM for these simulations (same as in previous figures). 93

Figure 4.A.1: **Velocity of cargo as a function of the number of motors on the cargo for rigid (D=0) and lipid (D=1 $\mu m^2 s^{-1}$) cargoes.** Single motor velocities were 800 $nm\ s^{-1}$ and 350 $nm\ s^{-1}$ at a population ratio of 0.7:0.3. All cargo simulations were performed at saturating ATP concentration of 2 mM. 200 cargo runs were simulated in each case. For each run, the data of cargo positions were collected at a sampling rate of 100 s^{-1}. The cargo velocity was then calculated by measuring the mean displacement of cargo Δx in a time interval of $\Delta t = 0.01\ s$. $v_c = \Delta x/\Delta t$ 98

Figure 4.A.2:**Velocity of cargo as a function of cargo radius for rigid (D=0) and lipid (D=1 $\mu m^2 s^{-1}$) cargoes.** Single motor velocities were 800 $nm\ s^{-1}$ and 350 $nm\ s^{-1}$ at a population ratio of 0.7:0.3. All cargo simulations were performed at saturating ATP concentration of 2 mM. 200 cargo runs were simulated in each case. For each run, the data of cargo positions were collected at a sampling rate of 100 s^{-1}. The cargo velocity was then calculated by measuring the mean displacement of cargo Δx in a time interval of $\Delta t = 0.001\ s$. $v_c = \Delta x/\Delta t$. Grey color represents a rigid cargo, $D = 0$ and Dark green represents a lipid cargo, $D = 1\ \mu m^2 s^{-1}$. 99

Figure 4.A.3:**Bound motor statistics.** (Left) Probability distribution of the number of bound motors in rigid and lipid cargoes. (Right) Fraction of fast motors for a given number of bound motors. To get data in we ran simulations of cargo transport with $N = 16$ motors at [ATP]= 2 mM and recorded data at a sampling rate of 100 s^{-1} for 200 cargo runs each for rigid and lipid cargoes. . 100

Figure 4.A.4:**Position and forces of motors in rigid and lipid cargoes.** Fast motors are colored in magenta; slow motors are colored in cyan. The black line represents the center of mass of the cargo. Negative force values indicate hindering forces, and positive force values indicate that the motor is experiencing assistive forces. The data were collected from cargo transport simulations with a data sampling rate of 100 s^{-1}. From these data, we selected a window where a fast and slow motor are simultaneously bound. The single motor velocities were 800 $nm\ s^{-1}$ (fast) and 350 $nm\ s^{-1}$ (slow) at a population ratio of 0.7:0.3. 101

Figure 4.A.5:**Average cargo velocity as a function of the time elapsed from motor detachment.** We ran simulations with N=16 motors at [ATP]=2 mM and recorded cargo and motor position data for 200 cargo runs each for lipid and rigid cargoes at a sampling rate of 100 s^{-1}. In this time series data, we identified time points where a motor detached and measured the mean displacement of cargo Δx_d, in a time window Δt after such time points. Then we measured velocity as $v_c = \Delta x_d/\Delta t$. . . . 102

Figure 4.A.6:**Distributions of motor head positions relative to the center of mass of the cargo.** (a) Rigid cargo and (b) Lipid cargo. Distribution of x-component of motor force in (c) Rigid and (d) Lipid cargoes. Data obtained from cargo simulations performed at high ATP with 16 motors. Population ratio of fast (800 nm s^{-1}):slow (350 nm s^{-1}) is 0.7:0.3 103

Figure 5.2.1: **Cargo transport across roadblocks of the size of a single binding site.** (a) Runlength, and (b) Cargo velocity as a function of the probability of encountering a roadblock on the next site (P) and diffusion constant of motors on the cargo surface (D). Values were averages over 200 cargo runs. $[ATP] = 2$ mM (staurating ATP) and $N = 4$. Error bars represent the standard errors of means. 108

Figure 5.2.2: **Analysis of cargo interaction with roadblocks.**(a) Probability distribution of displacements Δx (displacements along x-axis) of a cargo in Δt= 1 s for P=0.01. The number of displacement samples collected were 8000. The curves are the kernel density estimates (kde) obtained using distplot method of seaborn module in python. (b) Pause probability as a function of the diffusion constant and roadblock probability (P). Pause probability was estimated as the area under the probability distribution curve for $\Delta x < 0.4\,\mu m$. Data was from cargo transport at saturating ATP conditions, [ATP] = 2 mM with N=4. 109

Figure 5.2.3: **Pause time statistics.** (a) Distribution of pause times for different diffusion constants for P=0.01. Pause state is defined as the state in which at least one motor is stuck at a roadblock (b) Mean pause time as a function of P and D. The same parameters were used for cargo transport simulation as in the previous figure. 110

Figure 5.2.4: **Schematic diagram of a hurdle.** Hurdles are ringlike roadblocks around microtubules. They are modeled as a region of width w that is unavailable for motor binding and transport. A motor that walks up to this region gets stuck there until it's stochastic detachment. 111

Figure 5.2.5: **Probability of crossing hurdle increases with increase in cargo surface fluidity.** (a) Typical cargo trajectory. Black line: x-position of the center of mass of the cargo. Yellow lines: positions of motor heads along the microtubule. The hurdle is at position $x = 250$ nm. Cargo is said to have crossed the hurdle when no motor can access region below the hurdle, *i.e* when the center of mass of the cargo covers one radius distance beyond hurdle, $x = R + 250$ nm. (b) Probability of crossing the hurdle for cargo with a singly bound motor. Average was over 200 cargo runs. Error bars represent standard error of means. (c) Schematic to illustrate parameter dependence of sensitivity of pass prbability to cargo surface fluidity. Pass probability is sensitive to cargo surface fluidity when mean binding time for a new motor τ_{bind} is less than mean unbinding time τ_{off}, *i.e.* when the number of motors on the cargo N is high or when ATP concentration in the medium is low or both. 113

Figure 5.2.6: **Pause time analysis reveals distinct mechanisms used by lipid and rigid cargoes in navigating hurdles.** (a) Mean pause time at the hurdle for cargoes that crossed. Mean was over 200 cargo runs, at $N = 4$ and [ATP] = 4 μM. (b) Distribution of pause time for extreme diffusion constant cases, Rigid ($D = 0$) and Lipid ($D = 1\ \mu m^2 s^{-1}$). Insets show the cargo trajectories. (i) Typical cargo trajectory of rigid and lipid cargoes that have pause time near the peak of the distribution (ii) Trajectory of rigid cargo with Pause time about 20 s (iii) Trajectory of lipid cargo with pause time about 35 s. 115

Figure 5.2.7: **Pass probability and Mean Time to pass.** For three different parameter sets as a function of the initial number of bound motors (initial_bound) on the cargo and cargo surface fluidity (D). Pass probability increases with increase in D for initial_bound=1. Pass probability decreases with increase in D for initial_bound>1. Pass probability increases with increase in the number of bound motors. The hurdle of width, w=16 nm is located at x=250 nm. The center of mass of each cargo was initialized at x=0. So the hurdle is right at the edge of the cargo (cargo radius is 250 nm). cargoes are said to have passed only if their CM crosses x=500 nm which is one radius away from roadblock. 200 cargoes were considered for each case. Error bars represent the standard error of the mean. 119

Figure 5.2.8: **Effective pass probability of cargoes increases significantly as a function of the cargo surface fluidity for multimotor transport at low [ATP].** Effective probability was calculated as an average of the pass probabilities for different number of bound motors (Fig. 5.B) weighted by the probability distributions of the number of bound motors for three-different parameter sets. 120
Figure 5.B.1: **Analytical estimation agrees with the measured value of pass probability.** Sold markers: Simulation values. Hollow Markers: Analytical estimation specifically for rigid cargoes taking into account the probability of different numbers of motors in the access region.Solid lines: Analytical approximation. . 124
Figure 5.C.1: Mean lifetime is independent of D and P. Data was obtained from transport of cargo with 4 motors at high ATP concentration of 2 mM. 200 cargo runs were considered for calculating the mean. Error bars represent the standard error of the mean. 125

Figure 6.1.1: **Schematic of a three-dimensional microtubule lattice structure.** (a) lengthwise view and (b) cross-sectional view. This microtubule has 13 protofilaments. Created with BioRender.com 127
Figure 6.2.1: **On-rate of cargo held at specific distances from microtubules.** Cargo is rigid with $N = 16$ motors. The microscopic on-rate of motors was scaled up to get a shorter mean-binding time for computational convenience. Motor models used: No compressive resistance: One-sided spring that exerts resistance to extension with force constant, k_{mot}=0.32 pN/nm but no resistance to compression (grey line). Compressive force up to 1 pN: For extension, exerts a linear force with a force constant, k_{mot}=0.32 pN/nm and for compression exerts a linear force with force constant of k_{mot}=0.05 pN/nm and saturates at compressive force of 1 pN (blue line). 131

Figure 6.2.2: **The number of accessible sites defined as the number of microtubule sites weighted by Boltzmann weights based on motor's energy cost to access sites.** Data was from numerical computations, a motor was held at specific distances away from the microtubule axis, and the sum of Boltzmann weights over all lattice points was computed. Different models of motors: (a) One-sided spring: exerts resistance to extension with force constant, k_{mot}=0.32 pN/nm but no resistance to compression (brown dashed line). (b) Double-sided spring: resists both compression and extension linearly with force constant of k_{mot}=0.32 pN/nm (red dashed line), (c) Bind only within L_{mot}: No resistance to compression but also no binding to any points beyond the rest length of motor L_{mot} (green dotted line), (d) Compressive force up to 1 pN: For extension, exerts a linear force with a force constant, k_{mot}=0.32 pN/nm and for compression exerts a linear force with force constant of k_{mot}=0.05 pN/nm and saturates at compressive force of 1 pN (blue dash-dotted line). 132

Figure 6.3.1: **Schematic of the planned motor force computations in complex binding geometries.** A is the motor anchor position on cargo. H is the head position on the microtubule. The motor linker is treated like a Gaussian chain. F_{int} is the entropic force due to the grafting of the chain to the microtubule surface. This entropic force tends to align the motor perpendicular to the surface, equilibrium position A_{eq}. F_{spring} is the spring-like force of free chain with end positions at H and A, also due to entropy. F_{mot} is the resultant motor force. Created with BioRender.com 133

LIST OF TABLES

Table 3.A.1:**Comparison of the single motor binding and unbinding times for different N and [ATP]** 55

ACKNOWLEDGEMENTS

I thank my advisor Prof. Ajay Gopinathan for his patience, kindness, and expert guidance. The time and freedom he gave me were invaluable in helping me figure out my interests and develop as a researcher. I am influenced by his ability to work on multiple tasks efficiently while being mindful of the bigger picture. The flexibility, support, and time he gave me to fix my mistakes helped strengthen my weaker points without getting stressed. He was always there when I was struggling and needed help, and I am forever grateful for that.

I am also extremely grateful to my Ph.D. committee members Prof. Linda Hirst, Prof. Kinjal Dasbiswas, and Prof. Jing Xu for further helping me learn how to think, communicate and handle questions as a researcher. Their expertise in different subjects helped me build my thesis.

I'm incredibly grateful to the all teachers who have shaped my academic journey. I thank my high school teacher Sindhu Muralidharan for her amazing dedication to teaching science and inspiring me to take up basic science research. I am grateful to Prof. Sridhar Rajaram, whose guidance and motivation led me to apply for graduate schools in the USA. I thank my master's thesis advisor, Prof. Mithun Mitra (IIT-Bombay), for introducing me to studies on soft matter and statistical mechanics. I'm also indebted to Prof. Dibyendu Das and Prof. Raghunath Chelakkot at IIT Bombay for their invaluable mentorship. Their support and expertise have played a significant role in my growth as a scholar.

I consider myself fortunate to have collaborated with Dr. Oleg Kogan, whose enthusiasm for physics was truly inspiring. Working with him taught me valuable lessons and enriched my understanding. I am also grateful to Prof. Suliana Manley and Emine Berna Durmus for generously sharing their experimental data and engaging in insightful discussions on cell biology of motor-based transport. Prof. Jenny Ross and Nimisha Krishnan provided me with a wealth of experimental data, and collaborating on the paper with them was a rewarding experience. I

extend my heartfelt thanks to undergraduate student researcher Maria Gamez for her dedicated efforts in working with me on this project.

Moreover, I am extremely thankful for being a part of a collaborative project on active nematics with Prof. Linda Hirst, Prof. Kinjal Dasbiswas, Prof. Daniel Beller, and the graduate students Fereshteh Memarian and Madhuvanthi Athani, as well as post-docs Joseph D. Lopes and Fabian Jan Schwarzendahl. This project allowed me to engage in intriguing experimental analysis. Their support and collaboration have been instrumental in this remarkable journey.

I am grateful for the support, cooperation and mentorship from Gopinathan lab members, including Dr. Bhavya Mishra, Dr. Monika Sanoria, Dr. Farnaz Golnaraghi, Dr. Imtiaz Ali, Jose Zamora Alvarado, Dr. Ritwika VPS, Joey Mctiernan, Patrick Noerr and Suraj Sahu. Special thanks to Dr. David Quint for helping me develop my computational model and for all his mentorship during graduate school. I learned so many things by interacting with my lab members.

Also grateful to my friends and the Indian student community, physics graduate student community at UC Merced for such great support. Specifically, I thank Amanda Tan, Megha Suswaram, Nivin Mothi, and Som Sarang for their help and mentorship during graduate school. I thank all my housemates during the last six years, including Anuvetha Govindarajan, Madhuvanthi Athani, Jacqueline Giacoman, Benny Nguyen, Iman Ebrahimi, Maria Perez Mendoza, Swadha Singh, and Ekta Kandhway for the live discussions, game nights, cooking, and support, especially during COVID times.

I thank the Physics Department at UC Merced, the most student-friendly department I have ever seen. Thanks to CCBM for providing great resources and thereby enabling quality research. I also want to acknowledge the graduate division for their hard work in ensuring graduate students get what they need to be successful in school.

My research was supported by NSF (DMS-1616926, ACI-1429783), NSF-CREST Center for Cellular and Bio-molecular Machines (NSF-HRD-1547848). I thank GSOP Fellowship and Graduate Dean Dissertation fellowships from the UC Merced graduate division and the Physics department for nominating me to these fellowships.

Finally, I would like to express my deep gratitude to my parents, brother, and all my family. It wouldn't have been possible to pursue my studies till this point without their trust and unconditional love.

CURRICULUM VITAE

Niranjan Sarpangala
(209) 285 - 9818 — nsarpangala@ucmerced.edu

Education

University of California, Merced	2017 - present
PhD candidate in Physics	(GPA: 4.0/4.0)
Indian Institute of Technology, Bombay	2014 - 2016
Master in Physics	(CPI: 8.8/10.0)
Mangalore University	2011 - 2014
Bachelor of Science	(96.42%)

Publications

1. F. L. Memarian, J. D. Lopes, F. J. Schwarzendahl, M. G. Athani, **N. Sarpangala**, A. Gopinathan, D. A. Beller, K. Dasbiswas, L. S. Hirst, "Active nematic order and dynamic lane formation of microtubules driven by membrane-bound diffusing motors", *Proceedings of the National Academy of Sciences*, 118, (2021).

2. **N. Sarpangala**, A. Gopinathan, "Cargo surface fluidity can reduce inter-motor mechanical interference, promote load-sharing and enhance processivity in teams of molecular motors", *PLOS Computational Biology*, 18, 1–32, (2022).

3. N. Krishnan, **N. Sarpangala**, M. Gamez, A. Gopinathan, J. L. Ross, "Effects of Cytoskeletal Network Mesh Size on Cargo Transport", *Submitted to The European Physical Journal E*, (2023).

4. **N. Sarpangala**, B. Randell, A. Gopinathan, O. Kogan, "Tunable intracellular transport on converging microtubule morphologies", *arXiv*, (2023).

Research Projects

Understanding the role played by the lipid membrane on multi-kinesin transport.

Ph.D. thesis project with Prof. Ajay Gopinathan.

We developed a three-dimensional Brownian dynamics model of cargo transport along microtubules (MT) by teams of kinesin-1 motors. Using this model, we showed that the fluid surfaces of cellular cargo reduce the mechanical interference between motors allowing better load sharing and increased duration of motors on the filament, thereby increasing the distance over which they can carry cargo. We also explained that the experimentally observed increase in cargo velocity with fluidity is due to heterogeneity in single motor velocity. Currently applying the model to understand the cargo transport across roadblocks on MT such as amyloid-β in Alzheimer's disease. So far, our work has explained several existing experimental observations and generated experimentally testable predictions. We believe that our work also has useful insights for synthetic motor transport projects. Part of my thesis work is now published in Plos CB.

Image analysis projects.

with Prof. Ajay Gopinathan, Prof. Kinjal Dasbiswas, Prof. Daniel Beller, Dr. David Quint, Prof. Linda Hirst, Prof. Jennifer Ross, and Prof. Suliana Manley.

I performed microscopy image analysis for several collaborative projects.

1. Analysed microtubule collisions in microtubule gliding assay experiments using FIJI. Measured collision input and output angles and classified the collision types. This work is now published in PNAS.

2. Developed MATLAB code to track and analyze microtubule filament orientations in gliding assay experiments.

3. Extracted microtubule network from *in vitro* and *in vivo* fluorescence microscopy images using MATLAB package called FIRE and ran cargo transport simulations on the extracted networks.

4. Recorded movies of a nanoparticle self-assembly process and developed a MATLAB program to analyze the growth rate of nanoparticle clusters.

Effectiveness of converging microtubule morphologies in clustering materials in cells.

with Dr. Oleg Kogan, Prof. Ajay Gopinathan.

Developed a one-dimensional Monte Carlo model of cargo transport along two oppositely oriented microtubules converging at the microtubule organizing center. We found that the mean first passage time taken by cargoes to exit out of such microtubule traps is sensitively dependent on parameters like microtubule attachment and detachment rates, velocity, etc. This work has relevance in processes such as the transport of viruses to replication sites, transport of vesicles between the endoplasmic reticulum and Golgi apparatus, clustering of lytic granules in immune cells, etc.

Understanding the phase separation in thin film blends of P3HT and PCBM.

Master's thesis project with Prof. Mithun K. Mitra, IIT Bombay (2016).

Solved the modified Cahn Hilliard Cook equation, which governs surface-directed spinodal decomposition using a python package 'fipy' in a 2D lattice. Estimated the interfacial crystallization rates of PCBM as a function of time which was in agreement with previous experimental results.

Minor Projects Experience

Liquid crystal mediated nanoparticle self-assembly.

Graduate Rotation Research with Prof. Linda Hirst at UC Merced (2018).

Worked on a nanoparticle self-assembly process that is driven by the isotropic to the nematic phase transition of the host liquid crystal. Recorded movies of this self-assembly process and developed a Matlab program to analyze the movies.

Zeros of the partition function of q-state Potts model.

Course Project with Prof. Dibyendu Das at IIT Bombay (2016).

Expressed partition function of q-state Potts model as a polynomial and found its zeros (numerically) in complex temperature plane (called 'Fisher zeros') for 1D and 2D lattices of different sizes and for different q values. Identified the possible critical points for temperature-driven phase transitions in such systems

Coherent Population Trapping in ^{87}Rb atoms into the hyperfine levels of the ground state.

Summer internship with Prof. Vasant Natarajan at IISc Bangalore (2015).

Performed Coherent Population Trapping in ^{87}Rb atoms into the hyperfine levels of the ground state. Required optical fields were obtained by phase modulation of a laser beam from a single source using an electro-optic modulator.

Stereoselective synthesis of amino acids

Summer internship with Prof. Sridhar Rajaram at JNCASR Bangalore (2014).

Performed organic reactions, monitored reactions by thin layer chromatography, and extracted required compounds through flash column chromatography.

Preparation of Se-S chalcogenide glasses

Summer internship with Prof. Sebastian C. Peter at JNCASR Bangalore (2013).

Prepared Se-S chalcogenide glasses doped with heavy metals like Tl, Bi, Sb, and Pb by melt quench technique. The amorphous nature of prepared compounds was confirmed with powdered XRD. Studied IR spectra and UV-Vis spectrum of the

compounds.

Teaching Experiences

Worked as a Teaching Assistant at the University of California, Merced, for the following courses.

1. Calculus II – MATH-012 (Fall 2017)
2. Introductory Physics II – PHYS-009 (Spring 2018, Spring 2019, and Fall 2020)
3. Analytical Mechanics – PHYS-105 (Spring 2021)
4. Thermal Physics – PHYS-108 (Fall 2021)
5. Electricity and Magnetism – PHYS-110 (Fall 2021)

Conferences and Presentations

1. APS March Meeting, Boston, Massachusetts, 2019 *(oral presentation)*
2. Open House, Center for Cellular and Biomolecular Machines, UC Merced, 2019 *(poster presentation)*
3. APS March Meeting, Virtual, 2020 *(oral presentation)*
4. APS March Meeting, Virtual, 2021 *(oral presentation)*
5. APS March Meeting, Chicago, 2022 *(oral presentation)*
6. Annual Retreat, Center for Engineering Mechanobiology, Pennsylvania, 2022 *(poster presentation)*
7. Annual Retreat, Center for Cellular and Biomolecular Machines, UC Merced, 2022 *(poster presentation)*

8. Physics of Life Symposium, San Fransisco, CZ Biohub, 2023 *(selected, oral presentation)*

9. APS March Meeting, Las Vegas, 2023 *(oral presentation)*

10. Post-doc preview day, Center for Engineering Mechanobiology, Pennsylvania, 2023 *(selected, oral presentation)*

Fellowships and Awards During Ph.D.

1. "Best academic performance in the first year" award by the Department of Physics, UC Merced (2018).

2. Graduate Student Opportunity Program Fellowship from the UC Merced Graduate Division (2019 - 2020).

3. "Outstanding student service and outreach" award by the Department of Physics, UC Merced (2021).

4. Graduate Dean's Dissertation Fellowship, from the UC Merced Graduate Division (Spring 2023).

Other Academic Achievements

1. INSPIRE-Scholarship for Higher Education by the Department of Science and Technology, INDIA (2012 - 2014).

2. Diploma in Chemistry from JNCASR Bangalore through completion of Project Oriented Chemical Education (POCE) Program (2014).

3. Second rank in B.Sc. Program, Mangalore University (2014).

4. All India Rank 20 in Indian Institute of Technology - Joint Admission Test (2014).

5. "Most improved toastmaster" by the Big Shots Toastmasters club (2020).

6. Independently mentored two undergraduate students on research projects (2021 - present).

7. Developed computational modules for the Biophysics course at UC Merced (2019 - 2022).

Last updated: August 10, 2023

ABSTRACT OF THE DISSERTATION

Effect of lipid membranes on intracellular cargo transport by teams of molecular motors

by

Niranjan Sarpangala
Doctor of Philosophy in Physics
University of California Merced, 2023

In cells, multiple molecular motors work together as teams to carry cargoes, such as vesicles and organelles, over long distances to their destinations by stepping along a network of cytoskeletal filaments. A type of molecular motors, kinesins, are known to mechanically interfere with each other and be non-cooprative when assembled in *in vitro* experiments. However, these motors transport cargo over long distances in cells. It is unclear what is causing the enhanced teamwork between motors in cells. In this dissertation, we explore the possibility of lipid membranes enclosing most intracellular cargoes, enhancing teamwork. We understand the effects of lipid membranes on team dynamics by developing a three-dimensional simulation of cargo transport along microtubules by teams of kinesin-1 motors and applying it to various physiologically relevant conditions. In this model, we accounted for cargo membrane fluidity by explicitly simulating the Brownian dynamics of motors on the cargo surface and considered both the load and ATP dependence of single motor functioning. We first apply the model to a more straightforward case of cargo transport by identical kinesin motors. These simulations show that surface fluidity could lead to the reduction of negative mechanical interference between kinesins and enhanced load sharing, thereby increasing the average duration of single motors on the filament. This, along with a cooperative increase in on-rates as more motors bind leads to enhanced collective processivity. At the cargo level, surface fluidity makes more motors available for binding, which can act synergistically with the above effects to further increase transport distances

though this effect is significant only at low ATP or high motor density. These results reconcile experimental obervations of cargo runlength. Additionally, the fluid surface allows for the clustering of motors at a well defined location on the surface relative to the microtubule and the fluid-coupled motors can exert more collective force per motor against loads. Then we proceed to understand cargo transport at different physiologically relevant complexities, starting with heterogenous teams of motors. *In-vitro* experiments of membrane-bound cargo transport by teams of motors have reported that coupling motors through a lipid membrane lead to higher cargo velocity. However, the mechanisms behind this increased lipid cargo velocity are unclear. Using suitable modifications to the Brownian dynamics model, we show that underlying heterogeneity in single motor velocity is essential for increased velocity of lipid cargoes. We further explored other advantages of having heterogeneous motor velocities on lipid cargoes. Our simulations show that while runlength of both rigid and lipid cargoes increases with an increase in the motor velocity heterogeneity, lipid cargoes can travel a given distance with a lower degree of heterogeneity meaning a higher cargo velocity. Together our work explains mechanisms behind previous experimental observations and generates new experimentally testable predictions on runlength relevant for *in vivo* transport.

Next, we discuss breakdowns in cargo transport due to intracellular complexities and possible lipid membrane-mediated rescue. Presence of different kinds of roadblocks on the microtubule lattice, such as Microtubule Associated Proteins (MAPs) like the tau protein, neurofibrillary tangles, stalled cargoes, etc, are known to disrupt cargo transport [144, 92]. Enrichment of such roadblocks, specifically amyloid plaques and neurofibrillary tangles are observed in brain cells of patients with neurodegenerative diseases, including Alzheimer's disease [107]. Using Brownian dynamics simulations, we show that membrane-bound cargoes also have a higher probability of crossing roadblocks than membrane-free cargoes under specific conditions. Furthermore, we find that lipid and rigid cargoes might employ qualitatively different strategies to pass certain kinds of roadblocks. Finally, we discuss the effects of having different mechanical models of motors and a three-

dimensional lattice structure in our model and generate experimentally testable predictions to identify a suitable motor model for future studies. We find that this improved model might address the problem of cargo transport across large roadblocks better. More work needs to be done in this direction. Overall our work on understanding how lipid membrane impacts cargo transport by teams of motors sheds new light on cellular processes, reconciles existing observations, and encourages new experimental validation efforts; This also suggests new ways of improving the transport of artificial cargo powered by motor teams. We believe our work may inform future research on better treatments for neurodegenerative diseases like Alzheimer's, which are caused due to breakdowns in transport.

Chapter 1

Introduction

1.1 Transport of materials in cells

Proper functioning of cells requires the transport of different components like membrane-bounded vesicles and organelles, protein rafts, mRNA, chromosomes, etc., from one part of the cell to another [36]. Diffusion is one mechanism of cargo transport in cells. However, it is a slow process, especially in a medium like a cell that is crowded to such an extent that 20 - 30% of the intracellular volume is occupied by macromolecules [42]. This is evident in the reported values of self-diffusion rates of macromolecules of sizes varying from 2 - 45 nm which are 40% - 5% of their aqueous value [51, 100, 99, 101]. A typical diffusion constant for large vesicles (of size about 300 nm) in cells are of the order of $10^{-11}\,\mathrm{cm^2 s^{-1}}$ [110]. The estimated time to cross a cell of radius 10 μm with this diffusion rate is about 14 hours. In addition, this is anomalous subdiffusion where the mean square distance goes $\langle r^2 \rangle \sim t^{\alpha}$, where $\alpha < 1$ [51, 149, 150, 12, 50]. Thus cells rely on diffusion as a means of transport only for small molecules or for shorter distances. In particular, cells like human neurons which can be meters long and need the transport of cargo bigger than 50 nm cannot survive in the absence of a faster way of cargo transport.

Another disadvantage of diffusional transport is the lack of directionality. Eukaryotic cells are compartmentalized. The proper functioning of cells requires the directed transport of materials between these compartments or organelles. For

example, insulin secretion by pancreatic - β involves a series of steps at organelles endoplasmic reticulum (ER) and Golgi apparatus and hence requires transport of materials between ER, Golgi apparatus, and cell membrane [96]. Cells have evolved to achieve a faster and more directed transport of materials by rectifying the random fluctuations using special protein molecules called molecular motors.

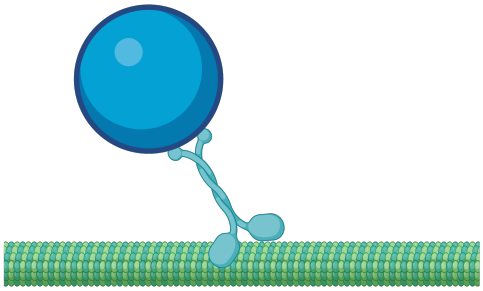

Figure 1.1: Cartoon of molecular motor carrying a lipid cargo and walking on a filament. Created with BioRender.com

1.2 Active transport using molecular motors

Thermal energy in cells leads to constant random motion of materials in cells. Cells have evolved special protein molecules called molecular motors that are capable of rectifying these random fluctuations to generate directed motion to deliver materials to desired locations [1] (See Fig. 1.1). However, an implication of the second law of thermodynamics is that it is impossible to extract directed motion from a random process without the expenditure of energy. In case of molecular motors, the energy for the rectification is obtained from repeated cycles of ATP hydrolysis [127]. The cytoskeleton, which is a network of microtubules, intermediate filaments, and actin filaments, serves as a network of roadways for this motor movement. Molecular motors walk on microtubules or actin filaments carrying cargoes [127]. The orientations of the cytoskeletal filaments play a major role in determining the directionality for cargo transport. In eukaryotic cells, there are three different classes of motors which undergo linear motion. These

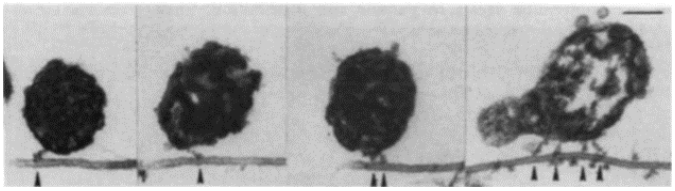

Figure 1.2: **Electron micrograph images showing evidence for multi-motor transport in cells.** Mitochondria with 1, 2 and 4 microtubule bound motors. Scale bar = 0.1 μm. Reprinted with permissions from Ashkin et. al., *Nature*, 1990. [11] .

are kinesins and dyneins which move along microtubules and myosins that move along actin filaments [128]. The polarity of the filaments needed for directional movement of motors is provided by the uniform arrangement of subunits - tubulin dimers in the case of microtubules and actins in case of actin filaments [127]. These motors move in different directions along the filaments typically carrying lipid bilayer vesicles packed with proteins and signaling molecules or even membrane bound organelles such as Golgi and mitochondria [63, 114]. Defects in motor function can impair normal cell functioning and is linked to a variety of pathologies, including neurodegenerative diseases like Alzheimer's disease and amyotrophic lateral sclerosis (ALS) [124, 86, 56, 68, 31, 108]. Owing to the importance of these molecular motors in the functioning of a cell, they have been extensively studied, and hence the single motor biophysical properties are well characterized [64, 142, 87, 136, 147, 155, 7, 129, 131, 22].

1.3 Multi-motor transport

It is often found that intracellular cargoes are carried by teams of molecular motors belonging to the same class as well as different classes [109, 11, 53, 60, 85]. See Fig. 1.2 for an early electron micrograph image indicating that cargoes are associated with microtubule with multiple motors. This simultaneous action of multiple motors enables the generation of sufficient force to move in highly viscous

in vivo environments, to travel longer distances, and also achieve complex features of intracellular transport like the bidirectional transport, switching at cytoskeletal intersections [78]. In spite of several experimental and theoretical studies [3, 62, 133, 104, 77, 76, 14, 111, 5, 66], several aspects of cooperativity and competition between multiple motors in carrying intracellular cargoes remain to be explored. Several theoretical and *in vitro* experimental studies [40, 122, 69, 117, 105] indicate that the collective behavior of motors is critically influenced by their coupling to each other, resulting in observable effects in transport speeds and run lengths. For example, it is known that non-cooperative kinesin motors coupled together by a rigid cargo interfere with each other's functioning leading to enhanced detachments and lowered run lengths [40, 122, 69].

1.4 Effect of lipid membranes on multi-motor transport

If motors interfere with each other's functioning, how do we explain the long-distance transport of membrane-bound vesicles and organelles by teams of kinesin motors in cells [103, 13]? One difference in cells is the presence of lipid membranes enclosing cargoes. Intracellular cargoes are typically covered with a lipid membrane. For example, it is observed that kinesins transport membrane-bound organelles like mitochondria, synaptic vesicle precursors in axons, endosomes, lysosomes, etc [61]. Membranes provide an efficient way for packing and delivering cargo materials [140]. In addition to this role, the cargo membranes are also shown to regulate molecular motor-based transport. For example, it was observed that dynein motors cluster into microdomains on the cargo surface as the phagosomes mature leading to their rapid transport towards lysosomes [119]. Another piece of evidence for lipid membranes regulating cargo transport can be seen in the cargo surface-mediated dimerization of kinesin-3 motors leading to the creation of processive kinesin-3 dimers [135] Although these ways of regulating transport are important, we hypothesize that there might be other, more physical ways in which lipid membranes influence transport. It is observed that molecular motors diffuse

in such membranes [54]. We think that this ability of motors to move on the cargo surface might increase the availability of motors for microtubule binding, and aid the motors in relaxing some tension arising due to the unfavorable positioning of the cargo or other bound motors. Lipid membrane may also help achieve high cargo velocity by allowing faster motors to slide on the surface and come to the posterior of the cargo, resulting in a higher likelihood of assistive forces and increased off rate for slower motors.

We explore these possible effects of lipid membranes on cargo transport by teams of molecular motors. Specifically, we study how lipid membranes influence the transport properties of intracellular cargoes like runlengths, lifetime, velocities, and their ability to navigate around different kinds of roadblocks in an ATP-dependent and motor number dependent manner. The results from our study could potentially inform future efforts in designing drug delivery systems, better cures for neurodegenerative diseases, and artificial cargo transport processes.

1.5 Outline

- **Chapter 2: Computational Model**
  In Chapter 2, we describe the development of the Brownian dynamics model of cargo transport by teams of motors that we use throughout this dissertation. In this model, we considered the cargo as a sphere and explicitly simulated the diffusion of motors on this surface to consider the presence of a lipid membrane. The diffusion constant of motors on the surface, D, is a parameter in our model that we vary to study the effect of surface fluidity on team dynamics. Bound molecular motors were modeled like cables (or one-dimensional springs) with their anchor positions on the cargo surface and head positions on the microtubule. The bound motor moves forward on the microtubule at a rate that is dependent on the force it experiences and also unbinds with a force-dependent rate. Overall this is a

3-dimensional stochastic model that takes into account the experimentally reported transport properties, and load-dependent kinetics of kinesin-I motors and the diffusion of motors on the cargo surface because of the presence of lipid membrane.

- **Chapter 3: Effect of surface fluidity on cargo transport by identical motor teams**

  In Chapter 3, we explain the application of the Brownian dynamics model to the case of lipid cargo transport by a team of identical kinesins on microtubules. We discuss how multi-kinesin transport is influenced by fluidities of cargo surfaces in an ATP-dependent, motor number-dependent manner. We show that cargo surface fluidity reduces mechanical interference between kinesin motors, increases availability, and hence increases runlength especially when the number of motors on cargo is high or ATP concentration in the medium is low. These results reconcile conflicting experimental observations on runlength dependence on surface fluidity. This work also generated important experimentally testable predictions. First, we predict that lipid cargo run length increases with a decrease in ATP concentrations. Second, motor teams cluster to defined regions on the lipid cargo surfaces when placed under external load. Third, motor teams on lipid cargo generate higher collective force than motor teams on rigid cargo when placed in an optical trap. These results are also relevant in designing novel artificial transport devices. This chapter is a reproduction of work in [125].

- **Chapter 4: Heterogenous teams of motors on the cargo**
  Although exploring the cargo transport by teams of identical kinesin motors provided us with useful insights into the effect of lipid membranes on cargo transport, the intracellular environment, and *in vivo* motor teams are more complex. It is often found that cargos are carried by non-identical teams of motors, like teams of different types of kinesins, dynein, and myosins in cells. Even motor teams of a given type often have marked differences in veloci-

ties and detachment rates. One cannot ignore some of these complexities in simulations when comparing with certain experimental observations. In this chapter, we explain one such case. *In-vitro* experiments have observed that coupling motors through a lipid membrane ubiquitous in cells leads to higher cargo velocity. However, the mechanisms behind this increased lipid cargo velocity are unclear. We show using our Brownian dynamics model that underlying heterogeneity in single motor velocity is essential for increased cargo velocity of lipid cargoes. We further explored other advantages of having heterogeneous motor velocities on lipid cargoes. Our simulations show that while runlength of both rigid and lipid cargoes increase with an increase in the motor velocity heterogeneity, lipid cargoes can travel a given distance with a lower degree of heterogeneity meaning a higher cargo velocity. Together this work explains mechanisms behind previous experimental observations and generates new experimentally testable predictions on runlength relevant for *in vivo* transport.

- **Chapter 5: Cargo transport across roadblocks**
  Neurodegenerative diseases like Alzheimer's and Parkinson's disease are found to involve disruptions in molecular motor transport due to different kinds of roadblocks on microtubule lattices such as aggregates of tau proteins (neurofibrillary tangles). More generally, a variety of decorating proteins, stalled motors, cargo or other structures in the crowded cytoplasm can act as roadblocks. We explore whether lipid membranes help cargo in crossing these different kinds of roadblocks. Specifically we discuss cargo transport in the presence of (a) roadblocks of the size of a tubulin dimer like membrane associated proteins (ex: tau protein), other microtubule bound motors (b) roadblocks that cover microtubule like a ring (ex: defect sites in annealed microtubules [52]). We show that membrane-bound cargoes have a higher probability of crossing roadblocks than membrane-free cargoes under specific conditions. Our results could inform the development of improved treatments for neurodegenerative diseases.

- **Chapter 6: Three-dimensional microtubule structure and motor properties**

  In Chapter 6, we implement further improvements to our model to enable us to answer more advanced questions of cargo transport by teams of motors, specifically the mechanisms used by motor teams in navigating large roadblocks like stalled cargoes. We implement a modified model of kinesin that takes more experimental details into account [70] as opposed to the simple one-sided spring model [82] that we used so far. We also implement a three-dimensional lattice structure to the model. This generated predictions on the dependence of the on-rate of motors as a function of distance from microtubules that will help us identify the best motor model for future simulations. More work needs to be done in this direction.

- **Chapter 7: Conclusion and Future Directions**
  In the final chapter, I will summarise our findings and present future directions.

Chapter 2

Computational Model

This chapter explains the Brownian dynamics model of cargo transport that is central to my thesis. We outline the main details of the model, including typical values of the parameters used. The content of this chapter is a reprint of the Materials and Methods section of the paper Sarpangala and Gopinathan, *PLos. Comput. Biol.*, 2022 [125]. The co-author listed in this publication directed and supervised research.

2.1 Introduction

Understanding how lipid membranes influence cargo transport requires monitoring the dynamics of single motors and quantifying how lipid membranes influence these dynamics. It is experimentally challenging to measure single-motor forces and hence characterize single-motor dynamics. However, computational models allow us to monitor single motor dynamics and connect these to experimentally measurable quantities like runlength, the collective force generated by motor teams, etc. Thus, we considered modeling approaches to answer this question of how lipid membranes influence cargo transport. Early models of multi-motor cargo transport used a mean-field approach where all motors were considered to share the load equally [112]. Later stochastic models that assume unequal load sharing [82, 88, 84, 24, 69, 156, 151] were found to describe experimental observations better [82, 83, 23]. The next improvement to the model was to explicitly consider that

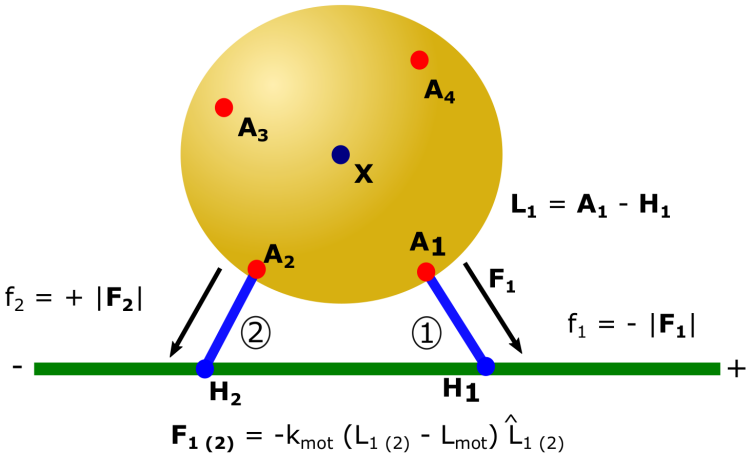

Figure 2.1: **Schematic of the model.** X is the center of mass of the cargo, A_i and H_i represent motor anchor and motor head positions. Motors exert spring like forces only when their lengths L_i exceed their rest length L_{mot}. Here, motor 1 experiences a hindering load (f_1 is negative), while motor 2 experiences an assistive force (f_2 is positive). Microtubule is modeled as a one-dimensional line. Cargo is an undeformable sphere. Motor anchor positions, A_i diffuse on the cargo surface.

motors are bound to a three dimensional spherical cargo surface, that was typically considered rigid [17, 43]. Only a few recent models have attempted to consider the lipid membrane on the cargo surface [113, 97, 25, 32]. For example, Lombardo *et. al.* [97], in the context of transport of vesicles by teams of myosins, modeled an ideally fluid cargo surface where motors instantaneously relax the tangential component of force. Our model is closer to that of Bovyn et. al. [25] where we consider unequal load sharing with explicit implementation of motor diffusion on the cargo surface. Here we describe the basic elements of our Brownian dynamics model, the assumptions involved, the typical range of parameters and the limitations of the model.

2.2 Brownian dynamics model of cargo transport by teams of motors

In our model, we consider a spherical cargo of radius, R ($R = 250$ nm in most cases) which is decorated with a given number of molecular motors (N) on the surface. N doesn't change during the cargo run, meaning there is no binding and unbinding of motors between the cargo surface and the solution. Each of these N motors is initially assigned a random, uniformly distributed anchor position on the cargo surface. Molecular motors on rigid cargo are fixed on the cargo surface. So a given initial configuration of motors on the rigid cargo surface persists throughout the cargo run whereas motors on lipid cargo diffuse on the surface.

In this study we considered all N motors to be kinesin motors with a rest length of $L_{mot} = 57$ nm [93]. We assume that an unbound kinesin motor binds to the microtubule with constant rate, $\pi_0 = 5$ s^{-1} [88], if some part of the microtubule is within L_{mot} distance from the anchor position of that unbound motor. In other words, unbound motors bind with a specific rate to the microtubule if they can access the microtubule. The number of motors on the cargo, (N) is assumed to be constant, similar to several other modeling studies [25, 28]. In other words, we assume the timescale for motor detachment from the cargo is much larger than the lifetime of the cargo on the microtubule.

Each cargo run is initiated with at least one motor bound to microtubule and stopped when all the motors detach from the microtubule. This procedure is similar to Bovyn. *et. al.* [25]. However, in other models [28] the cargo is tracked even during bulk diffusion when all motors are unbound till some motor binds back to the microtubule.

A microtubule bound motor is characterized by two position vectors, anchor point ($\vec{A}$) on the cargo surface and head ($\vec{H}$) on the microtubule. The head position is defined just by its continuous position along the x-axis, *i.e.*, we do not model

the lattice structure of the microtubule unlike in a recent Brownian dynamics model [29]. We justify this based on the fact that the microtubule has multiple protofilaments and when two kinesins are on different protofilaments they can have same x-position on the microtubule. There are also models that have explicitly incorporated the fact the motor heads cannot step on each other [97, 29], which is likely of more importance when the filament has only a few tracks like actin, which has only two protofilaments in a helix, compared to 10 to 15 for microtubules.

A microtubule bound motor is assumed to exert a spring-like force when the length of motor exceeds the motor's rest length (L_{mot}) with a force constant, $k_{mot} = 0.32$ pN/nm [34, 33]. Let $\vec{L} = \vec{A} - \vec{H}$ and $L = |\vec{A} - \vec{H}|$. The force exerted by the motor on the cargo is then given by,

$$\vec{F} = -k_{mot}(L - L_{mot})\hat{L} \quad L > L_{mot} \tag{2.1}$$

$$= 0 \qquad\qquad L \leq L_{mot} \tag{2.2}$$

The translation velocity of the center of mass of cargo is given by the over-damped Langevin equation

$$\frac{d\vec{X}}{dt} = \frac{1}{\gamma_c}\left[\sum_{j=1}^{N}\vec{F}_j + \vec{F}_{steric}\right] + \vec{\zeta} \tag{2.3}$$

Here, $\vec{F}_j$ is the force exerted on cargo by the jth motor. $\vec{F}_{steric}$ is the spring-like steric force on the cargo from the microtubule, represented with a high force constant $10k_{mot}$. We note that if the vesicle is deformable the steric spring constant could be significantly smaller. This force is present only if the cargo-microtubule distance is less than the sum of the cargo and microtubule radii. $\vec{\zeta}$ is the random force on the cargo due to collisions with the intracellular medium. We assume a normally distributed noise with zero mean, $\langle\vec{\zeta}\rangle = 0$ and the fluctuation-dissipation relation, $\langle\zeta_\mu(t)\zeta_\nu(t')\rangle = 2\gamma_c k_B T\delta_{\mu\nu}\delta(t-t')$. γ_c is the friction co-efficient for the cargo near microtubule surfaces, assumed to be $\gamma_c = 3\gamma_0$ [126], where γ_0 is the coefficient of viscosity of cargo in bulk, obtained from Stoke's Law [19] as $\gamma_0 = 6\pi\eta_v R$. η_v is the coefficient of viscosity of cytoplasm experienced by cargo. We approximated

η_v to be equal to the coefficient of viscosity of water at room temperature (About 20^0C), $\eta_v = 10^{-3}$ Pa.s. We integrate Eq. 2.3 using the Euler-Maruyama scheme

$$\vec{X}(t+\Delta t) = \vec{X}(t) + \frac{\Delta t}{\gamma_c}\left[\sum_{j=1}^{N}\vec{F_j} + \vec{F}_{steric}\right] + \sqrt{2\gamma_c k_B T \Delta t}\vec{\xi} \tag{2.4}$$

where $\vec{\xi} = (\xi_1, \xi_2, \xi_3)$ and ξ_1, ξ_2, ξ_3 are drawn from a normal distribution with zero mean and unit variance. The Euler-Maruyama scheme is similar to Euler's method of solving differential equations. Euler-Maruyama method is used to solve stochastic differential equations. (For more details, see Chapter: "Introduction to Stochastic Time Discrete Approximation" from Kloeden and Platen, 2011 [74]).

In addition to translational motion, the cargo also has rotational dynamics due to thermal fluctuations and torques from motor forces. Consider a motor at position $\vec{A_i}$ exerting a force $\vec{F_i}$ on the cargo. The torque on the cargo due to this motor is $\vec{r_i} \times \vec{F_i}$. The total torque on the cargo due to all the motor forces is

$$\vec{\tau} = \sum_{i=1}^{N}\vec{r_i} \times \vec{F_i} \tag{2.5}$$

The angular displacement in time Δt taking into account this torque and thermal fluctuations is

$$\Delta\vec{\theta} = \frac{\vec{\tau}}{\gamma_R}\Delta t + \alpha\sqrt{4D_R\Delta t}\,\hat{n} \tag{2.6}$$

Where, γ_R is the friction co-efficient, given by $8\pi\eta_v R^3$. D_R is the rotational diffusion constant of the cargo. α is a calibration constant to match the experimentally measured rotational mean square displacement. We set the rotational diffusion constant (D_R) for lipid cargo to be equal to that of a free spherical bead in solution, which is $k_BT/\gamma_R = k_BT/8\pi\eta_v R^3$. The rotational diffusion constant for rigid cargo bound by one motor was measured [57] to be $7 \times 10^{-2}\,\mathrm{rad}^2 s^{-1}$. In our simulations we used this value to calibrate the rotational diffusion of rigid cargo (see Appendix 2.A). $\hat{n}$ in Eq. 2.6 is given by $\hat{n} = (n_1, n_2, n_3)$ which is a random unit vector in 3-dimensions. To get this, we draw numbers a and b from uniform distribution in the interval [0,1]. Calculate angles $\theta_t = cos^{-1}(2a-1)$ and $\phi_t = 2\pi b$.

Then $\hat{n} = (n_1, n_2, n_3) = (sin\,\theta_t cos\,\phi_t, sin\,\theta_t sin\,\phi_t, cos\,\theta_t)$.

Let $\Delta\theta$ be the magnitude and $\hat{\omega} = (\,\omega_x,\, \omega_y,\, \omega_z\,)$ be the direction of this angular displacement vector $\Delta\vec{\theta}$. The Rodrigues' rotation matrix corresponding to this rotation is [132]

$$R_{\hat{\omega}}(\Delta\theta) = \mathbb{I} + \tilde{\omega}\sin\Delta\theta + \tilde{\omega}^2\,(1 - \cos\Delta\theta) \tag{2.7}$$

where $\mathbb{I}$ is the 3×3 identity matrix and $\tilde{\omega}$ is given by

$$\tilde{\omega} = \begin{bmatrix} 0 & -\omega_z & \omega_y \\ \omega_z & 0 & -\omega_x \\ -\omega_y & \omega_x & 0 \end{bmatrix} \tag{2.8}$$

We update each anchor point position using this matrix

$$\vec{A_i} = \vec{X} + R_{\hat{\omega}}(\Delta\theta)\left(A_i - \vec{X}\right) \tag{2.9}$$

At each time step we also update the anchor positions of each motor on the lipid cargo surface using a similar Brownian dynamics formalism given by

$$\vec{A}(t + \Delta t) = \vec{A}(t) + \Delta l_\theta\hat{\theta} + \Delta l_\phi\hat{\phi} \tag{2.10}$$

where Δl_θ and Δl_ϕ are the small displacements along $\hat{\theta}$ and $\hat{\phi}$ directions in the plane tangential to cargo surface at $\vec{A}(t)$. Δl_θ and Δl_ϕ are given by

$$\begin{pmatrix} \Delta l_\theta \\ \Delta l_\phi \end{pmatrix} = \sqrt{2D\Delta t}\begin{pmatrix} \xi_a \\ \xi_b \end{pmatrix} + \frac{\Delta t}{\gamma_s}\begin{pmatrix} F_\theta \\ F_\phi \end{pmatrix} \tag{2.11}$$

where ξ_a and ξ_b are random variables obtained from normal distribution with zero mean and unit variance. D is the diffusion constant for motor diffusion on cargo surface and γ_s is the friction coefficient given by $\gamma_s = k_B T/D$. (F_θ, F_ϕ) are the components of motor forces along $\hat{\theta}$ and $\hat{\phi}$ respectively which can be obtained from the motor force in Cartesian co-ordinates, $\vec{F} = (F_x, F_y, F_z)$ as follows

$$\begin{pmatrix} F_\theta \\ F_\phi \end{pmatrix} = \begin{pmatrix} \cos\theta\cos\phi & \cos\theta\sin\phi & -\sin\theta \\ -\sin\phi & \cos\phi & 0 \end{pmatrix}\begin{pmatrix} F_x \\ F_y \\ F_z \end{pmatrix} \tag{2.12}$$

At every time step, each bound kinesin motor hydrolyses an ATP molecule with certain probability and attempts to move forward on the microtubule. This stepping probability is a function of the motor force and also the ATP concentration. We have adopted the following relation for the stepping probability [9]

$$p_{step}(_{[\mathrm{ATP}],\vec{F}}) = 1 - e^{-v\Delta t/\delta} \tag{2.13}$$

where δ is the step size, the distance moved by motor after hydrolyzing one ATP molecule ($\delta = 8$ nm [21, 35, 155]). v is the velocity of kinesin motor which is a function of the ATP concentration and motor force and is taken to be

$$v(_{[\mathrm{ATP}],\vec{F}}) = v_0(_{[\mathrm{ATP}]})\tilde{v}(_{\vec{F}}) \tag{2.14}$$

where $v_0(_{[\mathrm{ATP}]})$ is the velocity of motor under no-load condition at a given ATP concentration. The ATP dependence of v_0 is described by the Michaelis-Menten equation

$$v_0(_{[\mathrm{ATP}]}) = \frac{v_{max}[ATP]}{K_m + [ATP]} \tag{2.15}$$

We considered the no-load velocity at saturated ATP concentration to be $v_{max} =$ 800 nm/s [8, 9] and $K_m = 44\,\mu$M [152].

$\tilde{v}(_{\vec{F}})$ gives the force dependence of the velocity. In the hindering direction, we assume [82, 9]

$$\begin{aligned} \tilde{v}_{hind}(_{\vec{F}}) \quad &= \left[1 - \left(\tfrac{F}{F_s}\right)^w\right] \qquad F < F_s \\ &= 0 \qquad\qquad\qquad\quad F \geq F_s \end{aligned} \tag{2.16}$$

F is the magnitude of motor force, $F = |\vec{F}|$. F_s is the stall force, the value of force beyond which kinesin motor stops walking. We considered $F_s = 7$ pN [27, 20, 8] and $w = 2$ [83]. In the assistive direction, velocity is assumed to be independent of force magnitude, $\tilde{v}_{asst}(_{\vec{F}}) = 1$ [8, 9].

Experimentally it is found that a kinesin motor is more likely to detach from the microtubule when one head is detached from the microtubule while trying to take a step than when both the heads are bound to the microtubule [152, 154, 130]. In our model we assume that a motor can detach only when it tries to take a step.

At every time step we first check whether a bound motor tries to make a step with probability $p_{step}(_{[\mathrm{ATP}],\vec{F}})$ using Eq. 2.13. If it tries to take a step, we check whether it detaches from the microtubule before completing the step using a microscopic off-rate whose value is calibrated based on the experimentally observed off-rate as a function of force, F, at saturating ATP concentrations.

$$\epsilon_{micro}(_{\vec{F}}) = \frac{\epsilon_{obs}(_{\vec{F}})}{p_{step}(_{[\mathrm{ATP}]=2\,\mathrm{mM},\vec{F}})} \tag{2.17}$$

$p_{step}(_{[\mathrm{ATP}]=2\,\mathrm{mM},\vec{F}})$ is the probability to step forward in time step Δt at high ATP concentration of 2 mM.

For hindering forces, we used the following relationship between observed off-rate and magnitude of motor force F developed [15, 44, 129] based on Kramer's theory [81] and used in several studies [82, 76, 9]

$$\epsilon_{obs}^{hind}(_{\vec{F}}) = \epsilon_0 e^{F/F_d} \tag{2.18}$$

ϵ_0 is the off-rate under no load condition. We used $\epsilon_0 = 0.79\,s^{-1}$ [9, 8]. F_d is the detachment force. We approximated F_d to be equal to the stall force F_s. For assistive forces, the relationship between observed off-rate and magnitude of force is taken to be [8, 9]

$$\epsilon_{obs}^{asst}(_{\vec{F}}) = \epsilon_0 + 1.56 \times 10^{12} F \tag{2.19}$$

Our model could easily be extended to incorporate more detailed chemo-mechanical models of motors [28, 29]. In chapter 6 we explain the incorporation of more details to the model, specifically a three dimensional lattice structure and different mechanical models of kinesin motors.

Computational code for this model is available at https://github.com/nsarpangala/lipid-cargo-transport. See Fig. 2.2 for a flow chart of this algorithm.

2.3 Conclusions

In this chapter, we presented details of our Brownian dynamics model. Here we consider cargo as a sphere and explicitly simulate the motion of motor anchor

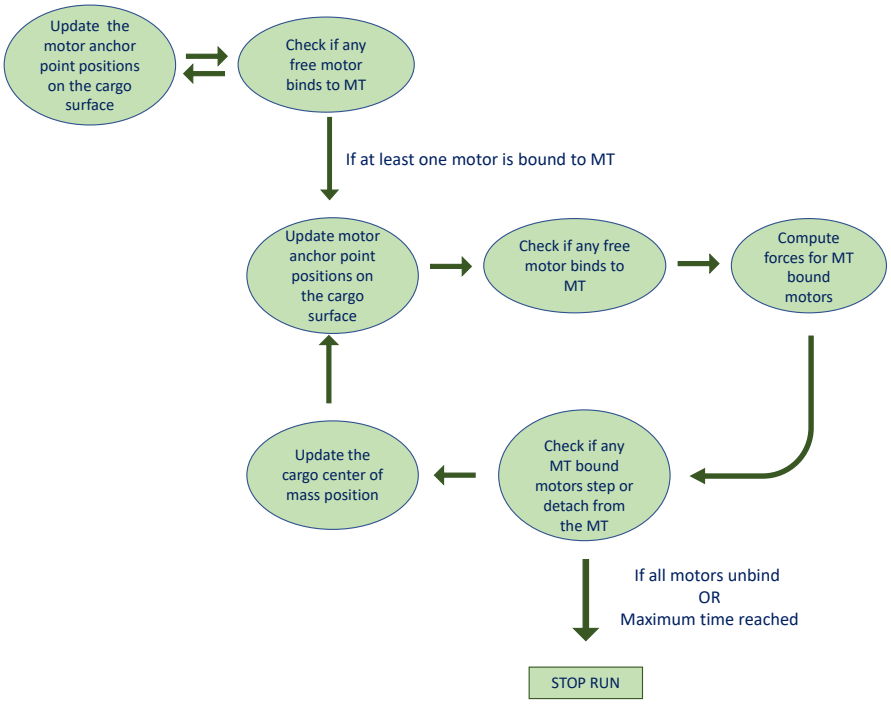

Figure 2.2: **The flow chart of the simulation.** The cargo is held near the microtubule until at least one motor is bound. Once a motor is bound, we loop over the series of steps shown in the middle until either all motors are unbound or maximum time is reached. At regular time intervals, we record relevant data like the cargo center of mass, anchor positions of motors on cargo surface, head positions of bound motors on the microtubule.

positions by allowing free diffusion for unbound motors and diffusion biased by exerted forces for bound motors. The diffusion constant for this motion is determined by the cargo surface fluidity. We also accounted for the force and ATP dependence of the bound motor's off-rate and stepping rate. The spherical cargo's position was then updated by an overdamped Langevin equation depending on the net force exerted by all bound motors. Rotational diffusion of the cargo due to the torque from motor forces and thermal fluctuations was also included. With

this model one can analyze the dynamics of the motors as they diffuse on the surface, their binding and unbinding from the filament, the forces experienced by individual motors, the total distance and velocity of cargo as a function of motor diffusion constant, motor density, and ATP concentration. We then applied it to understand team dynamics under different physiological scenarios.

Notes

2.A Notes on the assumptions in the computational model

2.A.1 We neglect the deformation of vesicle due to motor forces.

Application of a point force on the vesicle (the cargo) surface leads to shape deformation which could develop as narrow membrane tubes (tethers) at sufficiently high force magnitudes [37, 118, 123, 148]. There have been observations that teams of kinesin motors can pull membrane tubes out of a vesicle [89]. This raises the question as to whether we should consider the alteration in vesicle shape due to tether formation in our computational model. Previous analytical works [37, 118] have shown that the force magnitude needs to be greater than a critical value, $f_c = 2\pi\sqrt{\kappa_c \sigma}$ to pull a nanotube out of a membrane with bending rigidity κ_c and surface tension σ. For typical values, $k_c = 20k_BT = 10^{-19}$ J [148], $\sigma = 10^{-5}$ Nm^{-1} [38, 37] the critical force is $f_c = 8.8$ pN which is higher than the stall force of kinesin (7 pN). This critical value that we computed is lower than the estimated value in at least one other study [89, 37]. We can see from the force distributions in Fig. 3.2.0 (b & c) that the typical single motor force values are much lower than this critical value. Hence we have neglected the tether formation in our model.

2.A.2 Estimation of rotational diffusion of cargo.

We expect the rotational diffusion to be minimum for a rigid cargo, increase with an increase in cargo surface fluidity and approach the value for free bead in solution at very high cargo surface fluidity. For lipid cargo with high motor diffusivity, one might expect that such rotational diffusion of cargo only renormalizes the diffusion constant of motors on the surface (at most by a factor of 2) but doesn't induce any qualitative change in the motor availability at the access region.

The rotational diffusion constant of a rigid cargo associated with microtubule with a single motor has been measured experimentally to be $D = 7 \times 10^{-2}\,\mathrm{rad}^2 s^{-1}$ for a cargo of about 1.26 μm in diameter [58]. Since this diffusion constant was measured for a cargo of about half-micron radius, if we take into account the possibility that diffusion constant scales as $1/R^3$, for $R = 0.25\,\mu m$, we may take $D_{0.25\,\mu m} = 1.12\,\mathrm{rad}^2\mathrm{s}^{-1}$. The time required for a cargo to rotate by 90^o with this diffusion constant is $\frac{\pi^2}{16 D_R} = 0.55 s$ which is in the order of the lifetime of single kinesin motor in our simulations (lifetime of kinesin is about 1 s at [ATP] = 2 mM and about 10 s at [ATP] = 4.9 μM). Since how rotational diffusion constant of bead changes as a function of cargo radius is not experimentally measured yet, for our simulations we took rigid cargo diffusion constant D_R to be $7 \times 10^{-2}\mathrm{rad}^2 s^{-1}$ even for $R = 250$ nm (We also used $D_R = 1.12$ rad$^2 s^{-1}$ and compared different metrics like force distribution and off-rate and didn't find considerable difference).

Similarly we can estimate how much is the rotational angular velocity of cargo due to the torque from motor forces. Assume that a microtubule bound motor exerts a torque $\vec{\mathcal{T}}$ on the cargo. Angular velocity of cargo due to this torque is

$$\frac{d\vec{\theta}}{dt} = \frac{\vec{\mathcal{T}}}{8\pi\eta_v R^3} \tag{2.20}$$

Typical value of tangential component of motor force is $f_{tan} = 1$ pN. So the typical magnitude of the torque on the cargo due to this force is $\mathcal{T} = R f_{tan} = 2.5 \times 10^{-19}$ Nm. Substituting this in Eq. 2.20 we get the typical magnitude of angular velocity due to torque from motor forces to be equal to 636 rad s^{-1}. This

is a non-negligible angular velocity, for example, the rotation of the cargo due to motor forces in 1 s is 636 rad.

Typical magnitude of the torque, $|\vec{\mathcal{T}}| = R \times f_t$ where f_t is the typical magnitude of tangential force (about 1 pN). So $\frac{d\vec{\theta}}{dt} \propto R^{-2}$. Distance traveled by motor on the cargo surface, arc length $\propto R\frac{d\vec{\theta}}{dt}$. Hence arc length $\propto R^{-1}$. Thus we might expect the rotational distance covered to decrease with increase in cargo radius.

Bench mark test and calibration: Mean-Squared-Angular-Displacement

Let $A(\vec{t'})$ be the anchor position of a motor on the cargo surface and $\hat{a}(t')$ represent the unit vector representing the direction of this anchor position with respect to the cargo center of mass.

Define the angular displacement vector of a motor anchor point as [67]

$$\vec{\Theta}(t) = \sum_{i=0}^{n_t} \Delta\vec{\Theta}(i\Delta t) \tag{2.21}$$

Where $n_t = t/\Delta t$. The displacement vector $\Delta\vec{\Theta}(t')$ has a magnitude, $|\Delta\vec{\Theta}(t')| = \cos^{-1}\left[\hat{a}(t' - \Delta t) \cdot \hat{a}(t')\right]$ and a direction given by $\hat{a}(t' - \Delta t) \times \hat{a}(t')$. We take $\Delta\vec{\Theta}(0) = 0$.

We then compute the mean squared angular displacement [67]

$$\left\langle \vec{\Delta}\Theta^2(t) \right\rangle = \left\langle \left[\vec{\Delta}\Theta(t) - \vec{\Delta}\Theta(0)\right]^2 \right\rangle \tag{2.22}$$

As per the Stokes-Einstein-Debye relation we expect the mean squared angular displacement to grow as [67]

$$\left\langle \vec{\Delta}\Theta^2(t) \right\rangle = 4D_R t \tag{2.23}$$

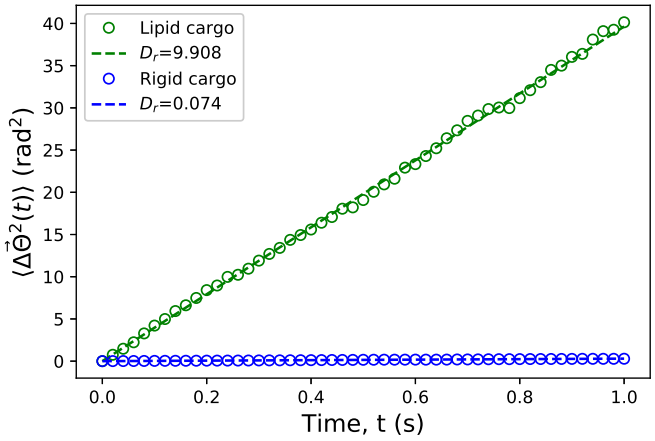

Figure 2.A.1: **Benchmark test to verify correct implementation of rotational diffusion.** We ran simulations of cargo dynamics with just rotational diffusion (no motor bound to MT, no translational diffusion of cargo, no diffusion of motor on cargo surface) and measured the mean-squared-angular-displacement (MSAD, $< \Delta\vec{\Theta}^2 >$) of motor anchor point. Ensemble size = 200. Then we fit MSAD to $4D_R t$ and extracted the rotational diffusion constant, D_R, to verify that we implement the desired rotational diffusion.

Chapter 3

Effect of surface fluidity on cargo transport by identical motor teams

In this chapter, we will discuss how lipid membranes influence cargo transport by teams of kinesin motors where each motor is assumed to have the same single motor properties. This chapter is a reproduction of the work presented in Sarpangala and Gopinathan, *PLos Comput. Biol*, 2022 [125]. The co-author listed in this publication directed and supervised research.

3.1 Introduction

Several theoretical and *in vitro* experimental studies [40, 122, 69, 117, 105] indicate that the collective behavior of motors is critically influenced by their coupling to each other resulting in observable effects in transport speeds and run lengths. For example, it is known that non-cooperative kinesin motors coupled together by a rigid cargo interfere with each other's functioning leading to enhanced detachments and lowered run lengths [40, 122, 69]. How then are *in vivo* cargoes such as membrane-bound vesicles and organelles typically carried over long distances by teams of kinesin motors [103, 13]? A fluid membrane present in most *in vivo* cargoes may make more motors available for binding at the filament either by

dynamic clustering of motors [71, 25] or membrane induced clustering of motors into micro-domains [75, 119] thereby enhancing processivity. Alternatively or in addition, there could be other lipid membrane coupling dependent physical mechanisms that directly affect single motor functioning and thereby promote teamwork. Studies on transport *in vivo* could address these questions directly, but the environmental complexity makes it difficult to disentangle fundamental phenomena of physical origin from the effects of other regulatory mechanisms [41]. *In vitro* systems, which offer cleaner insights, include microtubule gliding assays on flat bilayers with embedded motors [55, 98, 71, 106], motor driven nanotube extraction from vesicles [88] and more recently even membrane covered beads carried by kinesin motors [94]. Studies of these systems and related models have generated a variety of interesting and sometimes conflicting results on cargo run lengths and velocities in the presence of membrane fluidity [55, 94, 113, 25]. These results are also obtained under different conditions of cargo geometry, motor density, cargo surface fluidity and environmental factors like ATP concentration. In order to reconcile them, we need an understanding of the relative importance and interplay of these factors and their effects on the number of engaged motors and the loads they experience, which in turn influences their collective speed and processivity. More importantly, to uncover any physical mechanisms present in teams of motors that directly affect single motor functioning and thereby enhance teamwork, we need to be able to monitor both single motor dynamics and collective cargo transport simultaneously.

Here, we used Brownian dynamics model developed in Chapter 2 to accomplish this goal. Our model and problem are overall quite similar to Bovyn *et. al.* [25] which also implemented overdamped Langevin dynamics of motors on an undeformable, spherical lipid cargo surface. While there are minor differences between our models such as in the details of the load dependence of the motor unbinding rates and the incorporation of ATP, we do not expect significant quantitative differences. Indeed, measurements of the same quantities such as run lengths and single motor binding times are consistent between our studies. The major difference with

our work lies in the focus of their study which was the effect of surface fluidity on the availability of motors for both clustered and dispersed motors and how this influenced the trade-off between binding rates from solution and run length. While we also consider the availability of motors, a major focus in this work is on the effect of fluidity at the single motor level. This includes effects on the mechanical interference between motors which affects their load-sharing and thereby single motor processivity as well as collective force generation. Another difference is that we specifically consider the effects of varying ATP concentration. Finally, we study the relative importance of these effects and how they act synergistically at the level of the collective to influence cargo transport.

Specifically, our model enabled us to focus on the dynamics of the motors as they diffused on the surface, their binding and unbinding from the filament and the forces experienced by individual motors, as a function of motor diffusion constant, motor density and ATP concentration. We connected these characteristics at the individual motor level to the effect of surface fluidity (inverse viscosity proportional to the diffusion constant) on the collective behavior of motors at the cargo level by analyzing transport properties such as the average number of bound motors, collective force generated against load, speed and distance traveled (run length). We uncovered two salient features, the reduction of interference and the cooperative increase of on-rates. Our simulations showed explicitly that surface fluidity leads to the reduction of negative mechanical interference between kinesins, characterized by lower forces on individual motors and a significant drop in antagonistic forces between motors. This allows teams of fluid-coupled motors to more fully exploit load sharing without inter-motor interference. This decreases single motor off-rates and increases processivity. Our simulations also showed that the fluid surface allows for the clustering of motors at a well defined location on the surface relative to the microtubule and that the fluid-coupled motors can exert more collective force per motor against loads. Interestingly, increasing numbers of bound motors pull the cargo closer to the microtubule, increasing the on-rates of unbound motors, resulting in a cooperative increase in bound motor numbers that depends on 3D cargo geometry. Surface fluidity also makes more motors available for binding,

as expected, and as indicated by previous studies [71, 113, 25]. However, this effect, by itself, is significant only at lower ATP concentrations (and/or very high motor numbers) when the effective timescale for diffusion and binding is less than the unbinding time. In fact, we estimate that the reduction in interference is relatively the most important effect under physiological conditions of high ATP and low motor numbers. Taken altogether these effects can cooperatively result in increased processivity and collective mechanical force production against load with an increase in fluidity for teams of molecular motors, with both *in vivo* and technological implications.

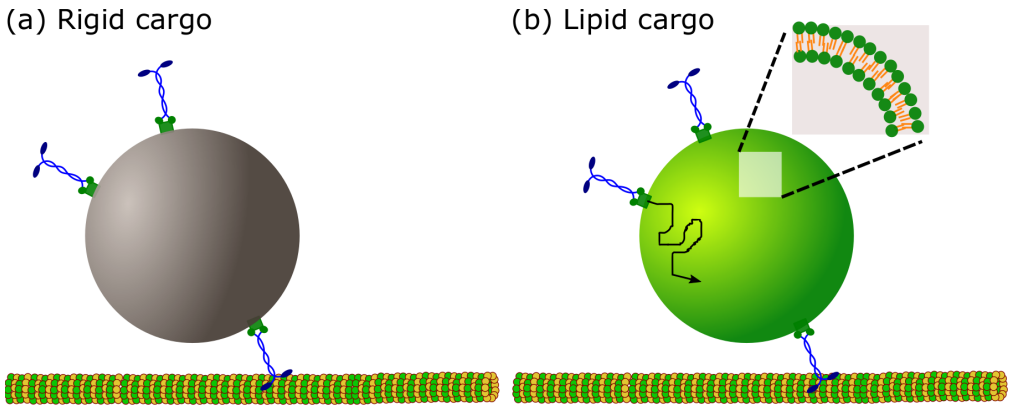

Figure 3.1.1: **Schematics of cargoes considered in the study. (a)** Rigid cargo (membrane-free cargo). Molecular motors are permanently attached to random locations on the cargo surface. **(b)** Fluid/Lipid cargo (membrane-enclosed cargo). Molecular motors diffuse on the cargo surface. Inset of Fig. 1(b) The lipid bilayer that forms the fluid cargo surface. Reprinted with permissions from Sarpangala and Gopinathan, *PLos Comput. Biol.*, 2022 [125]. CC-BY-4.0.

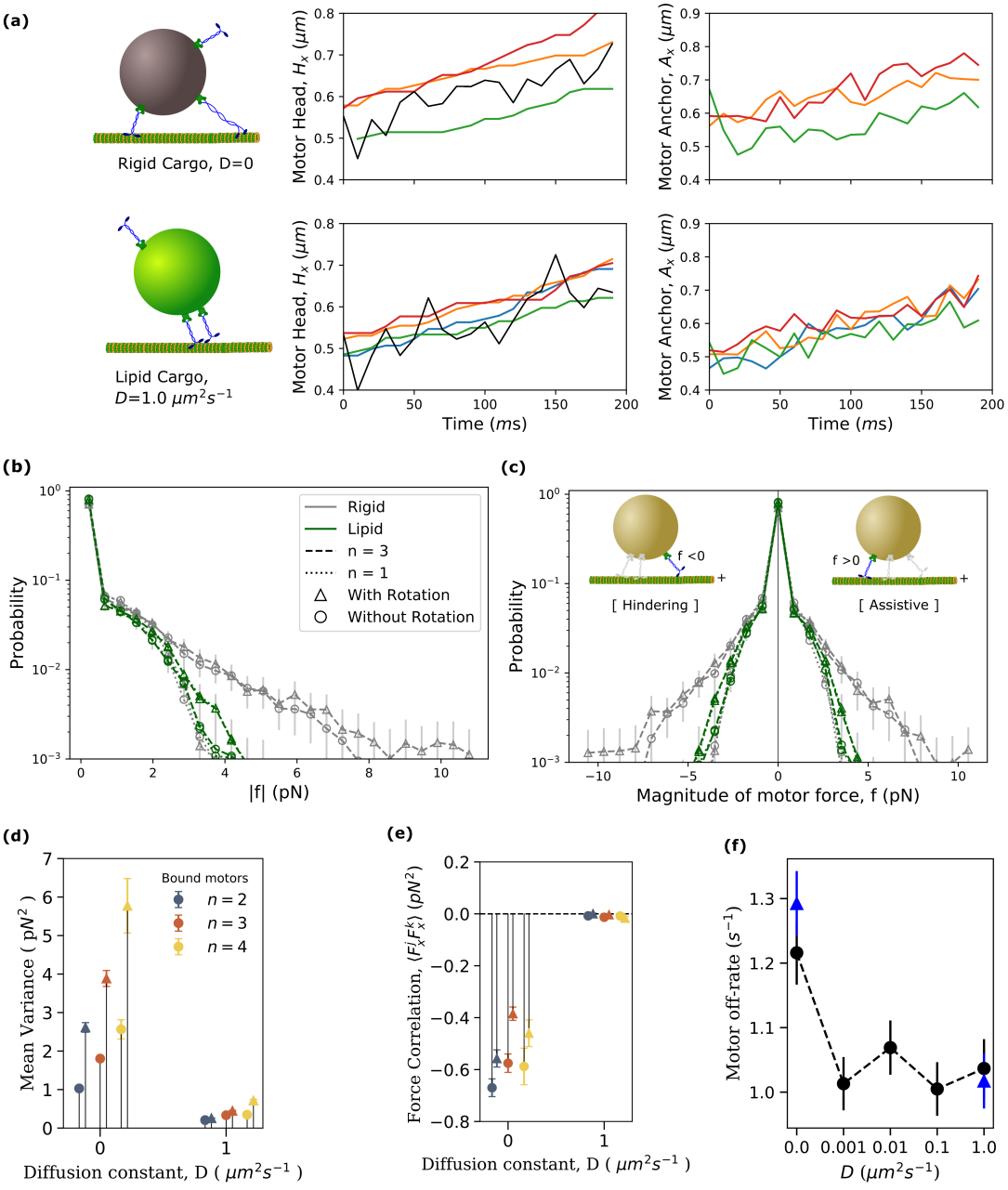
(a)
Rigid Cargo, D=0
Lipid Cargo,
D=1.0 μm²s⁻¹
Motor Head, Hx (μm)
Motor Anchor, Ax (μm)
Time (ms)
(b)
Probability
|f| (pN)
Rigid
Lipid
n = 3
n = 1
With Rotation
Without Rotation
(c)
Probability
Magnitude of motor force, f (pN)
f <0
f >0
[Hindering]
[Assistive]
(d)
Mean Variance (pN²)
Diffusion constant, D (μm²s⁻¹)
Bound motors
n = 2
n = 3
n = 4
(e)
Force Correlation, ⟨F_x^i F_x^k⟩ (pN²)
Diffusion constant, D (μm²s⁻¹)
(f)
Motor off-rate (s⁻¹)
D (μm²s⁻¹)

Figure 3.2.0: **Surface fluidity reduces the negative interference between bound kinesin motors which leads to reduction in motor off-rate. (a)** Typical trajectories for a rigid (top row) and a lipid cargo (second row). Motor head position subplots (middle column) include the x-positions of the center of mass of cargo (black lines) and head positions of motors on the microtubule (colored lines). The corresponding x-component of motor anchor positions (right column) on the cargo are also shown. **(b)** Distributions of the absolute magnitude of the force experienced by motors in rigid and lipid cargoes (including without cargo rotation) at a fixed number of bound motors ($n = 3$). Distribution for singly bound motor carrying a rigid cargo is also shown for comparison. We first collect $S = 10000$ force values randomly drawn from 200 cargo runs. We then bootstrap this (bootstrap sample size = 1,000 and the number of bootstrap samples = 10) to get the mean distribution and standard error of the mean. **(c)** Distribution of magnitude of motor forces when they specifically experience hindering loads ($f < 0$) and assistive loads ($f > 0$). Cartoon inside shows a possible scenario where the colored motor experiences hindering and assistive load. **(d)** The mean variance of forces among bound motors in rigid ($D = 0$) and lipid cargoes ($D = 1\,\mu m^2 s^{-1}$) with (triangles) and without cargo rotation (circles). Mean variance was calculated as $\frac{1}{S}\sum_{i=1}^{S}\sigma^2_{|f|}(i)$ where the summation is over all the sample time points when the number of bound motors is n. $\sigma^2_{|f|}(i)$ is the variance in the magnitude of force experienced by the n bound motors at i^{th} sample. Sample size $S = 10000$ drawn from 200 cargo runs. **(e)** Mean value of the correlation between the x-components of motor forces, $\langle F_x^j F_x^k \rangle$, averaged over motor pairs and time points with (triangles) and without cargo rotation (circles). Sample size $S = 10000$ drawn from 200 cargo runs. **(f)** Average value of motor off-rate as a function of fluidity of cargo surface with (triangles) and without cargo rotation (circles). ($S = 580$ from 200 cargo runs). Data for all the plots were obtained from the simulation of transport of cargoes with $N = 16$ motors at high ATP concentration of 2 mM. Data sampling rate was 100 s^{-1}. Reprinted with permissions from Sarpangala and Gopinathan, *PLos Comput. Biol.*, 2022 [125]. CC-BY-4.0.

3.2 Results and Discussion

3.2.1 Surface fluidity reduces negative interference between bound kinesin motors

We first addressed the question of whether the fluidity of the cargo surface has any influence on the functioning of a bound kinesin motor. We expected that the motor attachment point's freedom to move on the lipid cargo surface in response to forces could suppress strain and reduce the forces experienced by the motor. We also expected that the surface fluidity would allow bound motors to alter their spatial distribution relative to the cargo and each other thereby also changing the forces they experienced. We started by looking at the positions of motor heads on the MT and anchor points on the cargo during a typical cargo run for a rigid and a lipid cargo (Fig. 3.2.0(a); see Fig. 3.E.1 for a longer time window). From the motor head position subplots, it can be seen that motors on a rigid cargo are more spread apart and can be located opposite to each other relative to the cargo center of mass while on lipid cargos, bound motors tend to be closer and on the same side, in front of the cargo. This supports our expectation that the lipid membrane can alter the relative positioning of the motors which could lead to different strain forces on the motors.

To explore the forces experienced by motors more quantitatively, we computed the distribution of forces experienced by a single motor when it is part of a team of n motors that are simultaneously bound to the microtubule. This distribution, shown for $n = 3$ bound motors in Fig. 3.2.0(b), is broader, reflecting larger forces, for a motor on a rigid cargo compared to any of the lipid cargoes. The lipid cargo motor force distributions is, in fact, comparable to that for a single bound motor carrying a rigid cargo. A rigid coupling of motors, therefore, results in individual bound motors experiencing higher forces than when they are singly bound to cargo, indicating negative interference. The introduction of surface fluidity appears to reduce this interference by effectively decoupling the motors, consistent with our expectations. This reduction is also apparent in the distribution of forces experienced both against (hindering) and in (assistive) the direction of processive

motion (Fig. 3.2.0 (c)).

The reduction in forces due to fluidity is also evident in the fraction of non-negligible forces (Fig. 3.E.2), which we take to be forces with a magnitude $\geq$ 1% of F_s, the stall force of the kinesin motor (Fig. 3.E and Fig. 3.E.3 show similar fractions in hindering and assistive directions). For rigid cargo, this fraction increases as a function of the number of bound motors, n, indicating negative interference between motors. In the presence of surface fluidity, however, no such increase in the fraction with n is apparent, indicating a reduction of negative interference. In fact, the fraction decreases with n at high surface fluidity ($D = 1\,\mu m^2 s^{-1}$), which is likely due to the decrease in the average force experienced by the motors in the presence of multiple bound motors (Fig. **??**). While the decrease in average force occurs for rigid cargo as well, the increase with n due to negative interference dominates.

The variance between the individual forces experienced by simultaneously bound motors is also a measure of negative interference as it quantifies the deviation from perfect load-sharing where the variance should be zero. The mean variance over all sampled instances with n bound motors shows a dramatic decrease at higher fluidity ($D = 1\,\mu m^2 s^{-1}$) compared to the rigid cargo case (Fig. 3.2.0(d), see Appendix 3.D for detailed description of this and other force related metrics used in this section). In fact, even the presence of a small amount of fluidity accounts for most of the significant drop in variance (Fig. 3.E.5) indicating that fairly good load-sharing can be achieved with modest fluidity. We also quantified negative interference more directly by studying whether individual motors were acting antagonistically, *i.e.*, exerting forces in opposite directions. To do this, we computed the correlation between the x-components of bound motor forces $\langle F_x^j F_x^k \rangle$ averaged over different motor pairs (j, k) and time (Fig. 3.2.0(e)). We see that this correlation is highly negative for rigid cargo indicating opposing motor forces while it is negligible in the presence of fluidity indicating motors on the same side of the cargo pulling in the same direction. Taken together, our results show that interference dominates over load sharing for rigid cargo while increasing surface fluidity reduces

this interference and promotes load-sharing.

Next, we addressed the implications of the reduction in negative interference for the functioning of motors in the context of transport. The off-rate of a kinesin motor increases with the magnitude of the force that it experiences and also depends on its direction [82, 76, 9, 8, 129]. The observation that surface fluidity reduces negative interference leads us to expect that this will also lead to lower off-rates for individual motors. We measured the mean off-rate of motors as the inverse of the mean time spent by individual motors between a binding and subsequent unbinding event. We found that bound motors on fluid cargoes do indeed have lower off-rates than those on rigid cargoes (Fig. 3.2.0(f)). Consistent with our findings for the forces and interference, the introduction of a small amount of fluidity accounts for most of the significant drop in off-rates with no significant variation with increasing diffusivity.

The forces that motors feel and the off-rate of motor is a function of the spring constant of the kinesin coiled-coil region. In fact, previous studies [40, 16] have found that off-rate of ensemble of motors and the transport properties of cargo are sensitive to the stiffness of the motor. Our simulations (see Fig. 3.E.21) indicate that average single motor off-rate can increase by almost 20% for a change in the motor stiffness from 0.1 pN/nm to 0.5 pN/nm for rigid cargo, while for lipid cargo the change is not significant, which is again consistent with the picture of the lipid membrane suppressing strain in the motors.

We also ran simulations at different cargo sizes to determine how the single motor metrics change. The distribution of forces (Fig. 3.E.6 (a) and (b)) shows no clear trend except perhaps for a marginal increase in larger forces with decreasing radii for lipid cargo, which could be due to the steric constraints becoming more important. Interference between motors, quantified by the force correlations (Fig. 3.E.6 (c)), show negligible correlations between motors for lipid cargo at any size, while for rigid cargo, the interference appears to increase with size, consistent

with potentially increased spacing between motors. Motor off-rate (Fig. 3.E.6 d) decreases as a function of cargo size for both rigid and lipid cargo but the off-rate of motor in lipid cargo is lower than rigid cargo for all cargo sizes, which is again consistent with picture of reduced interference and greater load-sharing with a lipid cargo.

We also took the opportunity to explore the impact of cargo rotations on motor forces. While cargoes do rotate considerably during the course of a typical cargo run and especially at intersections or obstacles [48, 17], it is not clear whether this rotation impacts transport metrics like motor off-rate, force distribution and cargo runlength. Answering this question is also interesting from a modeling perspective and helpful for improved analytical approximations. Disallowing rotational motion of the cargo in our simulations leads to a slight decrease in the magnitude of motor forces, as is apparent in $n = 3$ cases shown in Fig. 3.2.0 (b and c). In our simulations and in *in vitro* experiments in aqueous media, the load due to viscous forces is low and the origin of higher forces is thermal fluctuations [151] and negative interference between motors. The higher forces experienced by motors in the presence of rotation is therefore likely due to rotational diffusion adding additional noise into the cargo dynamics. It is to be noted that the reduction in forces due to removing cargo rotations is slightly more pronounced for rigid cargo but in both cases the reduction is small compared to the reduction due to fluidity. The variance of motor forces (Fig. 3.2.0(d)) also decreases when we remove rotational diffusion because of the decrease in the noise though the effect is not significant for lipid cargo. Similarly, the magnitude of force correlations (Fig. 3.2.0(e)) increased when we removed rotation for rigid cargoes while the correlations are essentially the same and close to zero for lipid cargo. These effects arise because the removal of rotational diffusion removes a source of uncorrelated noise. Finally, we compared the change in motor off-rate with and without incorporating rotation in our model (Fig. 3.2.0(f)). We notice that rotation may increase the off-rate slightly (by about 5%) for rigid cargo, while the off-rate of motors on lipid cargo is unaffected by cargo rotation. Thus, it seems that ignoring rotation of cargo leads to no qualitative changes and is a perfectly good quantitative approximation for

lipid cargo and a reasonable one that slightly underestimates forces and off-rates for motors on a rigid cargo. It is to be noted that rotations can play a much more important role in enhancing binding rates from solution as seen in [25], but for lipid cargo, the diffusion of motors dominates over rotations of the cargo, and therefore rotations play a negligible role. In what follows, results presented include rotation of the cargo and are essentially very similar to the results without rotation unless explicitly noted.

Overall, our modeling indicates that increasing surface fluidity reduces inter-motor interference and promotes load-sharing leading to reduced off-rates and potentially longer processive runs for individual motors.

3.2.2 On-rate of a motor increases with the number of bound motors for fluid cargo

The run length of a cargo carried by a team of motors depends on the interplay between the off-rates and on-rates of individual motors [76]. The on-rate of a motor, typically considered to be independent of the number of other bound motors, depends on its intrinsic binding rate when it is within reach of the MT. The region of the cargo surface (or access area) from where an anchored kinesin can reach the MT is defined, in our model, by the set of points on the surface at a distance less than or equal to the rest length of the motor ($L_{mot} = 57$ nm). For a cargo bound to the MT with one or more motors, this access area is a function of the cargo geometry and the proximity of the cargo to the MT [119, 93, 71]. For rigid cargo, motors can only bind if they happen to be anchored in the access area while for fluid cargo, motors can diffuse in and out of the access area. For a given motor type with a fixed intrinsic binding rate and a given cargo geometry (a sphere here), the access area is then simply a function of the distance of the cargo from the MT. Interestingly, our measurements of the average distance of the center of mass of the cargo from the MT indicated that the cargo comes closer to the microtubule as the number of bound motors increases (Fig. 3.2.1(a)). This decrease in distance arises from the increase in the net vertical component of the average force due to

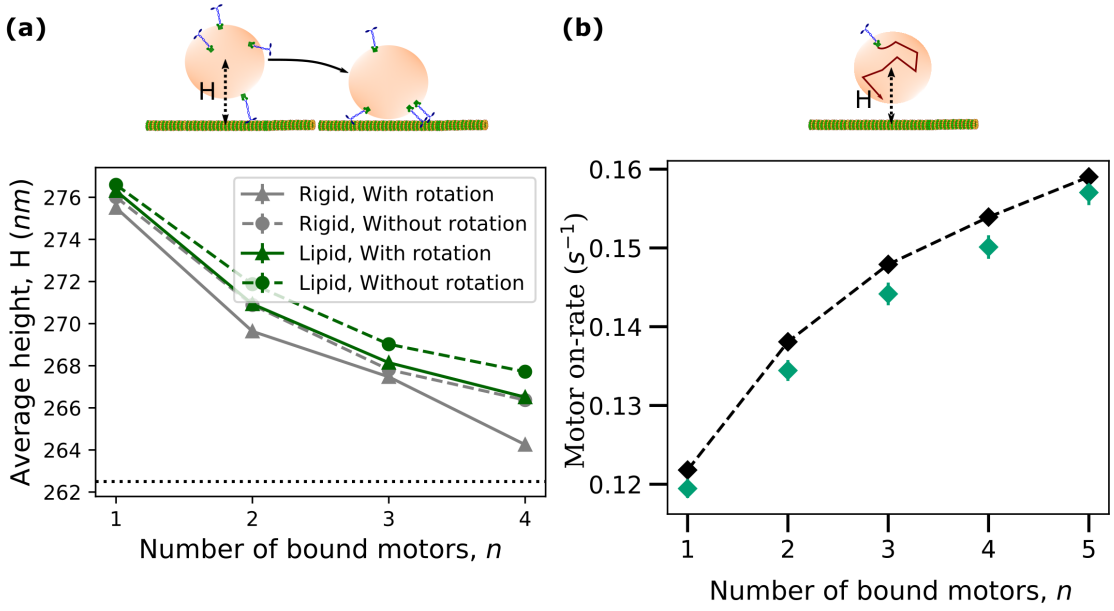

Figure 3.2.1: **On-rate of a motor increases with the number of bound motors for fluid cargo. (a)** Average measured distance (H) of the center of mass of cargo from MT as a function of the number of bound motors and fluidity. Horizontal line indicates the height below which the cargo experiences steric interaction from the MT. Data were obtained from the simulation of transport of cargoes with $N = 16$ motors at high ATP concentration of 2 mM. Data sampling rate was 100 s^{-1}. **(b)** Computational measurements of single motor on-rate (green diamonds) and analytical approximation (black dashed line with diamond). ($D = 1\,\mu m^2 s^{-1}$, $S = 10000$) using the cargo height for a given n from the data in (a). Error bars for all plots represent the standard error of the mean. Rotation of cargo was not considered in the on-rate measurement simulations for (b). Reprinted with permissions from Sarpangala and Gopinathan, *PLos Comput. Biol.*, 2022 [125]. CC-BY-4.0.

an increased number of motors which serves to counteract cargo fluctuations away from the MT. We also note that cargoes with low surface fluidity are closer to the MT than the cargoes with high surface fluidity, especially for high numbers of bound motors. This is because motors on fluid cargoes can relax their tension by sliding on the cargo surface allowing for larger fluctuations (Fig. 3.E.7 and Fig. 3.E.8) and therefore a higher average distance from the MT. We also note that rotations of the cargo seem to allow the cargo to get slightly closer to the MT, presumably because the extra forces due to rotational diffusion serve to increase the net vertical component of the average force as well.

Thus, for both rigid and fluid cargo, as the number of bound motors increases, the cargo approaches the MT leading to an increase in the access area. We expect that this should lead to an increase in the on-rate of an individual unbound motor because its likelihood of being in the access area is increased. We verified this by measuring the on-rate of a motor diffusing on the surface of a cargo held at specific distances from the MT (Fig. 3.2.1(b)) that correspond to different numbers of bound motors (from data in Fig. 3.2.1(a) for $D = 1\,\mu m^2 s^{-1}$). Here we chose a high diffusion constant for simplicity and measured the mean time required for a randomly placed motor to diffuse and bind to the MT. Indeed, we see that the effective on-rate of the motor, calculated as the inverse of this mean time, increases with decreasing distance corresponding to increasing numbers of bound motors (Fig. 3.2.1(b)). To show that the quantitative increase in on-rate was explained by the decreasing distance, we also analytically estimated the change in on-rate. Since the average time spent by a motor in the access area before binding to the microtubule is approximately proportional to the ratio of access area to total area in the high diffusion constant limit, we estimated that the effective on-rate is $\pi_{ad} = \pi_0(S_a/S_T)$, where $\pi_0 = 5\,s^{-1}$ is the intrinsic binding rate, S_a is the access area and $S_T = 4\pi R^2$ is the total surface area of the cargo. Such an assumption is reasonable for cargo surfaces with high diffusion constants where the time scale for motor diffusion across the cargo surface is small as seen in previous studies [119, 97, 71]. By computing the access area numerically for different cargo distances, we were able to estimate π_{ad} corresponding to different numbers of bound

motors. The rather good agreement with the measured values from simulations (Fig. 3.2.1(b)) indicates that the increase in on-rate is captured by the effects of increased access area. It is to be noted that the rate at which the cargo transitions from being bound by n to $n+1$ motors can be calculated from this on-rate, the off-rate and the number of unbound motors available for binding (details in Appendix 3.A and data in Fig. 3.E.9.)

Our results reveal a positive feedback effect at play. As the number of bound motors increases, the cargo gets closer to the MT and the on-rates of each of the remaining motors increase which further increases the number of bound motors. Interestingly, the apparently small change in cargo height can have a big effect on the overall processivity of the team as discussed in the subsequent section on the contributions of different effects to overall run length.

However, it should be noted that this positive cooperativity that we observe is conditioned on our assumption that an unbound motor can bind to any position on the microtubule at a distance less than the rest length of the motor (L_{mot}). For situations where a large number of protofilament tracks are not available, such as myosin motors on actin filaments, steric occlusion could be important. For instance, studies [97] on myosin binding to actin also found that the cargo comes closer to the filament with an increase in the number of bound motors, but this leads to a decrease in the on-rate of motors because of increased steric occlusion from the cargo itself.

3.2.3 Surface fluidity increases the availability of motors for binding

A cargo cannot, however, benefit from the positive feedback noted in the last section, unless it makes a sufficient number of motors available for binding. We expect that the diffusion of motors on the cargo surface should lead to a greater availability of motors in the access region and hence a higher number of bound motors compared to rigid cargo with the same overall number of motors. We also expect that this will be true only if τ_{bind} - the typical time for any one of the

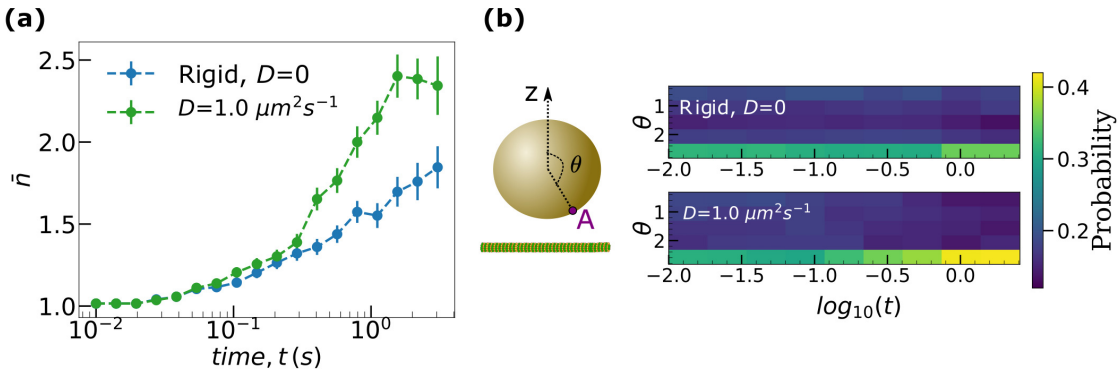

Figure 3.2.2: **Surface fluidity increases the availability of motors for binding.** **(a)** Ensemble average of the number of bound motors, $\bar{n}$ as a function of time (s). Error bars represent the standard error of the mean. **(b)** Spatial distribution of the kinesin motors on cargo, computed as the probability of locating motors as a function of the polar angle θ and time, t. θ is the polar angle of the motor, measured with respect to z axis perpendicular to the microtubule and passing through the center of the cargo. Data was obtained from the transport of cargoes with a total of $N = 16$ motors at [ATP]=2 mM. Reprinted with permissions from Sarpangala and Gopinathan, *PLos Comput. Biol.*, 2022 [125]. CC-BY-4.0.

unbound motors to bind to the microtubule is less than $\tau_{off} = 1/\epsilon_0$ - the typical time for a given bound motor to detach. The relative values of these two timescales are set by parameters such as the number of motors (N), the radius of cargo (R), and the ATP concentration. For instance, raising the motor density (say by raising N) will result in a higher effective on-rate and a decreased τ_{bind}, while decreasing the ATP concentration, lowers the off-rate and raises τ_{off}.

We first looked at a parameter set (N=16 [ATP]= 2 mM) satisfying the condition $\tau_{bind} < \tau_{off}$ (see Appendix 3.A for details of estimates). Fig. 3.2.2(a) shows that, while the average number of bound motors, $\bar{n}$, increases with time for both rigid and fluid cargoes, the fluid cargo indeed accumulates more motors. The spatial distribution of motors in Fig. 3.2.2(b) further highlights the difference between rigid and fluid cargoes with the probability of finding motors near the microtubule on a fluid cargo being larger at late times than for rigid cargo. It is to be noted that the slight increase at late times for rigid cargoes is simply due to the higher contribution to the average of cargoes, that happen to have motors clustered together, surviving for longer times.

To further test the dependence of motor accumulation on the relative values of the two time scales, we considered four other sets of physiologically relevant parameters of N and [ATP] that had different relative magnitudes of τ_{off} and τ_{bind} (shown in Table 1, Appendix 3.A) As predicted, there is no statistically significant difference in the average number of bound motors as a function of diffusivity (see Fig. 3.2.3(a)) for cases when $\tau_{off} \approx \tau_{bind}$ ($N = 4$, [ATP]= 2 mM and 100 μM). The number of bound motors, however, increases as a function of diffusion constant (D) for cases where $\tau_{bind} < \tau_{off}$ ($N = 16$ [ATP]= 2 mM and 100 μM, $N = 4$ [ATP]= 4.9 μM) as expected. This supports our expectation that fluid cargoes can indeed accumulate higher number of bound motors than rigid cargoes, but only under conditions that ensure that $\tau_{bind} < \tau_{off}$ i.e. when the number of motors (N) is high or the ATP concentration is low or both.

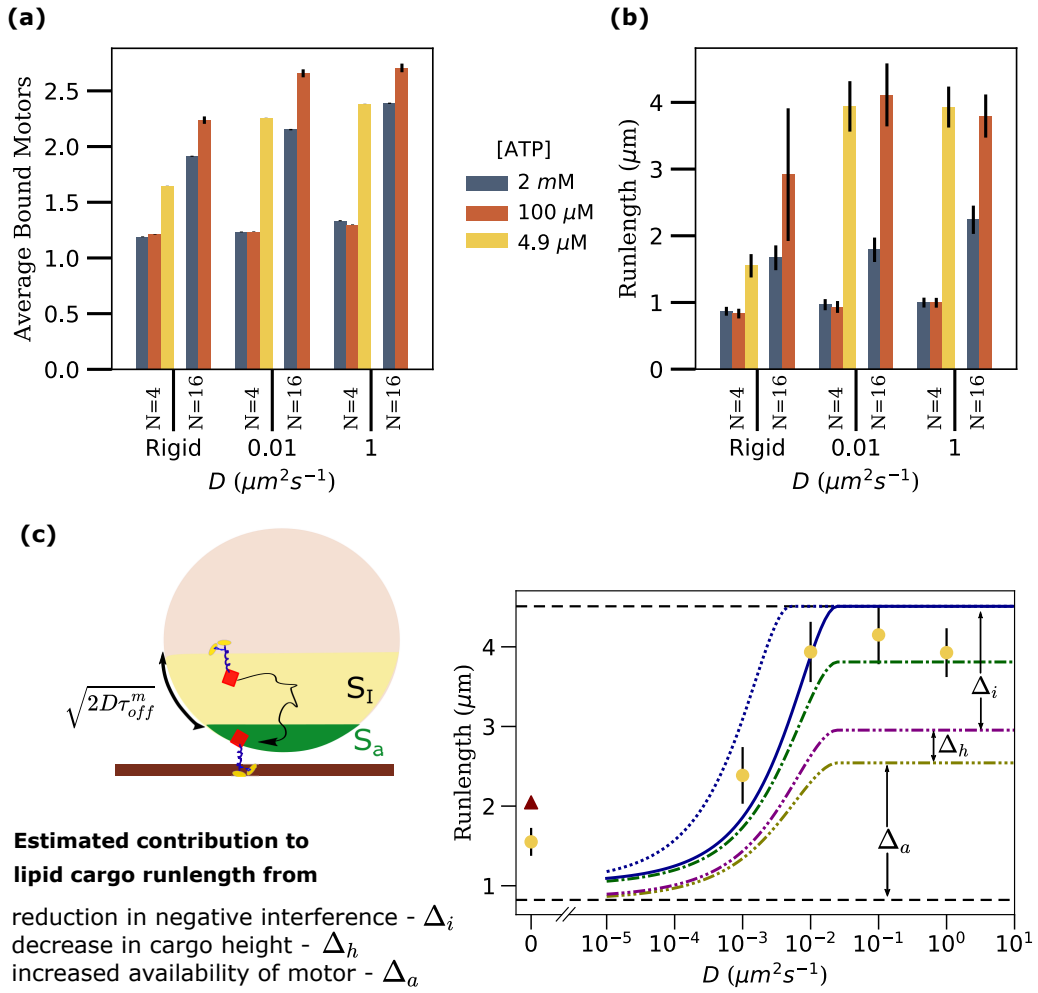

Figure 3.2.3: **Fluid cargo have longer run lengths than rigid cargo.** **(a)** Average number bound motors, **(b)** Runlength as a function of diffusivity (D) for two different numbers of motors on the cargo (N) and three different ATP concentrations. 200 cargo runs were considered for each parameter set. Error bars represent the standard error of the mean (SEM). The average number of bound motors in (a) was calculated as the mean of the number of bound motors (n) in all time samples (with data sampling rate = 100 s^{-1}) of these 200 cargo runs. Rotational diffusion of cargo was not considered in these simulations. Thus the sample size was large and hence the error bars obtained as the standard error of the mean is very small. **(c)** Comparison between run lengths from our simulations ($N = 4$, [ATP] $= 4.9\ \mu M$, yellow circles) and analytical estimates (maroon triangle, solid, dashed and dash-dotted lines) as described in the text. *Left cartoon*: A lipid cargo, with access area (S_a, green) and influx area (S_I, yellow) shown. Influx area is defined as the region within $\sqrt{2D\tau^m_{off}}$ from the access area. Reprinted with permissions from Sarpangala and Gopinathan, *PLos Comput. Biol.*, 2022 [125]. CC-BY-4.0.

3.2.4 Fluid cargo have longer run lengths than rigid cargo

So far we have shown that increasing surface fluidity reduces inter-motor interference and promotes load-sharing leading to reduced off-rates. Fluidity also makes more motors available for binding in a cooperative fashion with increased binding leading to higher on-rates. We would expect that having more motors bind that survive longer should lead to increased run lengths for fluid cargo. The run lengths of cargoes measured as a function of diffusion constants (Fig. 3.2.3(b)) suggest that this is indeed possible given the right ATP concentration and the number of motors on the cargo (see Fig. 3.E.12 for additional diffusion constants). Although the run length is unaffected by fluidity when τ_{bind} is of the order of τ_{off} (low N and medium/high [ATP]), the run length increases with the fluidity of the cargo surface when $\tau_{off} > \tau_{bind}$ (for high N or low [ATP] or both). The effect is much more pronounced when the disparity between the timescales is higher.

We saw earlier that the average number of bound motors shares similar trends (Fig. 3.2.3(a)) as a function of cargo surface fluidity. It is to be noted, however, that cargoes can have the same average number of bound motors but different run lengths. For example, although high fluidity ($D = 1\ \mu m^2 s^{-1}$) cargoes with $N = 4$ at [ATP]= 4.9 μM and $N = 16$ at [ATP]= 2 mM have the same average number of bound motors, the lower ATP case with fewer total motors shows a substantially larger run length (Fig. 3.2.3(a) and Fig. 3.2.3(b)). This is a consequence of the higher tendency of a cargo to survive a 1 motor state at low ATP due to a lower motor detachment rate (more details in Appendix 3.C).

For saturating ATP conditions, we note that the observation that a high number of motors (16 here) achieves a runlength of only about 2 μm is consistent with values predicted in other *in vitro* experiments and models [71]. This is because even though there are 16 motors on the cargo, the average number of motors that can access the microtubule is only about 1.37 ($N_a = 1 + (S_a/S_T)$). Our runlength values are also comparable to simulation results by Bovyn *et. al.* [25] for rigid and lipid cargoes under saturating ATP conditions. Finally, the range of runlength values for different numbers of motors for a cargo of radius 250 nm agrees with

the range of values from experimental studies [94], lending further validity to our model.

While the results in Fig. 3.2.3 are from simulations without considering cargo rotation, we also ran simulations with rotation and compared the runlength and average number of motors between these two cases Fig. 3.E.19. There is no noticeable change in these metrics with and without cargo rotation.

Overall, our results indicate that surface fluidity increases run lengths when the number of motors (N) is high or the ATP concentration is low or both. While previous studies have shown that the runlength of multi-kinesin rigid cargoes increases with decreasing ATP concentration [137], our simulations show explicitly that the increase in runlength with decreasing ATP concentration is significantly larger for lipid cargoes than for rigid cargoes.

3.2.5 Contributions of different effects to overall run length

We now consider the relative contribution to the overall run length of the different effects we showed are at play; the reduction in negative interference, the cooperative increase in on-rates and the increased availability of motors.

Analytical expression for run length

To estimate the magnitude of these contributions, we first consider an analytical expression for the run length [76]

$$r = \frac{v_o}{N_a \pi_{ad}} \left[\left(1 + \frac{\pi_{ad}}{\epsilon_m} \right)^{N_a} - 1 \right] \tag{3.1}$$

where v_o, N_a, π_{ad}, ϵ_m are the motor speed, the available number of motors for transport, the single motor binding rate and the mean motor off-rate respectively. Based on our results, we now generalize the expression by incorporating the dependence of these parameters on the cargo surface diffusivity D and the number of bound motors.

The mean off-rate, ϵ_m, is sensitive to the presence of inter-motor interference and the introduction of fluidity almost completely eliminates interference (Fig. 3.2.0(b-f)). This means we can treat ϵ_m as having two values; a higher one for rigid cargo due to interference and a lower one for fluid cargo (Fig. 3.2.0(f)).

The number of available motors, N_a, is usually taken to be the number of motors in the access area, S_a, for rigid cargo. For $D > 0$, however, additional motors from an influx area S_I (see Fig. 3.2.3(c)) can reach the access area before the cargo unbinds from the microtubule and contribute to transport. Here we estimate S_I as defined by a region within a distance $\sqrt{2D\tau_{off}^m}$ of the access area, representing the distance diffused by a motor over the mean motor lifetime $\tau_{off}^m = 1/\epsilon_m$. We, therefore, take N_a to be the average number of motors in the access and influx areas combined, $N_a = 1 + (N-1)(S_I + S_a)/S_T$. Thus the number of available motors starts from a minimum value $N_a = 1 + (N-1)(S_a/S_T)$ at $D = 0$ and increases monotonically as function of D before saturating at $N_a = N$.

Finally, motors bind with a rate $\pi_{ad} = \pi_0 = 5\,s^{-1}$ when they are within the access area and do not bind otherwise. This means we can take the mean on-rate of the available motors to be $\pi_{ad} = \pi_0 S_a/(S_I + S_a)$. We note that the access area, S_a, depends on cargo geometry and in particular on the height of the cargo above the microtubule. As more motors bind, the height decreases, S_a increases and the effective on-rate increases (Fig. 3.2.1). Finally, we note that the cargo velocity did not change by more than 5% over the range of parameters we tested (Fig. 3.E.14) and so we took v_o to be constant.

Approximate bounds for run length

Using these analytic estimates, we can compute approximate bounds for the relative contributions of the different effects to overall run length. As an example, we do this for the case of low motor density and low ATP ($N = 4$ [ATP]$= 4.9\ \mu$M, Fig. 3.2.3(c), other cases shown in Fig. 3.E.16). We start with the limiting lower bound case where there is no additional availability of motors due to diffusion ($N_a = 1 + (N-1)(S_a/S_T)$), no reduction in interference ($\epsilon_m = 0.12\,s^{-1}$, Fig.

3.E.15) and the cargo height is at its maximum (corresponding to having 1 motor bound (Fig. 3.2.1(a))). This yields the horizontal dashed line at the bottom in Fig. 3.2.3(c). A similar upper bound that assumes all motors are available ($N_a = N$), interference is absent ($\epsilon_m = 0.1\,s^{-1}$, see Fig. 3.E.15) and the cargo height corresponds to that at $n = 2$ (which is close to the average number of bound motors for this configuration), yields the horizontal dashed line at the top. While the bounds bracket the run lengths measured from the simulations, we notice that the lower limit is well below the actual values, especially at higher diffusion constants. It is to be noted that the bounds do not really extrapolate well to $D = 0$ because, for rigid cargo, the average run length is not set by the average number of motors in access area. A better approximation is the weighted average of run lengths for different numbers of motors in the access area weighted by the probability of having that many motors in the access area (maroon triangle in Fig. 3.2.3(c); details in Appendix 3.B).

Comparison of contributions from different effects

We first consider the contribution due to diffusion increasing the availability of motors alone. Allowing N_a to increase with D but with no reduction in interference ($\epsilon_m = 0.12\,s^{-1}$) and the maximum cargo height, corresponding to $n = 1$, yields the lowest dash-dotted curve in Fig. 3.2.3(c). While there is a substantial increase in run length with increasing D, this increase (of order Δ_a at high D) yields an estimate that is still significantly below the measured values at high D. This indicates that the increased availability of motors alone cannot account for the entire increase in run length. We next incorporate the cooperative increase in the accessible area due to more motors binding and the cargo moving closer to the microtubule by setting the cargo height to that corresponding to $n = 2$ bound motors. This yields an increase in the run length (middle dash-dotted curve in Fig. 3.2.3(c)) but the gain, of order Δ_h at high D, is also too small to account for the observed increase. We finally incorporate the effect of reduced interference between the motors due to surface fluidity by taking $\epsilon_m = 0.1\,s^{-1}$. This shifts the run lengths upwards considerably, by Δ_i at high D, and brings the estimates to

within the range of the observed values (solid curve in Fig. 3.2.3(c); the upper dash-dotted curve is for a cargo height corresponding to one bound motor). Intriguingly, the surface fluidity based reduction in negative interference has an effect that is comparable or even stronger (see Fig. 3.E.16 also) than the effect due to the increase in the number of available motors. We note that a reduction in the interference and the resultant reduction in mean off-rate leads to an increase in the mean motor lifetime, τ_m, and hence an increase in the influx area S_I which is set by $\sqrt{2D\tau_{off}^m}$. Thus, reduction in interference contributes to an increased run length not only due to an increased lifetime of each motor but also due to the resultant increase in the number of motors available for transport. While we used the single motor lifetime τ_{off}^m to estimate S_I, this represents a lower bound since new motors may reach the access area over the entire cargo runtime τ^c. Using the saturating value of τ^c (for high D) in place of τ_{off}^m in the expression for S_I therefore gives an upper-bound estimate for the run length (upper dotted curve in Fig. 3.2.3(c)). We note that the top three curves for estimates that include the effects of reduced interference and increased availability of motors reflect the measured values of run length fairly well as a function of increasing surface diffusion constant across different conditions of ATP and motor number (see Fig. 3.E.16).

3.2.6 Motor teams under external load

So far, we have considered the only load on the motor teams to come from viscous drag on the cargo which is very low for the aqueous medium we have been considering and usually dominated by thermal fluctuations. We now consider the behavior of the motor teams under external loads, specifically looking at motor clustering and collective force generation.

Motors dynamically cluster at specific locations on the lipid cargoes

Past studies of force generation by motors coupled to lipid membranes have shown that the motor performance (as measured by the velocity of microtubules) is reduced due to "slippage" of motors on the lipid membrane [55]. Also, studies have shown that rigid-like ordered regions on the membrane are beneficial for

transport of cargo because the motors can anchor on these ordered regions and use this as a rigid substrate to effectively generate forces [75, 119]. Hence, although motors on lipid cargo can interfere less and survive longer, a question arises as to whether the motors can efficiently generate forces against load while hauling cargo.

An important thing to note is that the geometry of the lipid membrane is a spherical surface, or at least a closed, bounded surface, for cargo *in vivo* such as vesicles and organelles. For such cargo, there is a limit to how far the motors can slip. Motors can slip only as long as the tangential force is non-zero. Once the tangential component reduces to zero and all the force is radial, a motor on a lipid cargo should be as efficient in generating force as on any other substrate.

To understand whether motors are likely to be in this radial force regime, we looked at the probability distribution of the location of motors on the cargo surface. To obtain this distribution, we ran simulations of cargo transport (N=16, High [ATP]= 2mM) under different hindering loads on the cargo and recorded (sampling rate of 100 s^{-1}) the anchor positions of MT bound motors relative to the body coordinate axis of the cargo (see schematic in Fig. 3.2.4). Heat maps in Fig. 3.2.4 show the probability distributions of the anchor positions of MT bound motors on the cargo surface. We can clearly see that there is a preferred position for motors on the cargo surface at different hindering loads (Fig. 3.2.4). At zero hindering load, motors experience only the viscous load which is small enough that this distribution is broad and only a diffuse enhancement is visible near the MT (bottom of the cargo) However, as we increase the cargo load, motors increasingly appear at a preferred location on the cargo surface to balance the load. We calculated the location on the cargo where the tangential force reduces to zero and the horizontal component of force balances the hindering load and found that the height (z-coordinate) of this location above the MT increases with increasing hindering load (see Appendix 3.D). The range of locations we obtained from this argument were in reasonable agreement with the values we measured from simulations (see Appendix 3.D for calculation and values) validating the mechanism for preferential localization of motors. While we see motor density enrichment for

both rigid and lipid cargoes with increasing hindering load, we note that the lipid membrane can allow motors to slide to this preferred location while this is not possible in rigid cargo, explaining the higher density enhancement in the lipid case. Motors can therefore dynamically cluster at a preferred location on the lipid cargo which minimizes the tangential component of motor forces and leads to better load-sharing. Our results are conisitent with prior observations of dynein clustering in axonemal endosomes and related modeling [32]. This sort of dynamic clustering can exist in addition to any intrinsic clustering mechanisms that may exist for *in vivo* lipid membranes [75, 119, 25] which can enhance processivity in motor teams.

This dynamic clustering of motors may also lead to the deformation of the vesicle. Collective forces due to kinesin motors have been observed to lead to the extraction of membrane tubes out of vesicles [2, 88]. There is a threshold of point force on membrane below which such a membrane extraction is not possible (see Appendix 2.A). When the hindering load is low, motors are not localized, the force is low and not concentrated and the threshold is not reached, which is the reason we can ignore deformation of vesicles under normal cargo transport conditions (see Appendix 2.A). If the hindering load exceeds the threshold, the clustering of motors may lead to membrane deformation and tube extraction. It should be noted that in our model, motors can come arbitrarily close to each other, while in reality, volume exclusion could broaden the localization region slightly, thereby affecting the threshold for tube extraction.

Motor teams in fluid cargoes generate higher collective forces

We have predicted that lipid cargoes may have a higher number of MT bound motors which exhibit less negative interference, better load sharing and increased processivity. We have also predicted that motors can cluster together on lipid cargo under constant increased hindering load. Do all these factors imply that lipid membrane coupled motors can also generate more collective force?

Collective forces generated by teams on cargo have been measured by optical

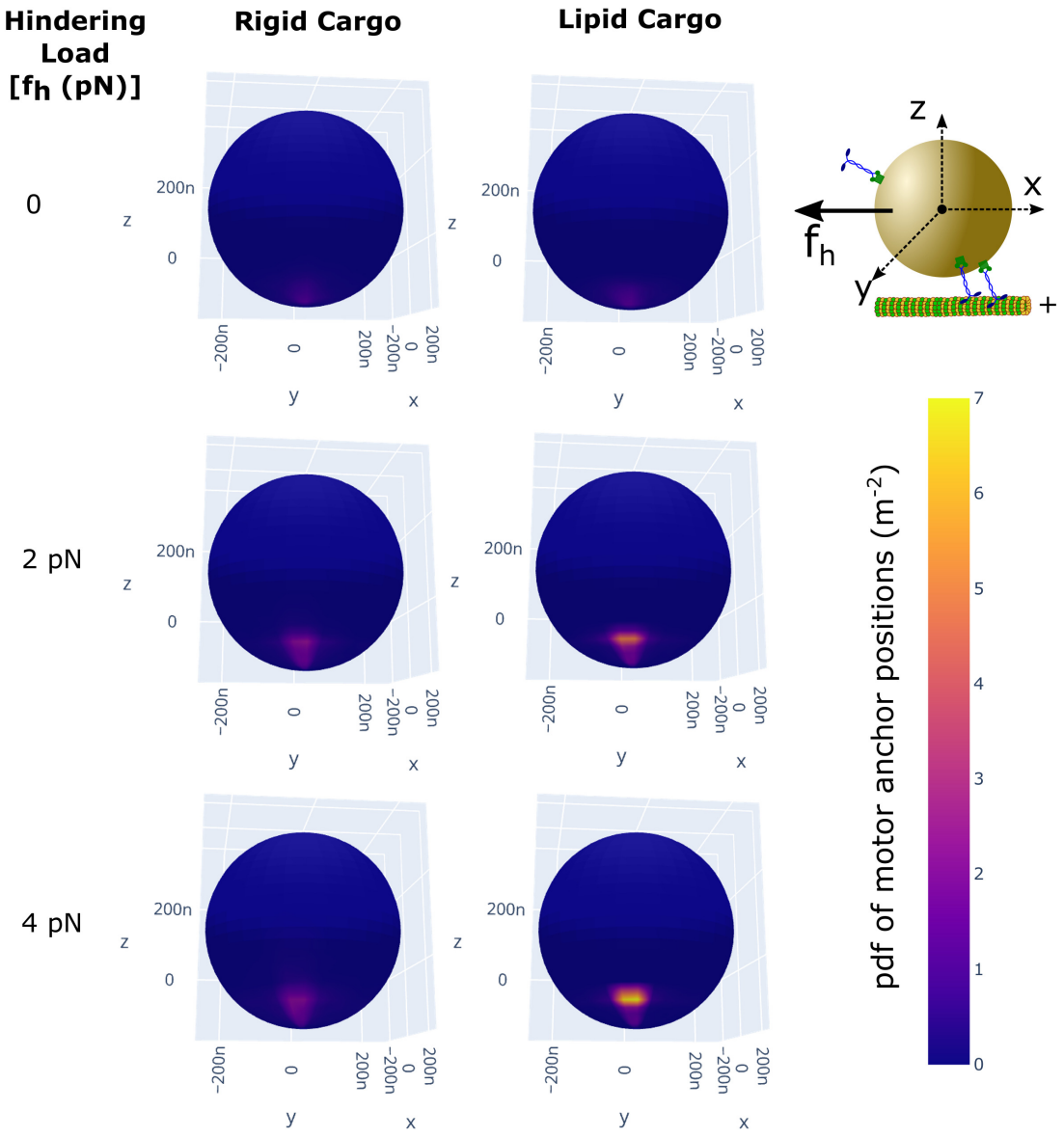

Figure 3.2.4: **Motors dynamically cluster at specific locations on the lipid cargoes.** Average distribution of bound motors on the cargo surface at different hindering loads on the cargo (f_h). Only multiple bound motor cases were considered. Data is from 200 cargo runs with N = 16, high [ATP]= 2 mM with anchor positions of bound motors recorded at a sampling rate of 100 s^{-1}). Anchor positions are measured relative to the body coordinate axis of the cargo (schematic at top-right). Diffusion constant of motors on lipid cargoes was 1 $\mu m^2 s^{-1}$. Reprinted with permissions from Sarpangala and Gopinathan, *PLos Comput. Biol.*, 2022 [125]. CC-BY-4.0.

trap experiments [143] for motor-teams *in vitro* as well as *in vivo*. *In vitro* experiments have indicated that the kinesin-motor teams generate sub-additive forces [47, 69, 141] whereas *in vivo* experiments [90, 141] have shown that motors exert additive forces. While this difference in cooperativity might arise from differences *in vitro* and *in vivo* environments, we wanted to check if it could arise from the difference in the cargo surface properties in *in vitro* (rigid cargoes) and *in vivo* experiments (lipid cargoes).

To this end, we modeled cargo placement in an optical trap of force constant (0.06 pN/nm) [90] (see cartoon in Fig. 3.2.5(a)) and ran simulations of cargo transport starting from a single microtubule bound motor for a maximum of 10 s (or until all motors unbind) for a total of 200 cargoes. We chose the parameters $N = 4$, $[ATP] = 2$ mM, which we believe is accessible to experiments [94]. We measured the values of the average total x-component of force due to motors on the cargo. We then rescaled the collective force [141] by $N \times F_s$ to get the rescaled average force per motor. The rescaled average force tells us how well the individual forces add up and whether or not the motors detach before reaching their stall force, serving as a good measure of the cooperativity between motors.

We scanned through the parameter space of single motor unloaded velocity (v_o) and stall force (F_s) (see Fig. 3.2.5(b)) to get a clear picture of motor cooperativity in different parameter regimes and to allow for comparisons with previous studies [141]. For both rigid and lipid cargoes, we observe that the rescaled average force is higher for lower stall forces and higher velocity in agreement with previous coarse-grained computation for multi-motor teams [141]. However, we find that motors on lipid cargo seem to generate higher rescaled average forces compared to those on rigid cargo virtually over the entire phase space explored (see Fig. 3.2.5(c)). Interestingly, the rescaled average force that we measure in the lipid cargo case is comparable to previous estimates that assumes perfect load sharing [141]. This is again an indicator of improved load sharing properties in lipid cargoes.

Thus the observations of sub-additive forces in *in vitro* experiments [47, 69] and additive forces in *in vivo* [90] experiments could be due to differences in the fluidity of the cargo surface. More controlled experiments on membrane-bound and membrane-free cargoes [94] could verify our prediction.

3.3 Conclusion

Our results show that motors coupled through a rigid cargo experience a broader range of forces when multiple motors are bound, reflecting the geometric constraints on the motor-cargo attachment points leading to antagonistic forces and therefore negative mechanical interference between motors. This interference is consistent with literature findings [40, 122, 69] and counteracts the expected load-sharing with increasing numbers of motors. We predict that the increased fluidity of the lipid membrane which allows the attachment points to move, suppresses strain, decreases the negative interference between kinesins and permits load-sharing between motors to be more effective. The reduction of negative interference not only contributes almost equally to run length at low ATP (and/or high motor numbers) as increased motor availability but is, in fact, the dominant effect at saturating ATP and low motor numbers (see Fig. 3.E.16(a)) which is typically the normal physiological (and *in vitro* experimental) state. Direct measurements of this enhanced load-sharing may be possible using optical trap experiments with an applied load on rigid and fluid cargo. Tuning the load and motor number to a regime where enhanced load-sharing can decrease motor off-rates may be able to resolve the effects in comparisons of rigid versus fluid cargo.

The effects of inter-motor interference in rigid cargo are also expected to be seen in the measurements of speed. However, while our measurements of speeds from the simulations do show a decrease with increasing numbers of bound motors (Fig. 3.E.14), it is not as dramatic as reported in [94]. Consistent with [94], we find this decrease to be negated in the presence of fluidity but the effect is not statistically significant. One possibility is that the force-velocity relation we used (Eq. 2.17 in Chapter 2) is not sensitive enough at low loads. Another more intriguing

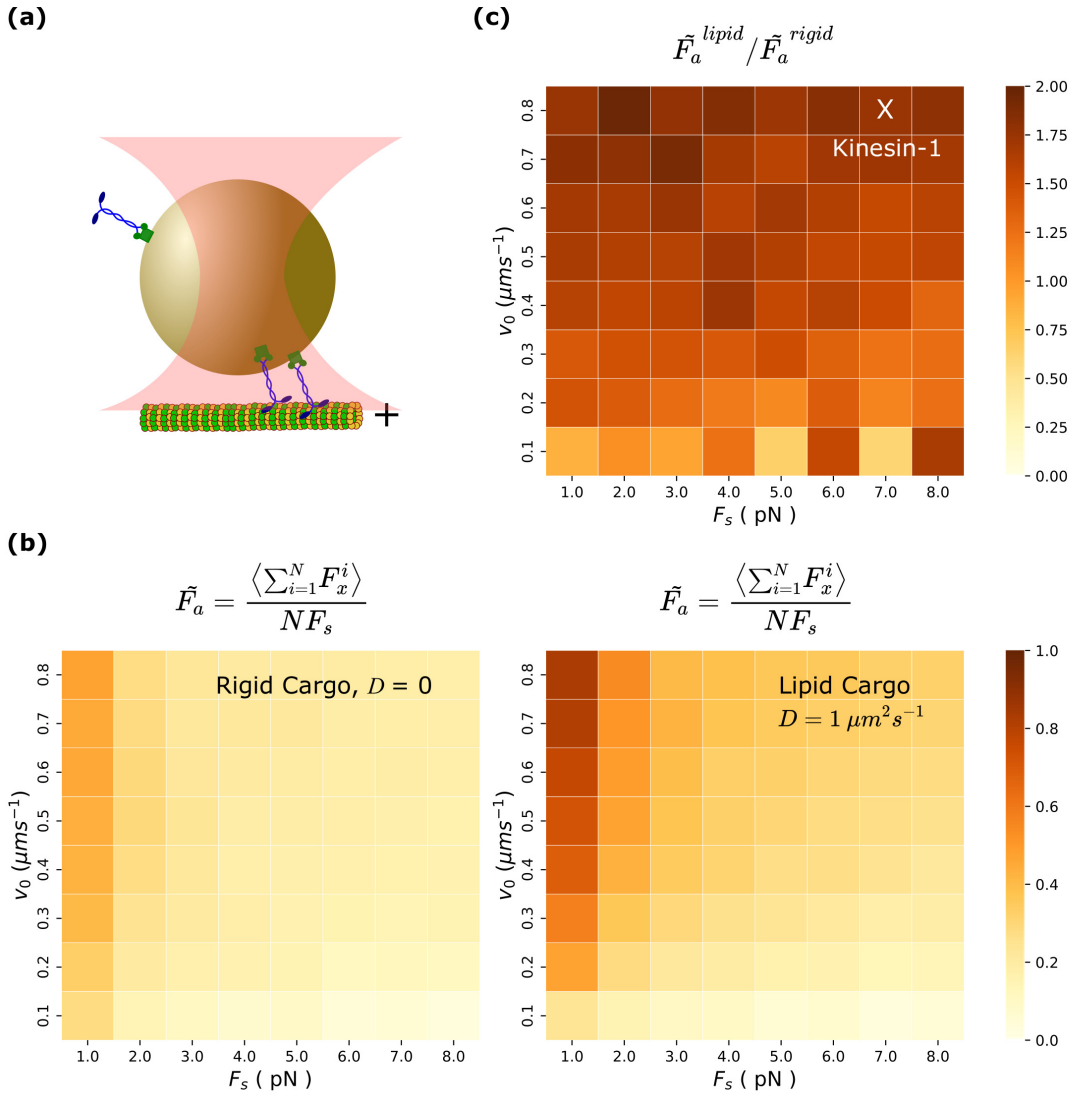

Figure 3.2.5: **Motor teams in fluid cargoes generate higher collective forces.** **(a)** Schematic of the optical trap set up that we used in simulation. **(b)** Rescaled average collective force $\tilde{F_a} = \frac{\langle \sum_{i=1}^{N} F_x^i \rangle}{NF_s}$ as a function of unloaded motor velocity (v_0) and stall force of motor (F_s) in rigid (left) and lipid (right) cargo. (c) Ratio of $\tilde{F_a}$ between lipid and rigid cargo. 200 cargo runs were used for each parameter set. For each cargo run, data of motor forces for each microtubule bound motors were recorded at a sampling rate of 100/s for a maximum time of 10 s for each cargo run. Average collective force is calculated as the average of the total x-component of motor forces over all time samples and cargo runs and then rescaled by NF_s. N=4 and [ATP] = 2 mM. Reprinted with permissions from Sarpangala and Gopinathan, *PLos Comput. Biol.*, 2022 [125]. CC-BY-4.0.

possibility is that the experimentally observed speed-up of lipid cargo [94, 113] may be due to a dispersion of speeds among motors leading to a bias for faster motors in the lead, and slower motors trailing and unbinding more often. On the other hand, microtubule-assay experiments [55] have indicated that the gliding velcoity of microtubules is decreased when motors were anchored on a membrane because the motors "slip" on the membrane. This seems to contradict velocity measurements from both the membrane-bound cargo transport experiments [94, 113] and our simulation. However, this disagreement can be attributed to the difference in the geometry of lipid bilayer between assay set-up [55] and our cargo transport set-up. In a spherical geometry, like our cargo, motors slip only until the tangential component of force goes to zero, while, on a flat membrane, a motor slips every time it makes a step.

Since the reduction in interference manifests as a decrease in the off-rate of motors, it leads to increasing numbers of bound motors at higher membrane diffusion constants. Interestingly, we found that the on-rate was not constant, but increased with an increasing number of bound motors that effectively pulled the cargo surface closer to the microtubule. Monitoring the binding times of successive motors in an optical trap geometry could potentially allow for the experimental verification this effect. This interesting cooperative effect on the on-rate that we uncovered has a smaller effect, in general, on the run length than the reduced interference or increased availability of motors but is still significant ($\approx$10%), especially at low ATP and/or high motor numbers (see Fig. 3.E.16). While the cooperative increase in on-rates works for both rigid and fluid cargo, the effect is enhanced when more motors are available due to fluidity. Finally, we showed that increased fluidity results in an expected increased recruitment of motors to the microtubule, thereby increasing the number of bound motors, with the effect only being significant at very high motor density or low ATP. We found that the confluence of decreased interference, decreased off-rate, increased on-rate and increased motor recruitment can lead to positive feedback resulting in dramatic effects on the run length, under the right conditions. We predict, for example, that run length is

insensitive to cargo surface fluidity for moderate numbers of motors at saturating ATP but can increase by *several fold* for fluid membranes at low ATP conditions. Taken together, our work reconciles varying experimental results including the observed insensitivity of run length to cargo fluidity at moderate motor densities and high ATP concentrations [94, 113]. Our prediction of a significant enhancement of run length at low ATP is potentially physiologically important as an adaptive mechanism, *in vivo*, under stress or starvation conditions [72].

We developed a generalized version of the analytical expression for run length that accounts for cargo surface fluidity and expect it to be useful to explore a wide range of parameter spaces for different motor types and cargo geometries going beyond our simulations, which were mostly done with a fixed cargo radius of 250 nm. Cargo geometry enters into the effective on-rate for motors which scales as $\pi_{ad} = \pi_0 S_a/(S_I + S_a)$. The increase in access area, S_a, as the cargo is pulled closer to the MT is determined by the curvature of the cargo surface and sets the magnitude of the cooperative increase in motor numbers. Even considering a fixed cargo height and high D, the on-rate still depends on the ratio of access area to the total surface area which decreases with increasing radius of curvature of the cargo. Thus, from our generalized version of Eq. 4.1, we expect an increased on-rate and higher run lengths for smaller cargo with a fixed number of motors (see Fig. 3.E.17). This is consistent with our simulation results (Fig. 3.E.20) and with other numerical studies [25]. The smallest cargos, with sizes comparable to synaptic vesicles of about 100 nm [30], in fact, show an enormous increase in the run length over a range of fluidity that is consistent with the ranges for *in vivo* membranes in different contexts [73, 55]. For synaptic vesicles with fluid membranes therefore, transport over very large axonal distances, is a natural outcome of our model. If the surface density of motors is fixed, on the other hand, the quadratic increase in the number of available motors compensates for the reduction in on-rate resulting in larger run lengths for larger cargo (Fig. 3.E.18). In general, the changes in run length over physiological ranges of fluidity imply that surface fluidity could be used as a control parameter to regulate transport.

We also explored the effects of load on motor team performance and showed that

motors on lipid cargo can undergo dynamic clustering and enhanced collective force generation. *In vivo*, increased load may be due to trapping or steric occlusion of the cargo, in which case motors can potentially cluster together exerting increased directed force against the load, perhaps even freeing the cargo. Such an adaptive response involving motor clustering has been observed in axonemal endosomes [32] and increased collective force generation in response to increased load could potentially be important in maintaining transport *in vivo* where crowding is high.

Overall, in this chapter, we identified the fundamental ways in which lipid membranes affect cargo transport by teams of molecular motors and connected with the macroscopic transport properties of physiological relevance.

Notes

3.A Estimation of relevant timescales

3.A.1 τ_{bind} and τ_{off}

τ_{bind} is the mean time taken for any one motor out of N motors of lipid cargo to bind to the microtubule. If a single motor takes τ_{ad} to bind, then if we have N of them, mean time for any one of the motor to bind is

$$\tau_{bind} = \frac{\tau_{ad}}{N} \tag{3.2}$$

$\tau_{ad} = 1/\pi_{ad}$. We have measured the value of π_{ad} in Fig. 3.2.1 for a lipid cargo of radius 250 nm and fluidity $D = 1\,\mu m^2 s^{-1}$. It is about 0.12 s^{-1}. So $\tau_{ad} = 8.33$ s.

τ_{off} is the time taken for a given bound motor to unbind. It is estimated as $\tau_{off} = \epsilon_o^{-1}$, where ϵ_o is the off-rate of an unloaded kinesin motor (bare off-rate). Unloaded motor off-rate is a function of ATP concentration. At high ATP concentration of 2 mM, ϵ_o is measured to be 0.79 s^{-1} [9, 8]. Based on previous studies [152, 154, 130], we assume that $\epsilon_o = v_o/d$. d is the run length of unloaded kinesin motor which is found to be independent of ATP concentration. These information along with Michaelis-Menten equation provided in Eq. 2.16 enable us to calculate unloaded velocity (v_o), unloaded off-rate (ϵ_o) and unbinding time (τ_{off}) of a kinesin-1 motor at different ATP concentrations. Please refer to Table 3.A.1 below for numerical values.

Table 3.A.1: **Comparison of the single motor binding and unbinding times for different N and [ATP]**

N	**[ATP]**	v_0 **(nm s^{-1})**	$\epsilon_o = \frac{v_o}{d}$ **(s^{-1})**	τ_{off} **(s)**	$\tau_{bind} = \frac{\tau_{ad}}{N}$ **(s)**
4	2 mM	800	0.79	1.26	2.08
4	100 μM	555	0.548	1.82	2.08
4	4.9 μM	80	0.079	12.66	2.08
16	2 mM	800	0.79	1.26	0.52
16	100 μM	555	0.548	1.82	0.52

τ_{bind} - the estimated mean time for the first motor binding in a lipid cargo (with $D = 1$ μm^{2}s^{-1}) assuming that all motors on the cargo are unbound , τ_{off} - the mean lifetime of a bound motor, N - total motors on the cargo. d is the run length of unloaded kinesin motor which is found to be independent of ATP concentration.

3.A.2 Conditional on-rate

In Fig. 3.2.1, we showed that the binding rate of a motor increases as the number of bound motors increases. However, it might be challenging to measure this rate directly in experiments because the n-bound state is not stationary but can decay to $n-1$ state by losing a motor. But one might be able to experimentally measure the number of bound motors as a function of time and one can obtain the *conditional on-rate per motor* from this data. We define the conditional on-rate per motor (Fig. 3.E.9) as the rate of transitioning from n-bound state to $n+1$-bound state divided by the total number of unbound motors in that state, $N-n$. A n-bound state can transition to a $n+1$-bound state if any one of the $N-n$ free motors binds to the microtubule. As mentioned earlier n-bound state can also decay to $n-1$-bound state if one of the motors unbind. So we are looking at the rate with which n goes to $n+1$ gated by n going to $n-1$. To obtain this conditional on-rate from the number of bound motors as a function of time, we just have to filter all the n to $n+1$ transitions in this time series, measure mean

rate for such transitions and divide by $N - n$.

In addition to being straightforward to measure from trajectory data, it is also easy to find an analytical estimation of this conditional on-rate of a motor if we know the single motor on-rate and the single motor off-rate. Let τ_o^n be the mean time for the decay of the n-bound state. Assuming that the motors work independently, we can write, $\tau_o^n = \tau_o^1/n$. Let τ_b^n be the mean time for gaining 1 more bound motor. Since there will be $N - n$ free motors when n motors are bound and these motors bind independently, $\tau_b^n = \tau_b^s/(N - n)$ where $\tau_b^s = 1/\pi_{ad}$ is the binding time of a single motor.

Mean time to go from n state to $n+1$ state before n state decays to $n-1$ state is

$$\tau_{cd}^n = \frac{1}{\mathcal{N}} \int_0^\infty t e^{-t/\tau_m} \frac{1}{\tau_b^n} dt \tag{3.3}$$

where

$$\frac{1}{\tau_m} = \frac{1}{\tau_o^n} + \frac{1}{\tau_b^n}$$

$\mathcal{N}$ is the normalization factor given by

$$\mathcal{N} = \int_0^\infty e^{-t/\tau_m} \frac{1}{\tau_b^n} dt \tag{3.4}$$

On simplification

$$\tau_{cd}^n = \tau_m = \frac{\tau_b^n \tau_o^n}{\tau_b^n + \tau_o^n} \tag{3.5}$$

The conditional binding time per motor is $\tau_{cd}^1 = \tau_{cd}^n (N - n)$. Conditional on-rate per motor is $\pi_{cd} = 1/\tau_{cd}^1$.

We note that as n increases, the decay rate of n-bound state also increases. This implies the conditional on-rate per motor should increase as a function of the number of bound motors, just because of the increase in the decay rate (or decrease in the gating time) even if the binding rate of motor π_{ad} doesn't change.

But we have seen in Fig. 3.2.1(b) that π_{ad} is not a constant value but is a function of n. We were curious to know how much difference will the change in π_{ad}

make on the conditional on-rate as a function of n. So we plotted the estimated conditional on-rate taking $\pi_{ad}(n)$ (data from Fig. 3.2.1(b)) and compared with conditional on-rate with π_{ad} a constant (equal to $\pi_{ad}(1)$) along with the measured value from simulations (Fig. 3.E.9). However, there is not much difference between $\pi_{ad}(n)$ and $\pi_{ad}(1)$ case indicating that it might be challenging to observe this in experiments. The conditional on-rate measured from simulations agree well with the analytical estimations confirming the consistency between simulation measurements and analytical calculations.

3.B Analytical estimation of run length for a rigid cargo

Since motors, are not free to move on a rigid cargo we approximate the run length as a weighted average of run lengths for the different number of motors in the access region [93]. The probability of locating exactly l motors in the access region when N motors are present on the cargo is

$$P(l) = \binom{N}{l} \alpha^l (1-\alpha)^{N-l} \tag{3.6}$$

α is the ratio of the access region to the total surface area of the cargo. The run length of the rigid cargo is estimated as

$$r_{rigid} = \sum_{l=1}^{N} \frac{P(l)}{\mathcal{N}} \, r(l, \pi_o) \tag{3.7}$$

where $\mathcal{N} = \sum_{l=1}^{N} P(l)$ and $r(N_a, \pi_{ad})$ is given by [79]

$$r(N_a, \pi_{ad}) = \frac{v_o}{N_a \pi_{ad}} \left[\left(1 + \frac{\pi_{ad}}{\epsilon_m} \right)^{N_a} - 1 \right] \tag{3.8}$$

3.C Discussion on how the runlength of cargo can be different even though the average number of motors is the same

We observe in Fig. 3.2.2(a) that the average number of motors for N = 4 Low ATP (4.9 μM) and N = 16 High ATP (2 mM) are approximately equal for lipid cargoes (D = 1 $\mu m^2 s^{-1}$). However, the runlength for the former case is higher than the latter. This is surprising since intuitively one would expect runlength to be the same when the average number of motors is the same.

We attribute this difference to the higher tendency to accumulate motors in the case of N = 4 Low ATP than N = 16 High ATP. A cargo run stops when the last bound motor unbinds. The likelihood for a new motor to bind before this last motor unbinds determines how far the cargo travels on the MT. Let us look at the ratio of the rate to bind one more motor to the unbinding rate for the case when there is just one motor bound, i.e.,

$$\mathcal{R} = \frac{1 \longrightarrow 2}{1 \longrightarrow 0} \tag{3.9}$$

Calculated value of effective binding rate for a given motor in lipid cargo with D = 1 $\mu m^2 s^{-1}$ is approximately 0.12 s^{-1}. So the rate for the process 1 $\longrightarrow$ 2 is 0.12(N-1) s^{-1}. The approximate unbinding rate, i.e., the rate 1 $\longrightarrow$ 0 is 0.79 s^{-1} for High ATP and 0.079 s^{-1} for Low ATP (The no load off-rate of a single kinesin motor).

(a) For N = 4 Low ATP (4.9 μM)

$$\mathcal{R}_1 = \frac{(4-1) * 0.12}{0.079} = 4.56 \tag{3.10}$$

(b) For N = 16 High ATP (2 mM)

$$\mathcal{R}_2 = \frac{(16-1) * 0.12}{0.79} = 2.28 \tag{3.11}$$

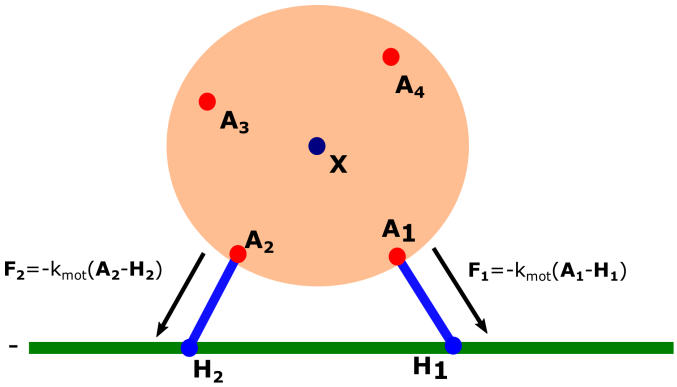

Figure 3.D.1: **Schematic with the motor forces.** $\vec{X}$ is the center of mass of the cargo. $\vec{A}_i$ are the anchor position vectors of motors. $\vec{H}_i$ are the position vectors of the microtubule-bound motor heads. Corresponding motor forces are represented by $\vec{F}_i$.

So the accumulation tendency in case (a) is higher than in case (b). Assume during a cargo run, the bound motor number becomes 1, then case (b) is more likely to fall off compared to case (a). However the average number of bound motors turns out to be the same because of the difference in upper bound, the maximum number of bound motors possible in case (a) is 4 whereas in case (b) it is 16.

3.D Details of different force-related metrics used to characterize negative interference

Force distributions

To get this data, we first run simulations of cargo transport for different cargo surface fludities (N=16, [ATP]= 2 mM). For each cargo run, we recorded data samples at every 0.01 s intervals. Every time sample includes the position of center of mass ($\vec{X}$), the anchor positions of all motors ($\vec{A}_i$), the head positions of microtubule bound motors ($\vec{H}_i$). To get good statistics we ran 200 cargo runs for each cargo surface fluidity.

From the collected data set, we extract all those time samples with desired number of bound motors (say $n = 3$). Then we compute the motor force vectors ($\vec{F}_i$) from the motor anchor and head positions as described in the materials and methods (Also see Fig. 3.D.1). Then we compute the magnitude of the force vectors ($f_i = |\vec{F}_i|$). As per the convention, we take the magnitude to be negative for motors experiencing a hindering load (for example, motor 1 experiences hindering load in the Fig. 3.D.1) and positive for motors experiencing assistive load (motor 2 in Fig. 3.D.1). We randomly select 10000 such f values from all time samples with $n = 3$ and then we compute the force distribution and the error bars by bootstrapping method. Bootstrap sample size was 1000 and number of bootstrap samples was 10.

Mean variance of forces

For each time sample with the given number of bound motors, we computed the variance of the absolute magnitude of motor forces $\sigma^2_{|f|} = \frac{1}{n-1}\sum_{i=1}^{n}(f_i - \bar{f})^2$ where $\bar{f} = \frac{1}{n}\sum_{i=1}^{n} f_i$. We then computed the mean of this variance by using S=10000 random time samples, $\frac{1}{S}\sum_{i=1}^{S}\sigma^2_{|f|}(i)$.

Force correlation

At every time sample with a given number of bound motors (n), we computed the product of x-components, $f_x^j f_x^k$, $(j \neq k)$ between all different unique pairs (i, j) of bound motors. Then we computed the mean by randomly drawing $S = 10000$ values from the set of all $f_x^j f_x^k$ values over all independent motor pairs in all the time samples with given number of bound motors from 200 cargo runs.

Motor off-rate

We measure the motor off-rate by tracking each individual motor from the time binds to the microtubule to the time it detaches from the microtubule. By collecting lifetime of many such individual motor runs within a cargo run, we compute the mean lifetime of motors.

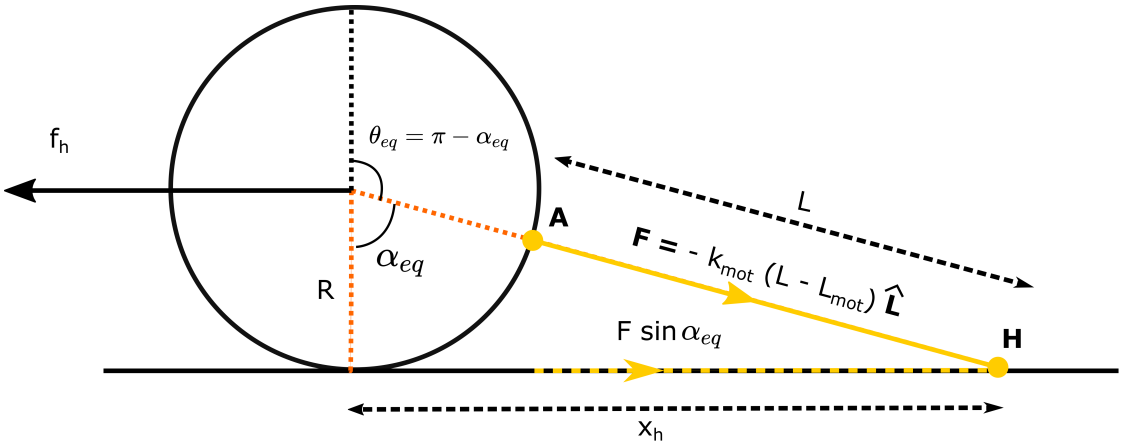

Figure 3.D.2: **Schematic diagram of a cargo with 1 motor under a fixed hindering load.** It is assumed that motor diffuses until the tangential component of force on the cargo surface reduces to 0.

Calculation of equilibrium anchor position for a motor on a lipid cargo

We assume that motor diffuses on the cargo until the tangential component of motor force reduces to zero and at equillibrium, x-component of motor force balances the hindering load. Thus from force balance,we have

$$F \sin \alpha_{eq} = f_h \tag{3.12}$$

$$F = k_{mot}(L - L_{mot}) \tag{3.13}$$

But

$$L = \frac{x_h}{\sin \alpha_{eq}} - R = \frac{R}{\cos \alpha_{eq}} - R \tag{3.14}$$

Hence,

$$F = k_{mot} \left(\frac{R}{\cos \alpha_{eq}} - R - L_{mot} \right) \tag{3.15}$$

Substituting Eq. 3.15 in Eq. 3.12, we get

$$f_h = k_{mot} \sin \alpha_{eq} \left(\frac{R}{\cos \alpha_{eq}} - R - L_{mot} \right) \tag{3.16}$$

We then solved for cosα_{eq} numerically. We found solutions range from $\cos \alpha_{eq} =$ 0.81 to 0.72 as hindering force varies from 0 to 8 pN. This is comparable to the

value $cos\,\alpha$ for locations of motor accumulation we get from simulations (0.98, 0.83, 0.83 for $f_h = 0$, 2, 4 pN respectively). The predicted values from the force equilibrium are at slightly larger angles than the measured simulation values presumably because fluctuations will tend to push the cargo slightly away from the MT.

3.E Supplementary Figures

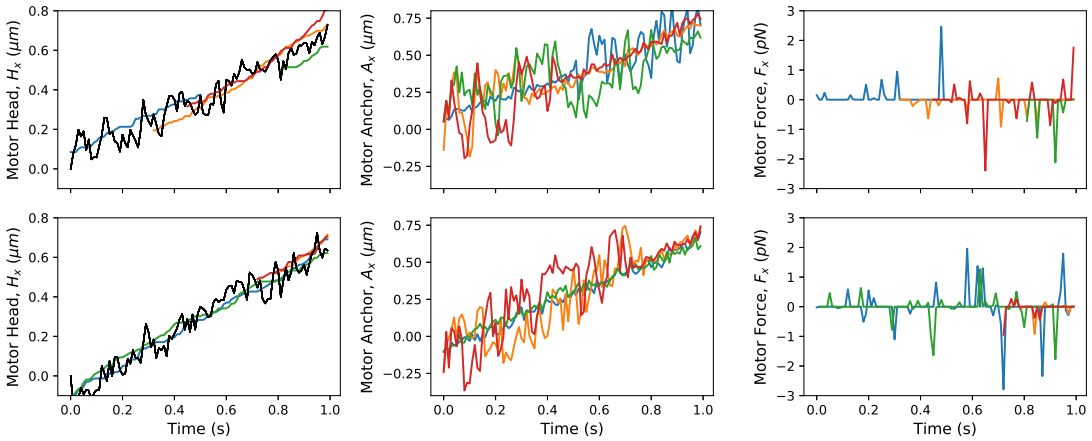

Figure 3.E.1: **Motor and cargo position and corresponding forces.** Variables and the simulation parameters same as Fig. 3.2.0(a) Reprinted with permissions from Sarpangala and Gopinathan, *PLos Comput. Biol.*, 2022 [125]. CC-BY-4.0.

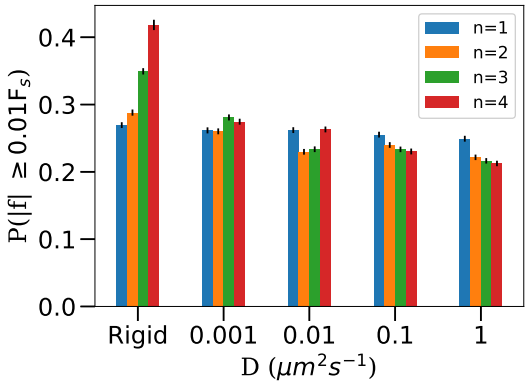

Figure 3.E.2: **The fraction of the force distribution with a magnitude of force f greater than or equal to $0.01F_s$, as a function of the diffusion constant for the different number of bound motors n.** Error bars represent the standard error of the mean obtained by the bootstrap method. F_s is the stall force of kinesin. The fraction increases as a function of n for rigid cargo but decreases for lipid cargo. Required force distributions as a function of n and D were obtained using the same procedure as explained in Fig. 3.2.0(b) (simulations without rotational diffusion, N=16, [ATP] = 2 mM).Reprinted with permissions from Sarpangala and Gopinathan, *PLos Comput. Biol.*, 2022 [125]. CC-BY-4.0.

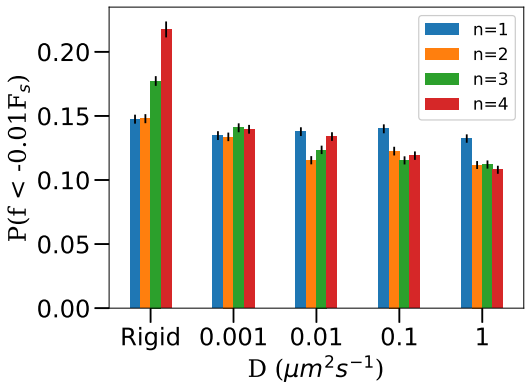

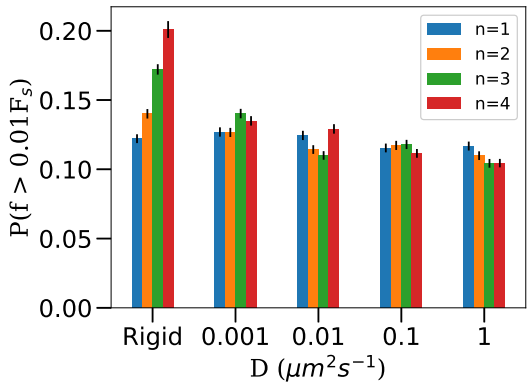

Figure 3.E.3: **Fraction of force distribution with force magnitude greater than $0.01F_s$ in the assistive direction.** Required force distributions as a function of n and D were obtained using the same procedure as explained in Fig. 3.2.0(b) (simulations without rotational diffusion, N=16, [ATP] = 2 mM). Reprinted with permissions from Sarpangala and Gopinathan, *PLos Comput. Biol.*, 2022 [125]. CC-BY-4.0.

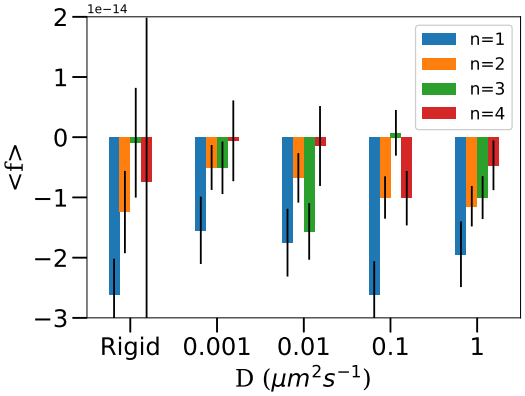

Figure 3.E.4: **Mean value motor force (in Newtons) experienced by a bound motor as a function of the number of bound motors n and diffusion constant D.** Mean force magnitude is negative which means on an average the motor is in the hindering direction, as one would expect because of active motion of motor on MT. The magnitude of mean force decreases with an increase in the number of bound motors due to load sharing. (simulations without rotational diffusion, N=16, [ATP] = 2mM) Reprinted with permissions from Sarpangala and Gopinathan, *PLos Comput. Biol.*, 2022 [125]. CC-BY-4.0.

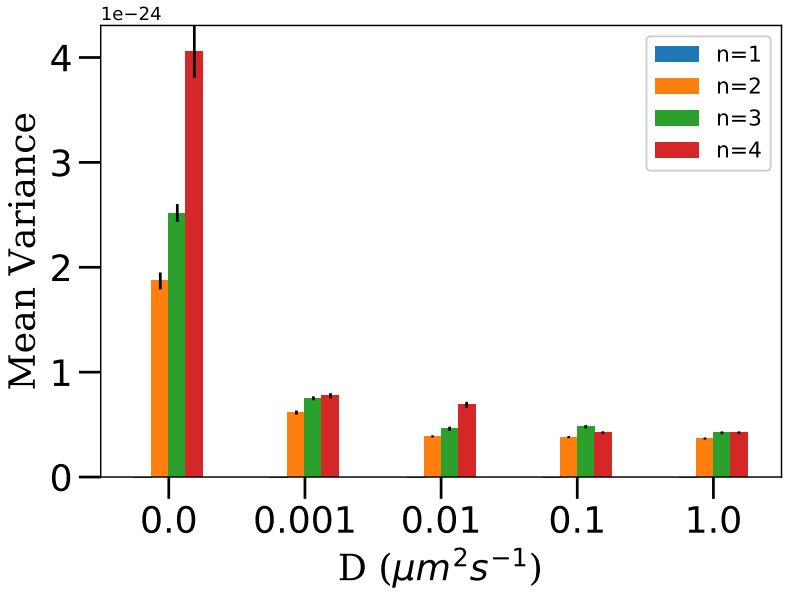

Figure 3.E.5: **The mean variance of forces (in units of N^2) among bound motors.** Calculated as $\frac{1}{S}\sum_{i=1}^{S}\sigma^2_{|f|}(i)$ where the summation is over all the sample time points where the number of bound motors is n. $\sigma^2_{|f|}(i)$ is the variance in the magnitude of force experienced by the n bound motors at i^{th} data sample. $S = 10000$ except for (i) $D = 0$ $n = 3$, $S = 7360$ (ii) $D = 0$ $n = 4$, $S = 1083$ (iii) $D = 0.001$ $n = 4$, $S = 3754$ (iv) $D = 0.01$ $n = 4$, $S = 6396$ (v) $D = 0.01$ $n = 4$, $S = 3508$ (vi) $D = 0.1$ $n = 4$, $S = 4883$. (simulations without rotational diffusion, N = 16 [ATP] = 2 mM). Reprinted with permissions from Sarpangala and Gopinathan, *PLos Comput. Biol.*, 2022 [125]. CC-BY-4.0.

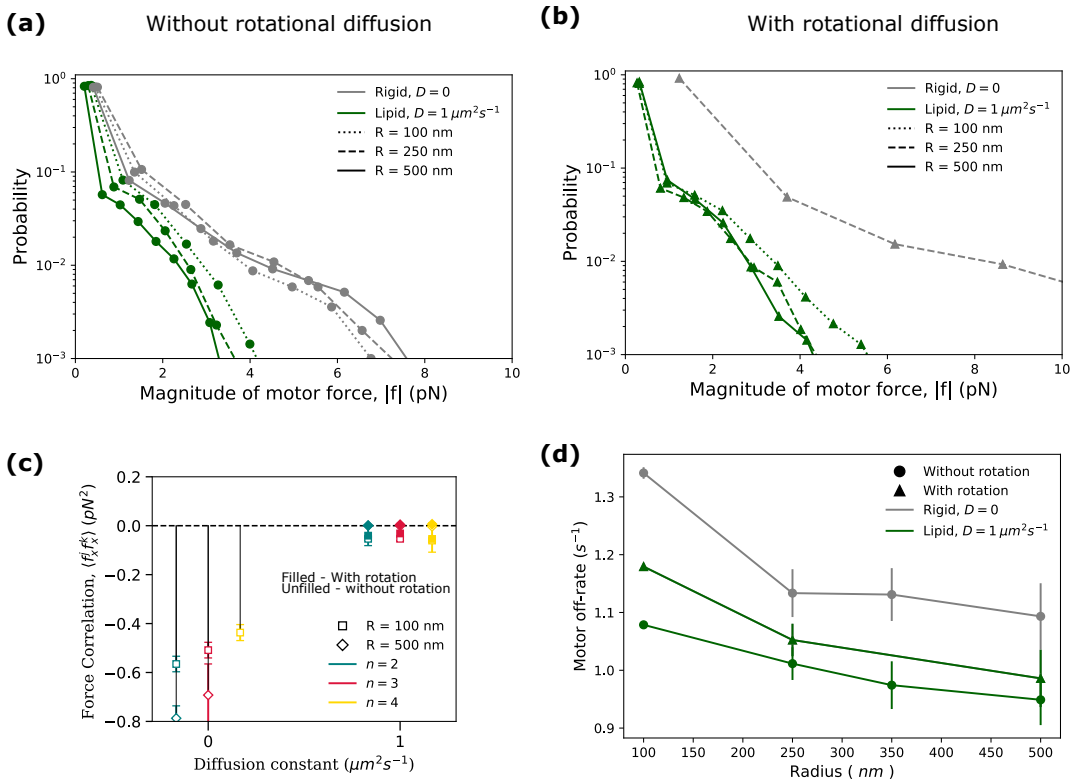

Figure 3.E.6: **Simulation results for different cargo radii**. (a) Distribution of the absolute magnitude of motor forces in rigid and lipid cargoes for two different cargo radii, without considering rotational diffusion of cargo. (b) Distribution of the absolute magnitude of motor forces in rigid and lipid cargoes for two different cargo radii, including rotational diffusion of cargo. (c) Mean force correlation between x-components of motor forces (d) Mean single motor off-rate. N=16, [ATP]= 2 mM. Reprinted with permissions from Sarpangala and Gopinathan, *PLos Comput. Biol.*, 2022 [125]. CC-BY-4.0.

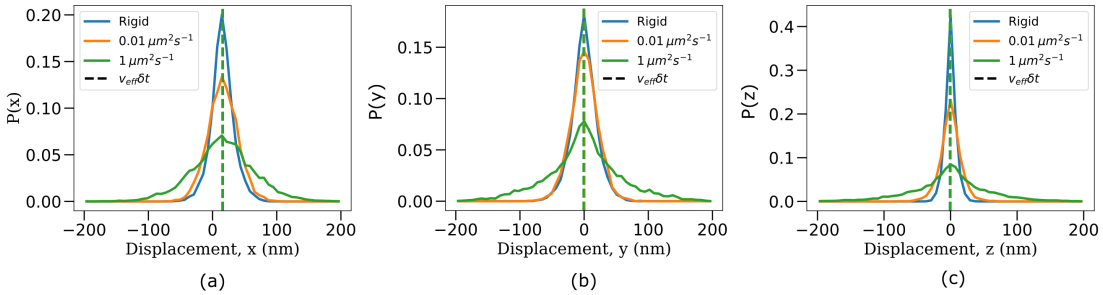

Figure 3.E.7: **Distribution of cargo displacements (position fluctuations) measured in 0.01 s time intervals along (a) x-axis (b) y-axis and the (c) z-axis.** In general, fluctuations increase with the increase in the fluidity of the cargo surface. Vertical lines indicate the mean values of fluctuations, interpreted as $v_{eff}\delta t$ where v_{eff} is the effective velocity of cargo and δt is the time interval used for measuring fluctuations (0.01 s). Fluctuations along the x-axis have a positive mean ($v_{eff}\delta t \approx 8\,nm$) because of the active motion due to molecular motors. Fluctuations along the y-axis and z-axis have a 0 mean. Fluctuations along the z-axis are much narrower than fluctuations along the y-axis and x-axis because of the steric force due to the microtubule. Data were obtained from the transport of cargoes (without rotational diffusion) with a total of $N = 16$ motors at [ATP] = 2 mM. 200 cargo runs were considered for each diffusion constant. Reprinted with permissions from Sarpangala and Gopinathan, *PLos Comput. Biol.*, 2022 [125]. CC-BY-4.0.

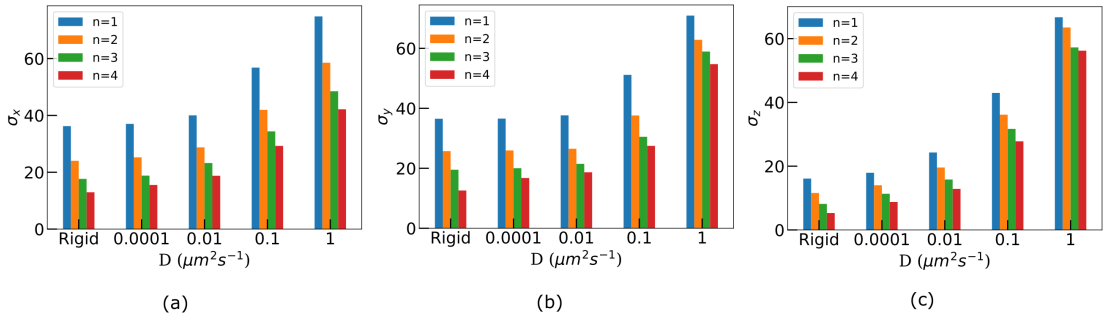

Figure 3.E.8: **Standard deviation (nm) of the position fluctuations as a function of diffusivity and the number of bound motors.** Data were obtained from the simulation of the transport of cargoes (without rotational diffusion) with a total of $N = 16$ motors at [ATP] = 2 mM. 200 cargo runs were considered for each diffusion constant. Reprinted with permissions from Sarpangala and Gopinathan, *PLos Comput. Biol.*, 2022 [125]. CC-BY-4.0.

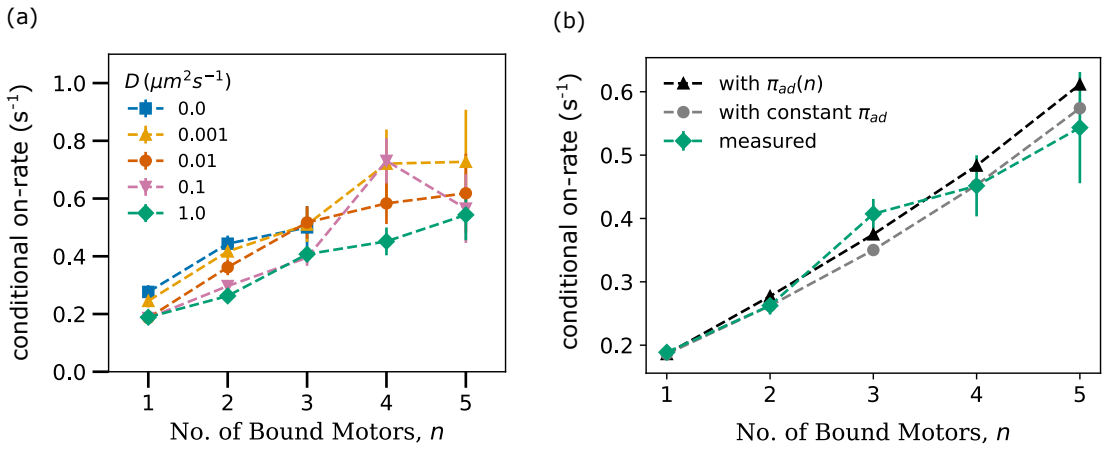

Figure 3.E.9: **(a) Conditional on-rate measured from the simulation trajectories.** We simulated 200 cargo runs (without rotational diffusion) for N = 16 [ATP] = 2 mM case and recorded the value of the number of bound motors at a sampling rate of 100 s^{-1}. With this data, we identified all the n bound motors to $n+1$ bound motor transitions, calculated the mean time for such transitions, and then the mean rate (1/meantime). We then divided this rate by the number of unbound motors $N-n$ to obtain the conditional on-rate per motor. We then repeated the analysis process for a different number of bound motors n and diffusion constants D. **(b) Comparing the measured conditional on-rate with analytical expressions.** Black triangles with dashed lines provide conditional on-rate where we consider the increase in on-rate of a single motor with an increase in the number of bound motors. Grey circles with a dashed line provide conditional on rate assuming a constant single motor on-rate. It can be inferred that if we measure this quantity in experiments one can expect to see only a slight increase as the cargo comes closer to the microtubule. This is because as the number of bound motors increases, the effective detachment rate of the n-bound state increases, hence the gating time decreases. Our analysis shows that the decrease in gating time contributes more to the increase in the conditional on-rate than the increase in the single motor on-rate. See Appendix 3.A for more details. Reprinted with permissions from Sarpangala and Gopinathan, *PLos Comput. Biol.*, 2022 [125]. CC-BY-4.0.

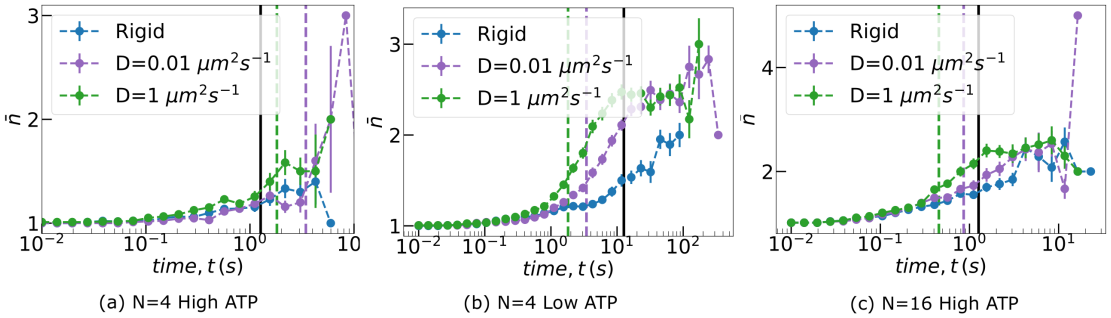

Figure 3.E.10: **Ensemble average (± SEM) of the number of bound motors for three different cargo-motor systems.** Vertical lines indicate the estimated time-scales, mean time for a new motor to bind - τ_{bind} (dashed lines) and mean unbinding time of a kinesin motor - τ_{off} (solid black line). N is the total number of motors on cargo, High [ATP] = 2 mM, Low [ATP] = 4.9 μM. The averaging was performed over 200 cargo runs (without rotational diffusion) each. Please refer to Table 1 in Appendix 3.A for more information on τ_{bind} and τ_{off}. Reprinted with permissions from Sarpangala and Gopinathan, *PLos Comput. Biol.*, 2022 [125]. CC-BY-4.0.

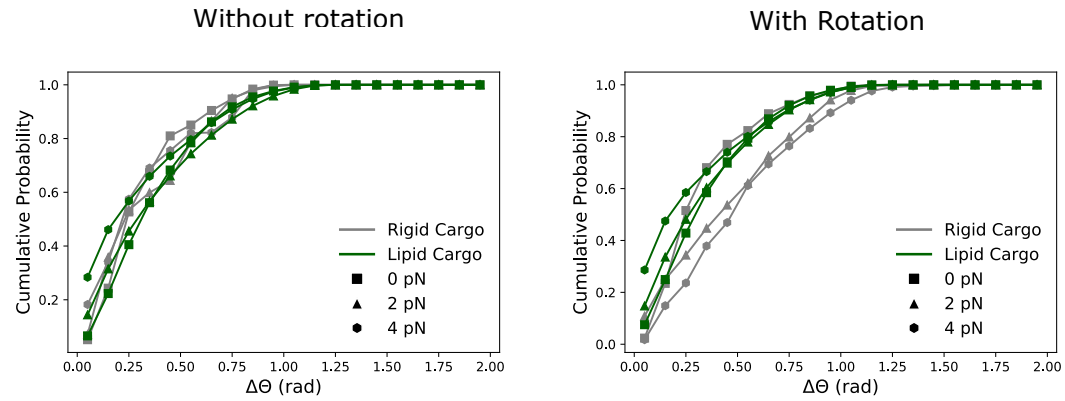

Figure 3.E.11: **The distribution of the angular distance (ΔΘ) between the anchor positions of microtubule bound motors along the great circles connecting them (ΔΘ).** 200 cargo runs were considered for each parameter set with data sampling rate = 100 s^{-1}). Reprinted with permissions from Sarpangala and Gopinathan, *PLos Comput. Biol.*, 2022 [125]. CC-BY-4.0.

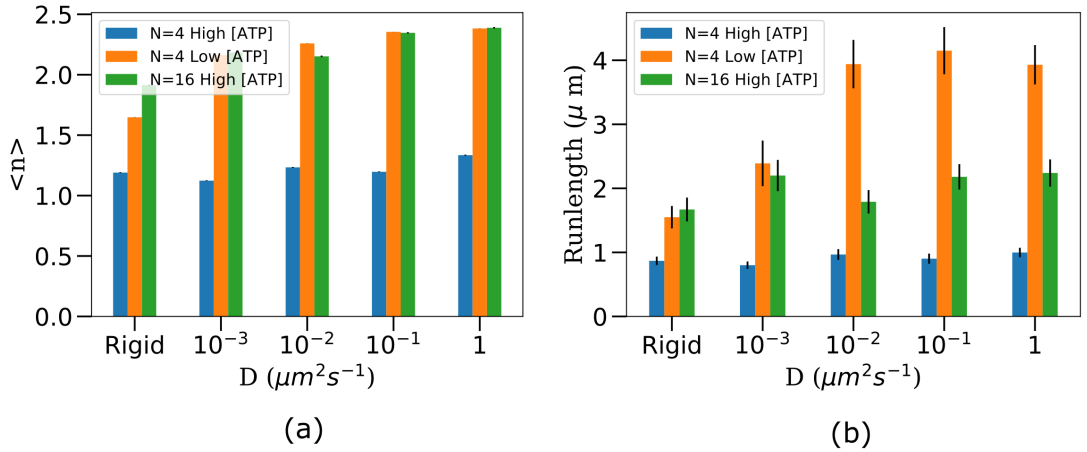

Figure 3.E.12: **(a) Average number of motors (± SEM) (b) Runlength (± SEM) for more values of diffusion constants.** Averaging was performed over 200 cargo runs in each case. Reprinted with permissions from Sarpangala and Gopinathan, *PLos Comput. Biol.*, 2022 [125]. CC-BY-4.0.

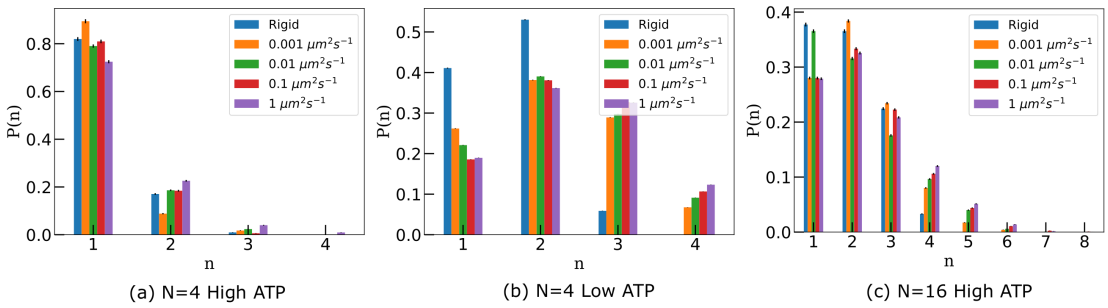

Figure 3.E.13: **Probability distribution of the number of bound motors in three different cargo-motor systems. High [ATP] = 2 mM, Low [ATP] = 4.9 μM.** Data were obtained from 200 cargo runs for each case. Reprinted with permissions from Sarpangala and Gopinathan, *PLos Comput. Biol.*, 2022 [125]. CC-BY-4.0.

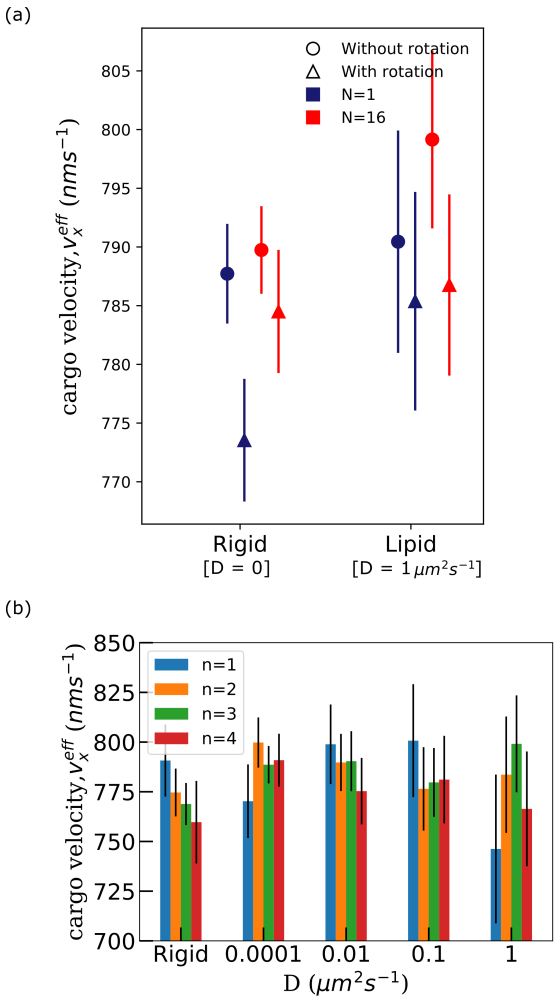

Figure 3.E.14: **Velocity of cargo along x-axis, v_x^{eff} as a function of the number of bound motors and diffusion constant.** Velocity is measured as the ratio of mean displacement along x-axis in a given time window (we took $\delta t = 0.1s$) to δt. Cargo position data was obtained from the simulations of the transport of cargoes with a total of $N = 16$ motors at [ATP] = 2 mM. 200 cargo runs were considered each for each diffusion constant. We recoreded data at a sampling rate of 100 s^{-1}. Data in (b) is for N= 16, [ATP] = 2 mM without rotational diffusion. Error bars represent the standard error of the mean. For figure (a) we considered 10000 random time windows over 200 cargo runs to get the mean displacement for each diffusion constant. For figure (b) we considered all the time window samples with given n over all the cargo runs. Reprinted with permissions from Sarpangala and Gopinathan, *PLos Comput. Biol.*, 2022 [125]. CC-BY-4.0.

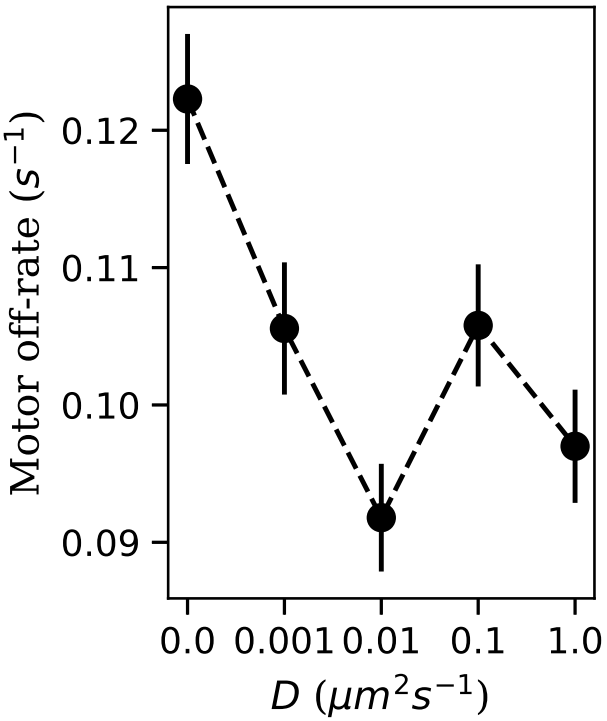

Figure 3.E.15: **Average value of motor off-rate as a function of fluidity of cargo surface for N = 4 [ATP] = 4.9 μM.** (Sample size = 530 from 200 cargo runs) Reprinted with permissions from Sarpangala and Gopinathan, *PLos Comput. Biol.*, 2022 [125]. CC-BY-4.0.

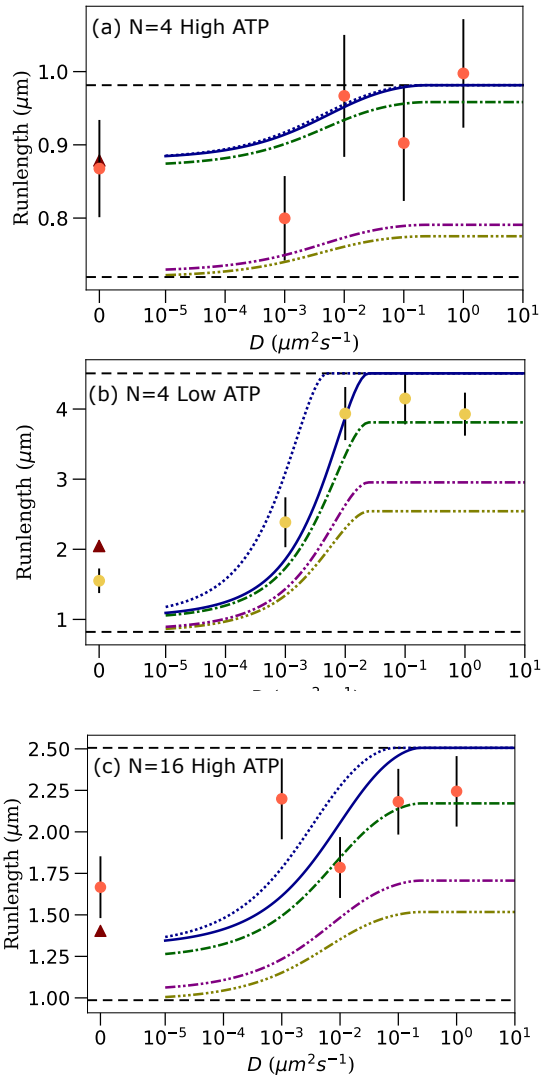

Figure 3.E.16: **Comparison between run lengths from our simulations (circles) and analytical estimates (maroon triangle, solid, dashed and dash-dotted lines) as described in the main text.** Reprinted with permissions from Sarpangala and Gopinathan, *PLos Comput. Biol.*, 2022 [125]. CC-BY-4.0.

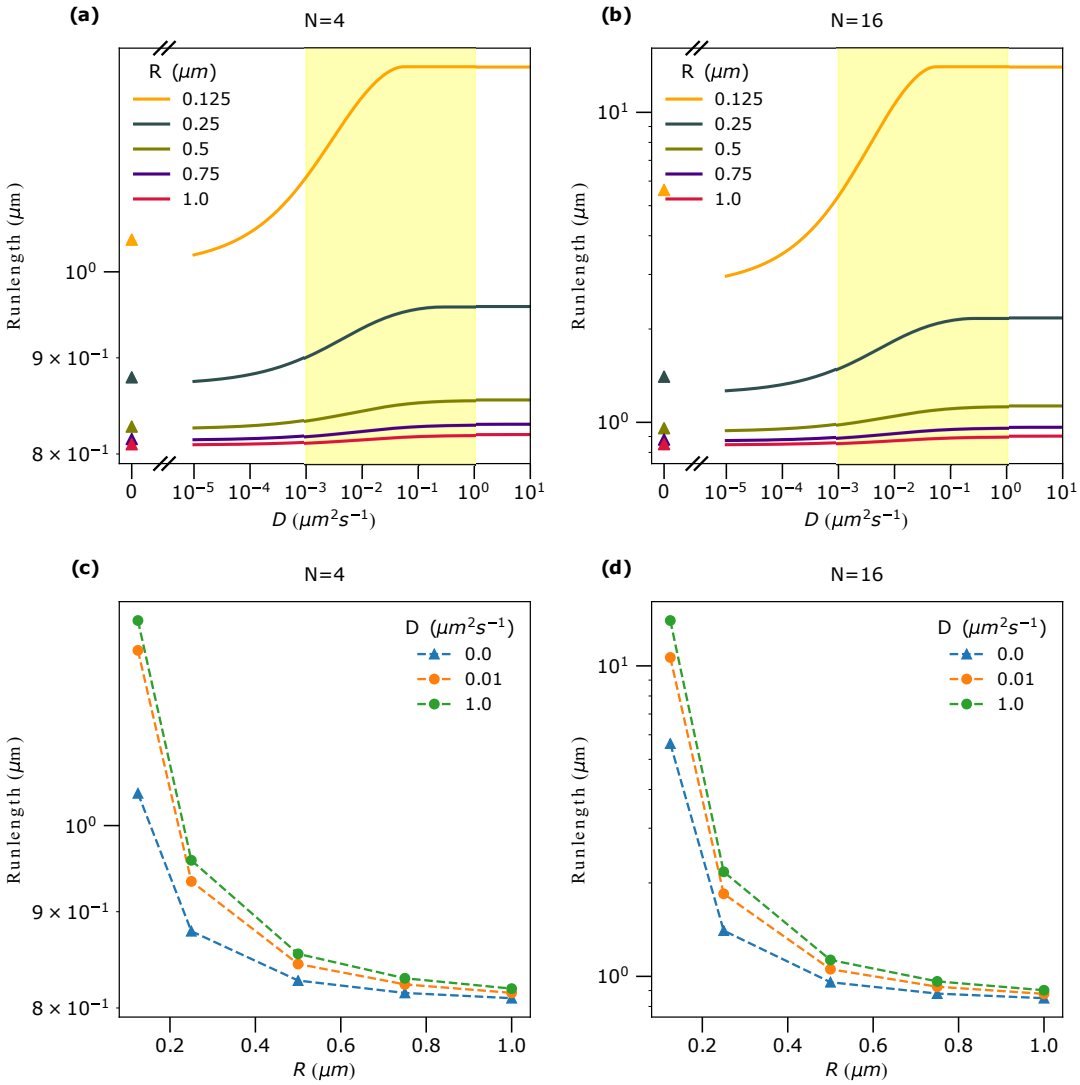

Figure 3.E.17: **Analytically estimated runlengths for different cargo radii for a fixed number of motors on cargo.** The general method for calculating runlength analytically is described in the main text. We have numerically computed the access area, S_a, considering the typical distance between cargo surface and MT for 1 motor bound case. τ^m_{off} for computing influx area, $S_I(D) = \sqrt{2D\tau^m_{off}}$, was taken to be 1 s which is the typical motor unbinding time at saturating ATP concentration. Yellow vertical bands in (a) and (b) correspond to the range of physiologically relevant diffusion constants of motors. Reprinted with permissions from Sarpangala and Gopinathan, *PLos Comput. Biol.*, 2022 [125]. CC-BY-4.0.

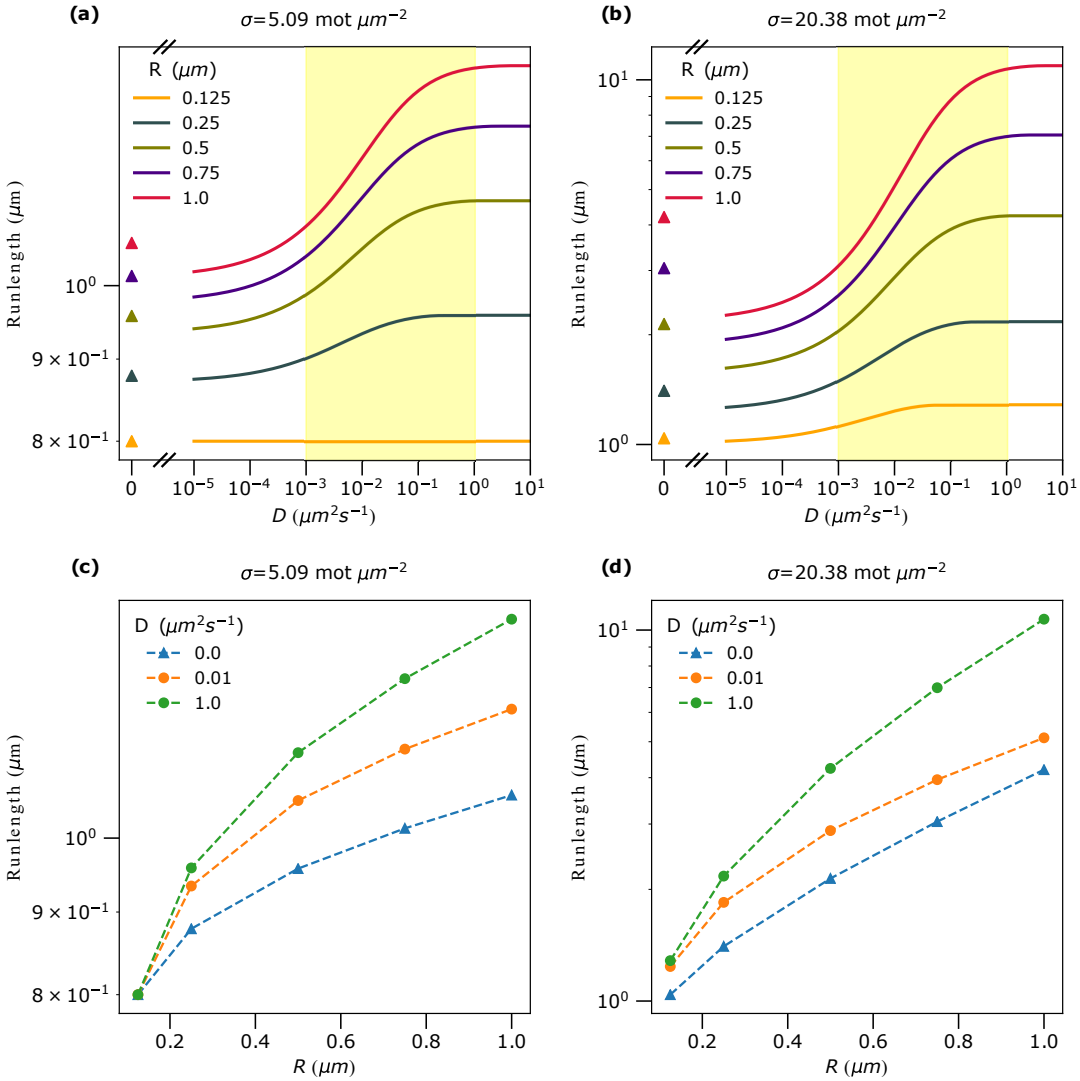

Figure 3.E.18: **Analytically estimated runlengths as a function of cargo radius (R) for a fixed surface motor density (σ).** The general method for calculating runlength analytically is described in the main text. We have numerically computed access area, S_a, considering the typical distance between cargo surface and MT for 1 motor bound case. τ^m_{off} for computing influx area, $S_I(D) = \sqrt{2D\tau^m_{off}}$, was taken to be 1 s which is the typical motor unbinding time at saturating ATP concentration. Yellow vertical bands in (a) and (b) correspond to the range of physiologically relevant diffusion constants of motors. Reprinted with permissions from Sarpangala and Gopinathan, *PLos Comput. Biol.*, 2022 [125]. CC-BY-4.0.

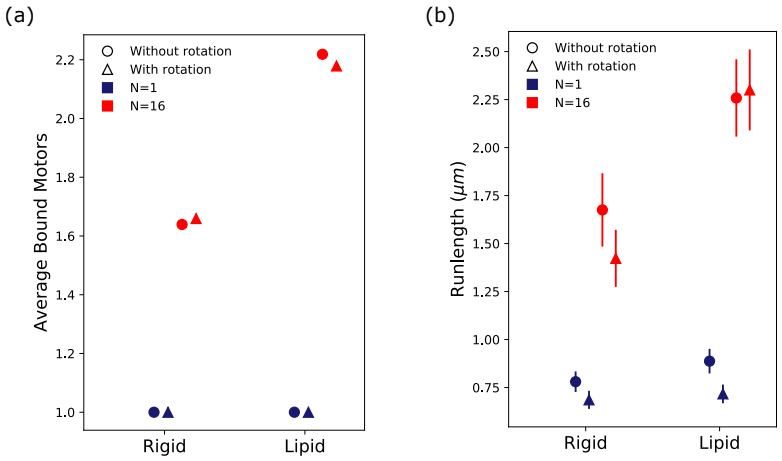

Figure 3.E.19: **Comparison of the number of bound motors and cargo runlength without and with rotational diffusion in the model**. (a) Average number of bound motors (b) Runlength. Error bars represent the standard error of the mean. [ATP] = 2 mM. Reprinted with permissions from Sarpangala and Gopinathan, *PLos Comput. Biol.*, 2022 [125]. CC-BY-4.0.

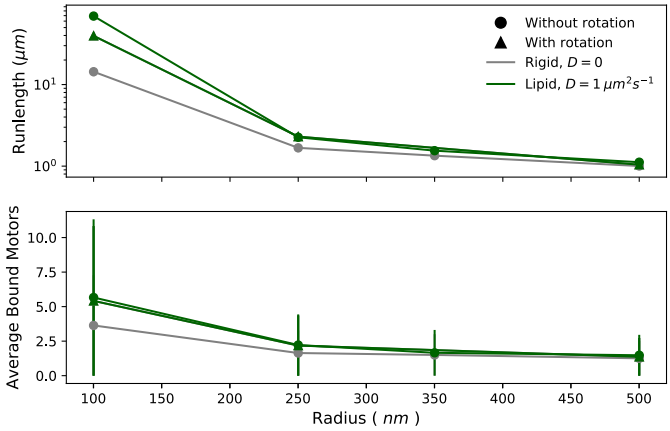

Figure 3.E.20: **Simulation results for different cargo radii**. Runlength, and average number of bound motors in rigid and lipid cargoes as a function of the cargo radius. N=16, [ATP]= 2 mM. Reprinted with permissions from Sarpangala and Gopinathan, *PLos Comput. Biol.*, 2022 [125]. CC-BY-4.0.

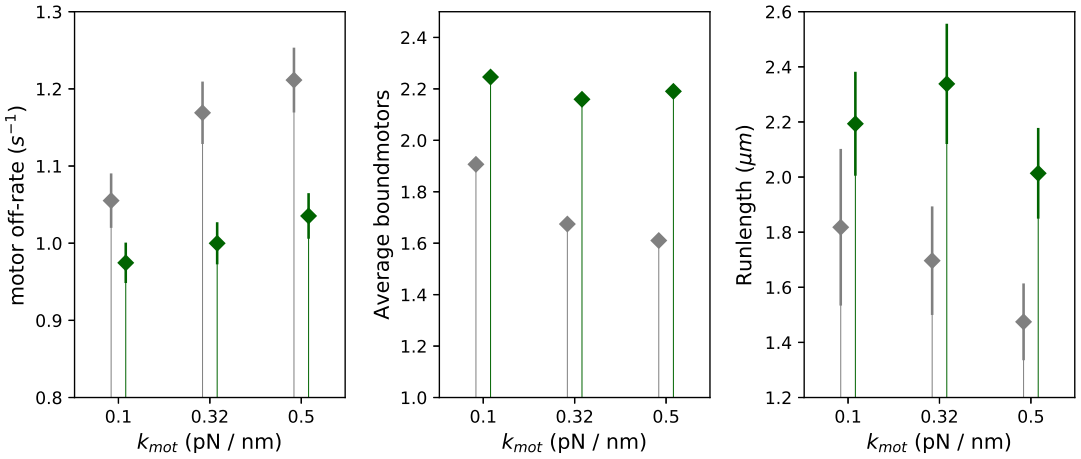

Figure 3.E.21: **Simulation results for different motor stiffness (k_{mot})**. Run-length, average number of motors and motor off-rate for different motor stiffness. N=16 [ATP]= 2 mM. Darkgreen is lipid cargo ($D = 1\mu m^2 s^{-1}$) and grey is rigid cargo ($D = 0$). Reprinted with permissions from Sarpangala and Gopinathan, *PLos Comput. Biol.*, 2022 [125]. CC-BY-4.0.

Chapter 4

Heterogenous teams of motors on the cargo

In this chapter, we explain how heterogeneity among motor populations is essential in explaining the reported increase in cargo velocity with an increase in cargo surface fluidity. Additionally, we show that lipid cargoes can travel a given distance with a lower degree of heterogeneity than rigid cargoes. This work sheds light on novel transport phenomena that emerge because of the combined action of the fluidity of cargo surface and heterogeneity among motor teams.

4.1 Introduction

In the previous Chapter 3 we explained that coupling motors through lipid membrane, and the resulting diffusion of motors on the cargo surface influence multimotor functioning in various ways. This is also in agreement with other papers on membrane-bound cargo transport and gliding assay-based studies [119, 71, 98, 125, 106, 113, 94, 25]. In particular, studies have shown that cargo velocity [113, 94], runlength and mean binding rate [71, 98, 125] can change because of the presence of the membrane as the membrane diffusion helps in reducing mechanical interference [125] and leads to dynamic motor clustering. Microstructures in the membrane (lipid rafts) can lead to additional clustering of motors [119]

In addition to the complexities of motor-motor coupling through the membrane, the motor teams in cells are found to consist of motors of different types. For example, it is known that melanosomes in *Xenopus* melanophores are carried by kinesins, dyneins, and also myosin-V [91], intraflagellar transport of IFT particles by kinesin-II and osm-3 kinesin [134, 115, 116]. There are also abundant examples of the presence of both dyneins and kinesins on the same cargo, which leads to bidirectional transport on microtubules [59]. It is still unclear how cells can achieve desired transport when the individual motors have different transport properties, such as velocity, binding and unbinding rate, and even polarity.

This transport by non-identical motor teams has been studied experimentally and also theoretically. It is shown in microtubule gliding assay experiments and models that the predicted behavior of teams of motors is sensitive to their single motor properties [10]. However, the insights from the planar geometry in assay systems [10] cannot be directly translated into the spherical cargo geometry relevant for cargo transport in cells. Hence, one has to complement these studies with analysis of spherical cargo geometries for a comprehensive understanding of transport by heterogeneous teams of motors through complex cellular environments.

Experiments with a spherical cargo geometry often focus on two quantities, the cargo runlength (average distance traveled) and cargo velocity, since they are two transport quantities of most relevance *in vivo*. If we consider the transport of signaling molecules, then cargo velocity might be more important as it determines how fast cells can respond to external stimuli [110]. It was observed that cargoes that have a fluid surface have higher velocity than those that have rigid or gel-like surfaces when carried by teams of kinesins [94] as well as myosin-V [113] in *in vitro* experiments. These studies also propose two possible mechanisms that could lead to this speedup, namely the delay in strain generation between motors of different types and the enhanced detachment of lagging motors and recentering of cargo. But it is unclear whether these mechanisms explain the observed speedup quantitatively and what is the relative contribution of these two mechanisms to

the overall cargo speedup. We wanted to find a minimal computational model that shows this velocity difference and thereby understand the mechanisms behind higher lipid cargo velocity.

Our simulations of lipid cargo transport in Chapter 3 didn't show a statistically significant difference between rigid and lipid cargo velocities. We reasoned that this could be because the force-velocity dependence we assumed in our computational model may not be sensitive enough to lead to differences in cargo velocity with changes in cargo surface fluidity. It may also be that the heterogeneity in single motor velocity often seen in mixtures of motors purified from cells [121, 113] show heterogeneity in their single motor velocities. In fact, it was suspected that this heterogeneity in single motor velocity could be leading to the observed higher lipid cargo velocity [94], although it wasn't explained how heterogeneity could lead to higher velocity.

In this study, we performed cargo transport simulations by motor teams with varying levels of heterogeneity in their individual motor velocities. Our findings indicate that a substantial degree of heterogeneity in single motor velocity is crucial for achieving higher lipid cargo velocities. We explain this increased velocity through an analysis of cargo and motor dynamics, the velocity contribution from cargo recentering mechanisms, and the delay in strain generation. Furthermore, we investigated the impact of heterogeneity in motor velocity on runlength (the average distance traveled by cargo) and showed that lipid cargoes can traverse a specified distance with a smaller proportion of slower motors while maintaining a higher overall cargo velocity.

4.2 Methods

We used the same computational model as described in Chapter 2 with the added feature that each motor could have a unique single motor velocity $v_{o,mot}$. To take into account the physiologically relevant heterogeneity in motor velocities, we

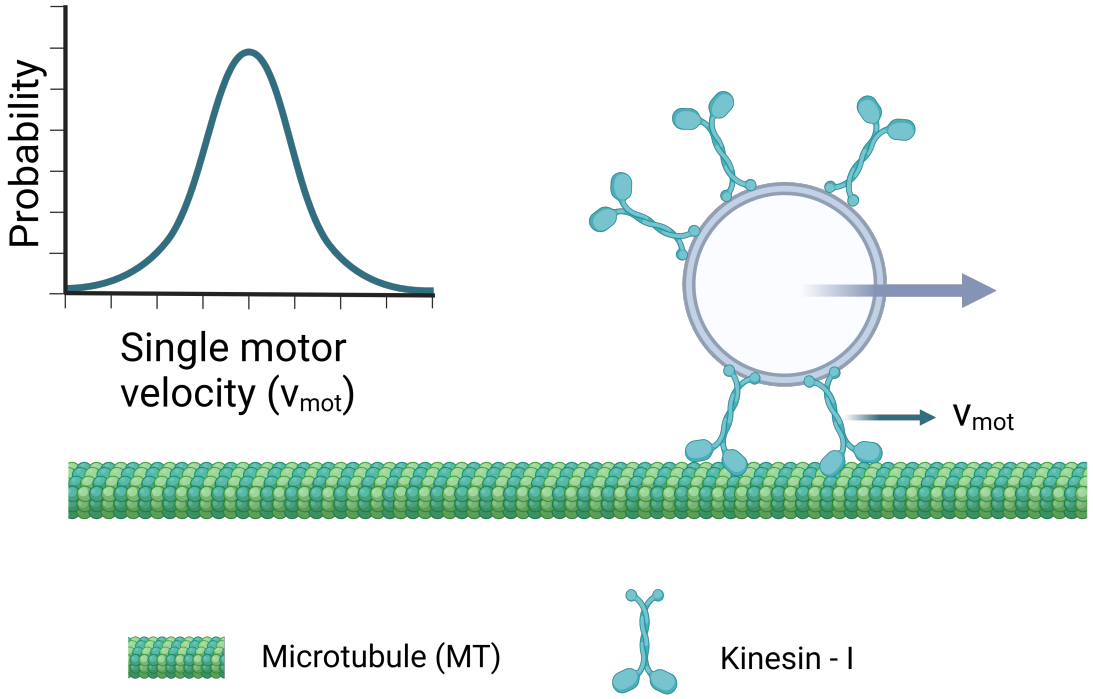

Figure 4.2.1: **Schematic of the heterogeneous motor teams model.** The velocity of a motor v_{mot} depends on the force that it is experiencing and its intrinsic unloaded motor velocity $v_{o,mot}$. The unloaded motor velocity $v_{o,mot}$ is different for each motor, and they are drawn randomly from a given probability distribution like the one shown on the left. Created with BioRender.com

considered experimentally observed heterogeneity in motor populations as input to our model. Specifically, we used a normal distribution and a bi-delta distribution, as explained in the results section. We assign to each motor a mean unloaded motor velocity $v_{o,mot}$, which was drawn randomly from a given probability distribution. In our model, the unbinding rates of motors are effectively proportional to their stepping rates. Thus slower motors effectively spend longer times associated with microtubules.

4.3 Results and Discussions

4.3.1 Heterogeneity is essential to explain experimentally observed differences in rigid and lipid cargo velocities

We wanted to first find a computational model with the least set of assumptions that show a velocity difference between rigid and lipid cargoes. While models have shown this velocity difference, [113] they had a few assumptions. First, it was assumed that every step of the motor results in a spike in its force. If the motor is attached to lipid cargo, the tangential component of this force relaxes quickly because of the sliding of motor attachement point on the membrane. If it is rigid (or gel-state) cargo then such force relaxation is much slower. While our previous computational model [125] showed that there is indeed a reduction in forces experienced by motors in lipid cargo, it is only true statistically, and force trajectories don't show a spike and eventual relaxation every time a motor steps. Second, it was assumed that the center of mass of the cargo fluctuates about a point that is the mean of front and rear-most motor positions. We were curious to know if we are able to see the velocity difference between rigid and lipid cargo in a 3-dimensional Brownian dynamics simulation of cargo transport by teams of motors independent of additional assumptions of motor force relaxation and cargo recentering.

Surprisingly our initial simulations of 3-dimensional cargo transport by teams of motors, reported earlier [125] didn't show any difference between rigid and lipid cargoes. We reasoned that this independence of cargo velocity to fluidity of the membrane could be because the force-velocity curve we used in our simulation is not sensitive enough or as previous works [94] pointed out, this may be due to the presence of heterogeneity in velocities of motors in the team.

To test if heterogeneity could lead to differences in lipid and rigid cargo velocities, we introduced a heterogeneity to our model by incorporating a normal distribution to single motor velocity with a standard deviation of σ=20 $nm\ s^{-1}$ [152]. In this case too, no statistically significant difference was seen between rigid

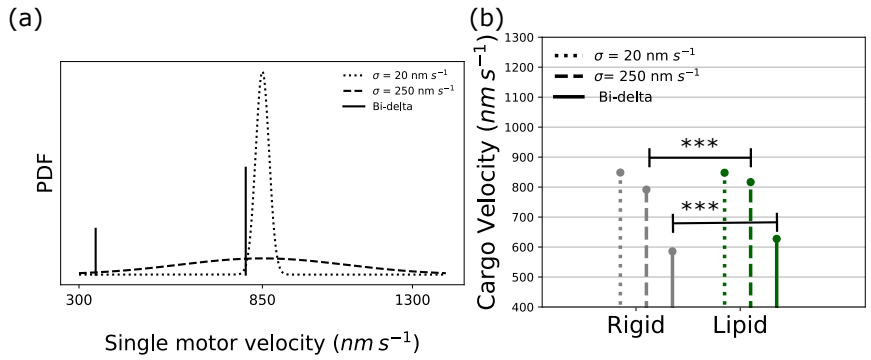

Figure 4.3.1: **Heterogeneity is essential to explain experimentally observed differences in rigid and lipid cargo velocities.** (a) The three different single motor velocity distributions considered in our study, normal distributions with σ= 20 nm/s, σ = 250 nm/s and bi-delta distribution - two different velocity populations with velocities 350 nm/s and 800 nm/s at the population ratio of 0.3:0.7. When we initialize cargoes, we assign to each motor its unloaded velocity drawn from these distributions. (b) The resultant cargo velocity for three different input single motor velocity distribution. To measure velocity, we obtained cargo position data from the simulations of transport of cargo by teams of motors with the given single motor velocity distribution. For each cargo run, we recorded the cargo position data at a sampling rate of 100 s^{-1}. 200 such cargo runs were considered for each parameter set. Cargo velocity was then measured as the ratio of mean displacement along the x-axis in a given time window to δt (we took δt = 0.1 s). Error bars denote the standard error of the mean (error bars are very small and hence not visible in the figure). For all cases, the number of motors on the cargo was $N = 16$ and ATP concentration in the medium, [ATP] = 2 mM. For lipid cargoes, we considered a motor diffusion constant of $D = 1\,\mu m^2 s^{-1}$.

and lipid cargo velocities (Fig. 4.3.1b). We thought this could be because the heterogeneity that we considered wasn't sufficient to cause a significant difference in cargo velocities. In fact, previous experimental works have reported a higher relative heterogeneity in single motor velocity in teams of kinesins [121] and also in teams of myosins [113] as quantified by the spread in the single motor velocity distribution. When we used a high heterogeneity, normal distribution with σ =250

$nm\ s^{-1}$ (Fig. 4.3.1a), we observed a higher velocity for lipid cargoes. This shows that heterogeneity in single motor velocity could lead to a difference in rigid and lipid cargo velocity. To confirm that heterogeneity in single motor velocity leads to velocity difference, we tried another case of heterogeneity, as seen in kinesin-I motors purified from drosophila embryos [121], two sub-populations of motors with velocities 350 $nm\ s^{-1}$ and 800 $nm\ s^{-1}$ at a population ratio of 0.3:0.7 respectively. We took an approximation to this distribution, a bi-delta distribution (Fig. 4.3.1a). This case also resulted in a higher velocity of lipid cargoes, confirming that heterogeneity in single motor velocity leads to higher velocity of lipid cargoes.

Our observations compare well with previous experiments on cargo transport by teams of kinesin-1 motors [94]. Here it was found that the velocity difference between rigid and lipid cargo is an increasing function of the motility fraction (a proxy for the number of motors on the cargo). This velocity difference varies from about 25 $nm\,s^{-1}$ at low motility fractions to about 150 $nm\,s^{-1}$ at very high motility fractions [94]. Interestingly, the value of velocity difference that we observe, about 30 $nm\ s^{-1}$ is within this range. In addition to that, we observe velocity difference between rigid and lipid only at high numbers of motors on the cargo (See Appendix, Fig. 4.A.1) consistent with experimental observations. However, experimental data [94] shows the velocity difference between rigid and lipid arises not because the velocity of lipid cargo increases with increase in motility fraction but rather because the velocity of rigid cargo decreases while the lipid cargo velocity remains constant. Thus one could argue that the lipid cargo is not moving faster than average, but in fact, rigid cargo is moving slower. This indicates that other mechanisms might be at play, which are not accounted for in our model. Specifically, steric interactions between motor stalk regions and the resulting mechanical interferences might be causing rigid cargoes to move slower than lipid cargoes in teams of kinesins. Lipid membranes could be reducing these interferences restoring the velocity. Improvements to the mechanical model of motors and a three-dimensional structure of microtubule lattice are needed to incorporate these effects into our model and address this possibility.

However experiments on teams of myosin Va [113] show that lipid cargoes move faster than average single motor velocity, indicating that velocity difference between lipid and rigid (gel state) is coming because of the additional velocity lipid cargoes gain due to underlying motor dynamics. This is in agreement with our simulations. However, in this experiment, it was observed that the lipid cargo velocity decreases with an increase in the number of motors on the cargo. This might be because of the actin site exclusion and resulting jam between myosin Va motors. Our model doesn't take into account the filament site exclusion - the fact that one site can be occupied by only one motor at a time. While this assumption of no site exclusion is reasonable for kinesin transport on microtubules that have multiple protofilaments, site exclusion might be important for myosin motor transport on actin filaments that have only two protofilaments. This might explain the discrepancy between our simulations and experimental observation of velocity at high motor densities. In this experiment [113], it was also pointed out that the lipid cargo velocity increases with an increase in the cargo size while rigid cargo velocity remains constant. While we see a trend that confirms this experimental observation (See Fig. 4.A.2), there are also high fluctuations that make it difficult to say with certainty whether the lipid cargo velocity increases with an increase in cargo size.

Overall our simulations could reproduce the experimentally observed increase in lipid cargo velocity and show that the underlying heterogeneity in single motor velocity is crucial for this observation.

4.3.2 Enhanced lipid cargo velocity is explained by delay in strain generation between slow and fast.

We wanted to understand the mechanisms that lead to higher lipid cargo velocities. For simplicity, we focused on the bi-delta case (mixture of slow, 350 $nm\,s^{-1}$ and fast, 800 $nm s^{-1}$ motors at a population ratio of 0.3:0.7). Since we had a simple case, a mixture of slow and fast motors with defined velocities, we hoped to find

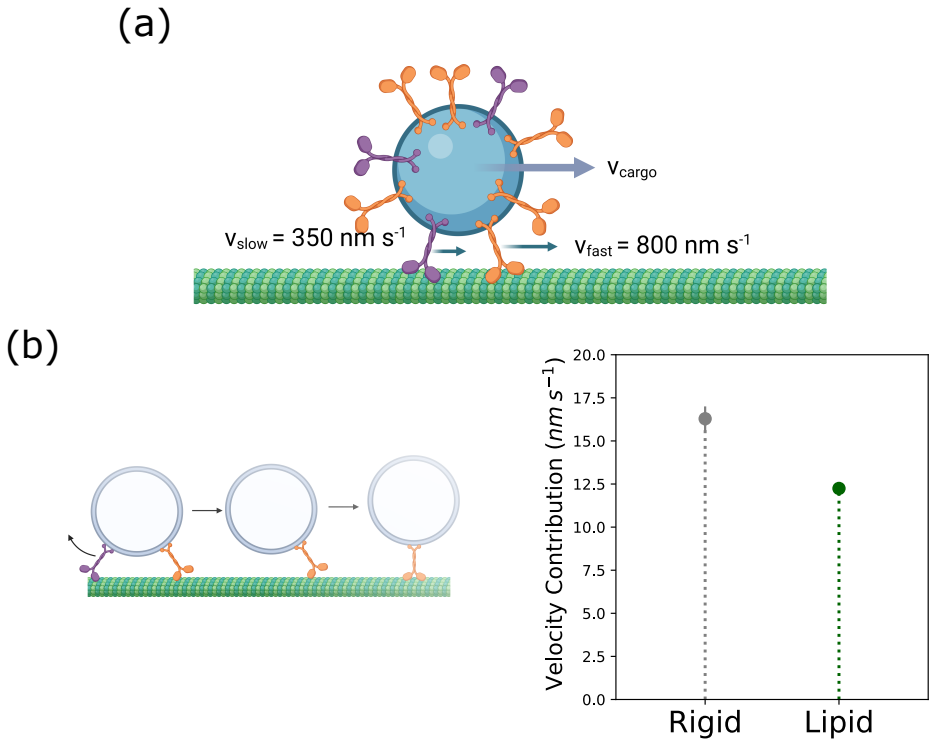

Figure 4.3.2: **Cargo recentering mechanism doesn't account for the observed velocity difference between slow and fast motors** (a) Schematic of the cargo-motor system considered in this section. Single motor velocities of motors were 350 nm/s (slow) and 800 nm/s (fast) at a population ratio of 0.3 to 0.7 (a bi-delta distribution) (b) Illustration (left) and quantification (right) of the contribution to cargo velocities from cargo recentering mechanism. Error bars are calculated from the error propagation method described in the text. Created with BioRender.com

an analytical estimate of cargo velocities as a starting point for our explanations. If we assume that only one motor is bound at a time, this motor could be slow or fast; the probability of it being slow or fast depends on the population ratio and the mean lifetime of these motors. We then computed the average of slow and fast motor velocities weighted by the corresponding lifetime of slow and fast motors, which is $v_{est} = 486.9\ nm\ s^{-1}$, clearly lower than the observed cargo velocities of about 600 $nm\ s^{-1}$. It could be because, most of the time, more than one motor is bound, and faster motors could be enhancing the detachment of slower motors.

We looked at the probability distribution of the number of bound motors, and only 30 to 40 % of the time, it is singly bound (See Appendix Fig 4.A.3). If we consider that more than one motor is bound, it becomes important to take the mechanics into account since the velocity difference between motors could induce a strain between them which could impact the motor and cargo velocity. In fact, forces experienced by slow and fast motors do show such a strain build-up between slow and fast motors; when the lagging slow motor detaches this additional strain experienced by the fast motor drops (See Appendix Fig 4.A.4).

In previous works, it has been emphasized that the increased cargo velocity of lipids is because there is a preferential detachment of lagging motors, and after a lagging motor detaches the cargo quickly recenters, which gives an additional boost to cargo velocity (Schematic of the mechanism is in Fig. 4.3.2(b)). It was explained that there is a higher contribution from such a cargo recentering effect for lipid cargo since the lipid membrane allows for relaxation of the tangential component of force, resulting in the situation where a motor that detaches preferentially has a force normal to the cargo surface [113]. Since our simulation allowed us to analyze the dynamics at a single motor level, it was straightforward to analyze the cargo dynamics right after a motor detached from the microtubule and thereby test the hypothesis.

We measured the velocity of the cargo immediately after a motor unbinds, which is observed to decay exponentially as the time window size used for measuring the velocity increases (See Appendix Fig 4.A.5). We fit this data to $v_{\text{cargo}} + \Delta x_f/t$ to get the mean flopping distance $\Delta x_f \pm \delta x_f$ (scipy.optimize.curve_fit, δx is the one standard deviation error in Δx_f). v_{cargo} is the average cargo velocity. Surprisingly, the flopping distance for rigid cargo is higher than for lipid cargo. We also measured the number of flops, *i.e.*, the number of motor detachments, N_f, and the total cargo simulation time, T (equal to the cumulative lifetime of 200 cargo runs). Then we estimated the mean contribution to cargo velocity from the cargo recentering mechanism as $\Delta v_{\text{flop}} = N_f \Delta x_f / T$ and the error as $\delta v_{\text{flop}} = N_f \delta x_f / T$.

Interestingly the contribution to velocity from this cargo recentering was less for lipid cargo compared to rigid cargo (Fig. 4.3.2(b)). Hence cargo recentering mechanism doesn't explain the observed velocity difference between rigid and lipid cargoes. We added the contribution from cargo recentering (Δv_{flop}) to our estimation of cargo velocity (v_{est}) and obtained a value of about 500 nm/s. This too doesn't explain cargo velocity since the cargo velocity measured from simulations is about 600 nm/s. To resolve this discrepancy, we did a closer analysis of cargo and motor

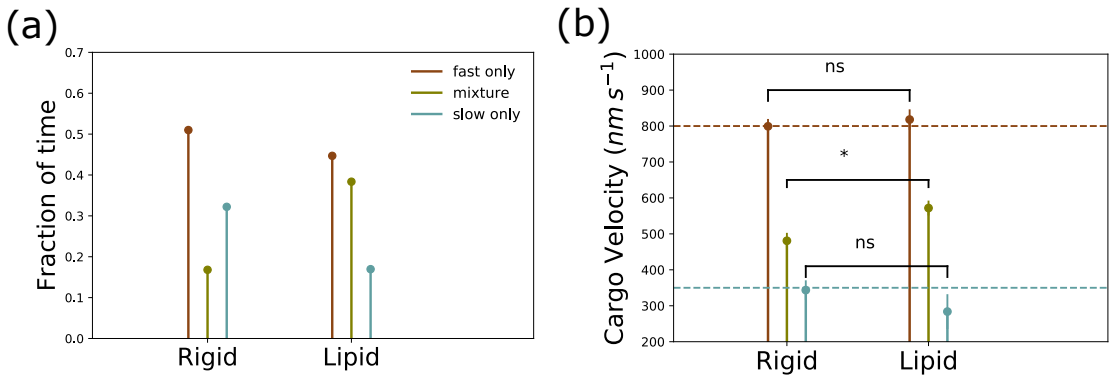

Figure 4.3.3: **Evidence for the delay in strain generation between slow and fast motors in lipid cargoes.** (a) Fraction of time and (b) Mean cargo velocity when cargo is being carried by only fast, only slow, and a mixture of slow and fast motors. To get data in (a) and (b), we first ran simulations of cargo transport with N=16, [ATP]= 2 mM and recorded data at a sampling rate of 100 s^{-1} for 200 independent cargo runs each for rigid and lipid cargo. From this data set, we filtered out time windows where microtubule-bound motors were (i) all fast motors, (ii) all slow motors, and (iii) a mixture of fast and slow motors. To get fraction of time data in (a), we computed the ratio of the cumulative size for each filtered group to the total size of the trajectory data. To get the velocity data in (b), we measured the cargo velocity by computing mean displacements in short time windows (Δt =0.01 s) among each filtered group. Error bars indicate the standard error of the mean. p values were computed from the students-t test. * represents p $\leq$ 0.05 and ns represents p $>$ 0.05.

dynamics when multiple motors are working together. Since motors are moving at different speeds, we expect them to compete mechanically with each other. It

was shown the fluidity of the membrane reduces any mechanical competition in teams of identical motors [125]. We expected that when we have teams of slow and fast motors also, the lipid membrane could reduce the mechanical competition, thereby allowing slow and fast motors to spend more time working together. In other words, lipid membrane could delay strain as mentioned in previous works [94].

In order to test this hypothesis, it is important to look at the typical composition of bound motor teams, whether it is predominantly fast motor only, slow motor only or is it a mixture of fast and slow teams. This is not only a function of the lifetime, and population ratio of motor teams on the cargo but also depends on the mechanical interactions between motors. The fraction of the time cargo is carried by all fast motors, all slow, and the mixture that we measured from the simulated data is given in Figure 4.3.3(a). It can be seen that the fraction of time the cargo is carried by a mixture of slow and fast motors is more in the case of lipid cargo compared to rigid cargo. This means that lipid membrane allows slow and fast motors to spend more time associated with the microtubule simultaneously. This is in agreement with our expectations of reduced mechanical interference in lipid cargoes.

Then we were curious to know what is the cargo velocity when being carried by slow only, fast only or a combination of some fast and some slow microtubule-bound motors. While it is easy to predict what the mean cargo velocity should be when all microtubule-bound motors are fast (or when all are slow motors), it is unclear what the cargo speed should be when some slow and some fast motors are simultaneously bound to the microtubule. One could argue that if any of the MT bound motors is a slow motor, then the entire cargo should be moving with slow motor velocity. However, analysis of simulation data indicates that the cargo velocities when some of MT bound motors are slow, are higher than slow motor velocity (Fig. 4.3.3(b)).

This higher velocity could be because these slow and fast microtubule-bound motors may not be under tension always. This is confirmed by the distribution

of motor forces experienced by slow and fast motors (Appendix Fig 4.A.6) which indicates that slow and fast motors experience low forces (any forces below 5.25 pN - hindering load of 5.25 pN the fast motor velocity reduces to slow motor velocity) for a sufficient fraction of time during the time they are associated with microtubules. We believe that as long as motors experience forces less than 5.25 pN, the fast motors move at velocities higher than the slow motor velocity. Consequently, the cargo center of mass also moves at a velocity higher than slow motor velocities. This velocity is higher for lipid cargo than rigid cargo (Fig. 4.3.3(b), statistical significance confirmed with students-t test, p=0.03) This is because the lipid membrane allows the motors to slide on the membrane and relieve some of its tension. Therefore, in lipid cargoes, the tension between motors with non-identical velocities will be building up at a rate slower than the rate in rigid cargoes. Since the velocities of motors are dependent on the force they experience, a lower time to build tension would mean faster velocities of motors, especially fast motors. As a sanity check, we then measured the average velocity by computing a weighted sum of velocities in each of these states (Fig. 4.3.3(b)), weighted by the corresponding fraction of time (Fig. 4.3.3(a)). This reproduced the correct overall cargo velocity.

Overall the analysis of velocity contribution from cargo recentering mechanism and delay in strain generation mechanism reveals that it is the delay in strain generation that explains the higher velocity of lipid cargoes when carried by heterogeneous teams of motors.

4.3.3 Runlengths increase as the fraction of slow motors increases.

Next, we focused on other biophysical advantages of having a mixture of slow and fast motors in a team. Experimental observations that the heterogeneity in motor velocity is higher than what we would expect from random fluctuations [121] clearly indicates there could be some advantages to having high heterogeneity. This is non-intuitive since identical teams may be better for smoother operations. However, one would expect to have different velocity and runlength requirements for

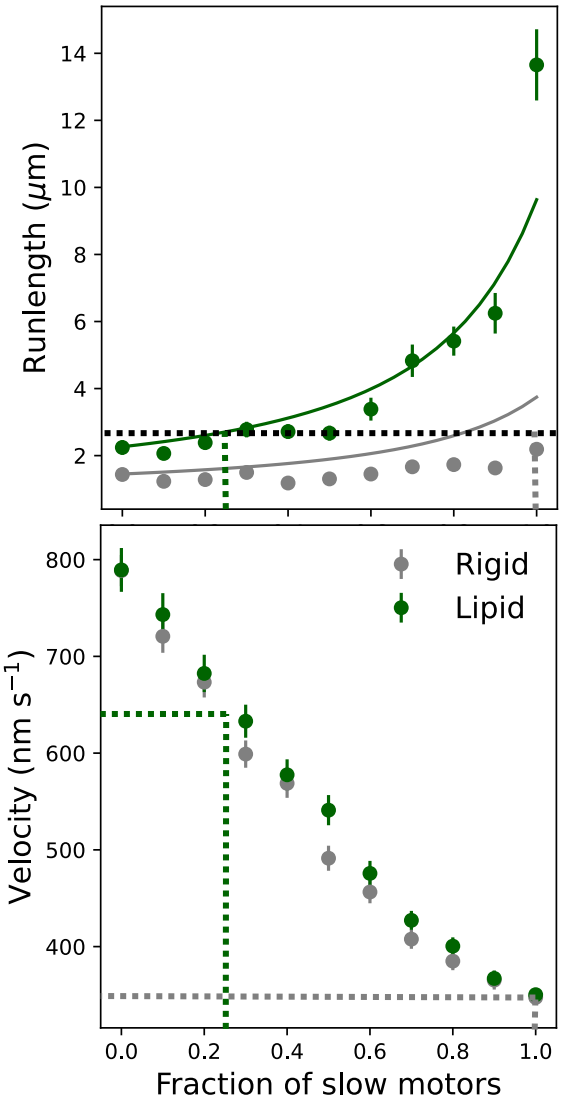

Figure 4.3.4: **Lipid cargo achieves given runlength with a lower fraction of slower motors or with higher overall cargo velocity.** (a) Runlength of the cargo. Circular markers show the mean runlength measured over 200 cargo runs. The solid lines are analytical estimations of cargo runlength by considering the weighted average of the velocity and unloaded motor unbinding rate. (b) Mean velocity of cargoes. We measured velocity using the same method as we followed for the previous figures. Error bars indicate the standard error of the mean. We considered the parameters, $N = 16$ and $[ATP] = 2$ mM for these simulations (same as in previous figures).

different cargoes in cells. Often velocity of motor and runlength of single motors are inter-related. Motors that step slowly often remain associated with microtubule longer [152]. Our computations of cargo transport by teams of motors at low ATP concentration (where motors step slowly) show a higher run length for teams of all slow motors [125]

However, the presence of all or some slower motors in the team is expected to reduce the overall cargo velocity. So we expected that cells might optimize the degree of heterogeneity in order to achieve the desired runlength while also maintaining higher cargo velocity. To explore this optimality, we ran simulations with a varying fraction of slower motors and measured the runlength and velocity of lipid and rigid cargoes. As expected, the runlength increases and cargo velocity decreases with an increase in the fraction of slower motors for both rigid and lipid cargoes (Fig. 4.3.4); the lipid cargo runlength increases more than the rigid. The fact that lipid cargoes have higher runlength than rigid cargoes is in agreement with previous computational studies [125, 25]. Thus lipid cargo can achieve a given runlength with a lower fraction of slower motors or higher cargo velocity. To illustrate this, consider a runlength of 3 μm. Lipid cargo can achieve this runlength with a fraction of about 0.25, hence a cargo velocity of about 630 nms^{-1}. However, rigid cargo needs all motors to be slower motors to travel this distance, hence a cargo velocity of only 350 nms^{-1}.

Thus cells can tune the composition of motor teams depending on the distance that needs to be traveled and the velocity requirements. There is evidence, at least in the context of rigid cargoes, of cells making use of this tunability. These rigid cargoes are intraflagellar particles that move along axonemes in cilia. They are carried by the concerted action of kinesin-II and osm-3 kinesin motors [134, 116]. In the longer middle region of cilia (about 4 μm), IFT particles were observed to be carried by both slow (kinesin -II) and fast (osm-3 kinesin) motors. At the same time, the shorter distal segment (2.5 μm) is found to be traversed by only fast (osm-3 kinesin) motors. Other cases where cells make use of this tunability

remains to be explored.

Analytical estimation of runlength

We use the analytical expression for runlength derived by previous works, [76] that was modified for cargoes of finite size with membranes [125]

$$r = \frac{v_{o,mot}}{N_a \pi_{ad}} \left[\left(1 + \frac{\pi_{ad}}{\epsilon_{o,mot}} \right)^{N_a} - 1 \right] \tag{4.1}$$

Where $v_{o,mot}$, N_a, π_{ad}, $\epsilon_{o,mot}$ are the motor speed, the available number of motors for transport, the single motor binding rate, and the mean motor off-rate, respectively. Considering p_{slow} is slow motor fraction, $v_{o,slow}$ and $v_{o,fast}$ are slow and fast motor velocities, $\epsilon_{o,slow}$ and $\epsilon_{o,fast}$ are mean unloaded unbinding rates for slow and fast motors, we compute the mean motor speed to be $v_{o,mot} = p_{slow} v_{o,slow} + (1 - p_{slow}) v_{o,fast}$, and the mean motor unbinding rate to be $\epsilon_{o,mot} = p_{slow} \epsilon_{o,slow} + (1 - p_{slow}) \epsilon_{o,fast}$. We varied the available number of motors depending on the fluidity of the cargo surface (Please see our previous work for more information [125]). It is interesting to note that even this crude analytical estimation captures the observed runlength from simulations satisfactorily.

4.4 Conclusion

Previous experimental observations [94, 113] showed that membrane-bound cargoes (or lipid cargoes) have higher velocity than membrane-free cargoes when carried by teams of molecular motors. Even though several mechanisms have been proposed to explain this higher velocity of lipid cargoes, a clear quantitative explanation of the mechanisms was lacking. In this study, we show, using a computational model, that underlying heterogeneities in single motor velocities are crucial to observe higher velocities of lipid cargoes. Our simulations showed that the lipid cargoes move with a higher velocity than rigid cargoes only when they are being carried by heterogeneous teams of motors. When motors have different velocities, they develop tension between them as they walk along microtubules. If

the motors are coupled to the membrane, the rate of this strain buildup is slower. During the time in which slow and fast motors build up tension, the cargo can move at a velocity higher than the limiting slow motor velocity. Since this time is higher in lipid cargo, the overall cargo velocity is also higher.

While velocity is one quantity that is of interest to cargo transport in cells, run length is another important quantity. Having some or all slow motors in the team enhances cargo run lengths. We find that the runlength of lipid cargo increases more than the rigid cargo with an increase in the fraction of slow motors. Thus lipid cargoes can traverse a given distance with a lower fraction of slower motors or higher overall cargo velocity. We also estimated the runlength of cargoes with a modified version of a previously established analytical equation [76, 125]. This analytical model seemed to adequately predict the runlengths of rigid and lipid cargoes allowing us to extend the predictions to various other parameter regimes in future studies. Overall, our work elucidates the emergence of cooperativity between heterogeneous teams of motors in cells because of purely physical mechanisms arising from how they are coupled together. We also illustrate that the degree of heterogeneity can be used as a tunability parameter to achieve desired runlength and velocity. However, these predictions need to be verified with experiments of membrane-bound cargo transport by teams of motors with varying levels of heterogeneity.

The central assumption in our model is that the detachment rates of motors decrease with a decrease in motor velocities. We assumed that all the motors are kinesin-I motors, and the rate of the detachment of motors from microtubules is expected to be directly proportional to the velocity of motors. However, cellular cargoes can have motor teams that are made up of different motor types. It remains to be seen what effects do such heterogeneities have on the transport by teams of motors. A more detailed study of cargo transport by teams of motors with different complexity, such as mixtures of different types of kinesins; kinesin, myosin, and dynein together and other heterogeneities, is necessary to understand the functional relevance of all these heterogeneities in cells and relevant tunability

parameters to regulate this transport.

Notes

4.A Supplementary Figures

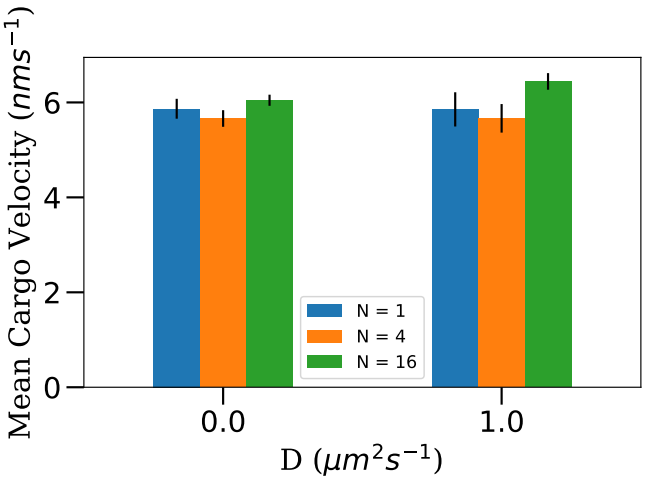

Figure 4.A.1: **Velocity of cargo as a function of the number of motors on the cargo for rigid (D=0) and lipid (D=1 $\mu m^2 s^{-1}$) cargoes.** Single motor velocities were 800 $nm\ s^{-1}$ and 350 $nm\ s^{-1}$ at a population ratio of 0.7:0.3. All cargo simulations were performed at saturating ATP concentration of 2 mM. 200 cargo runs were simulated in each case. For each run, the data of cargo positions were collected at a sampling rate of 100 s^{-1}. The cargo velocity was then calculated by measuring the mean displacement of cargo Δx in a time interval of $\Delta t = 0.01\,s$. $v_c = \Delta x / \Delta t$

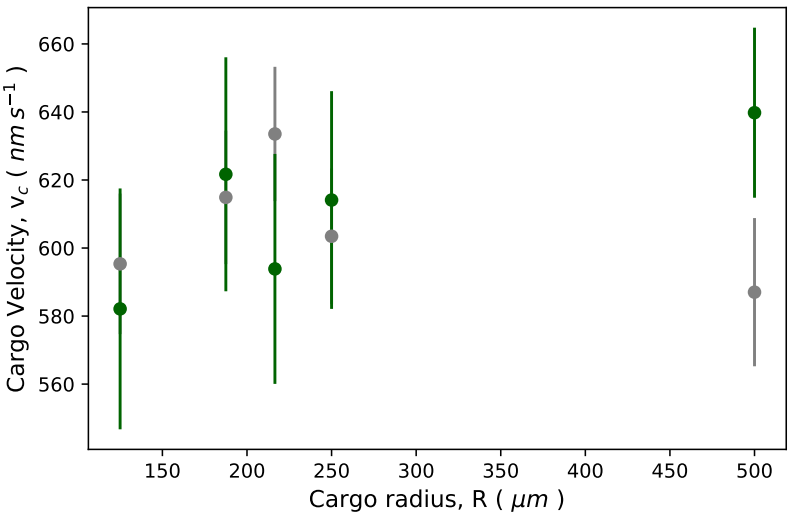

Figure 4.A.2: **Velocity of cargo as a function of cargo radius for rigid (D=0) and lipid (D=1 $\mu m^2 s^{-1}$) cargoes.** Single motor velocities were 800 $nm\ s^{-1}$ and 350 $nm\ s^{-1}$ at a population ratio of 0.7:0.3. All cargo simulations were performed at saturating ATP concentration of 2 mM. 200 cargo runs were simulated in each case. For each run, the data of cargo positions were collected at a sampling rate of 100 s^{-1}. The cargo velocity was then calculated by measuring the mean displacement of cargo Δx in a time interval of $\Delta t = 0.001 s$. $v_c = \Delta x / \Delta t$. Grey color represents a rigid cargo, $D = 0$ and Dark green represents a lipid cargo, $D = 1\ \mu m^2 s^{-1}$.

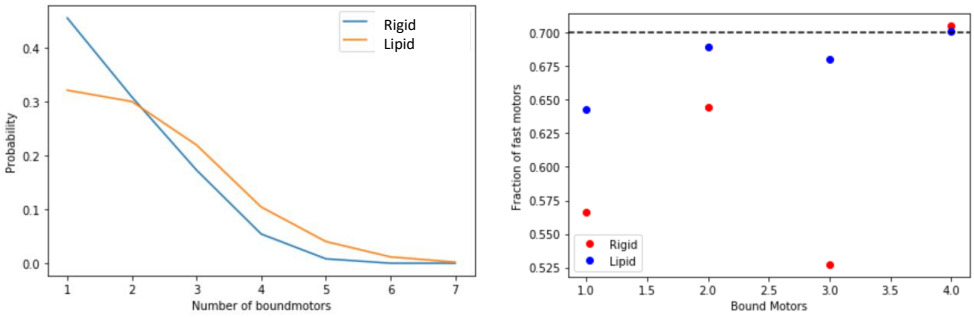

Figure 4.A.3: **Bound motor statistics.** (Left) Probability distribution of the number of bound motors in rigid and lipid cargoes. (Right) Fraction of fast motors for a given number of bound motors. To get data in we ran simulations of cargo transport with $N = 16$ motors at [ATP]= 2 mM and recorded data at a sampling rate of 100 s^{-1} for 200 cargo runs each for rigid and lipid cargoes.

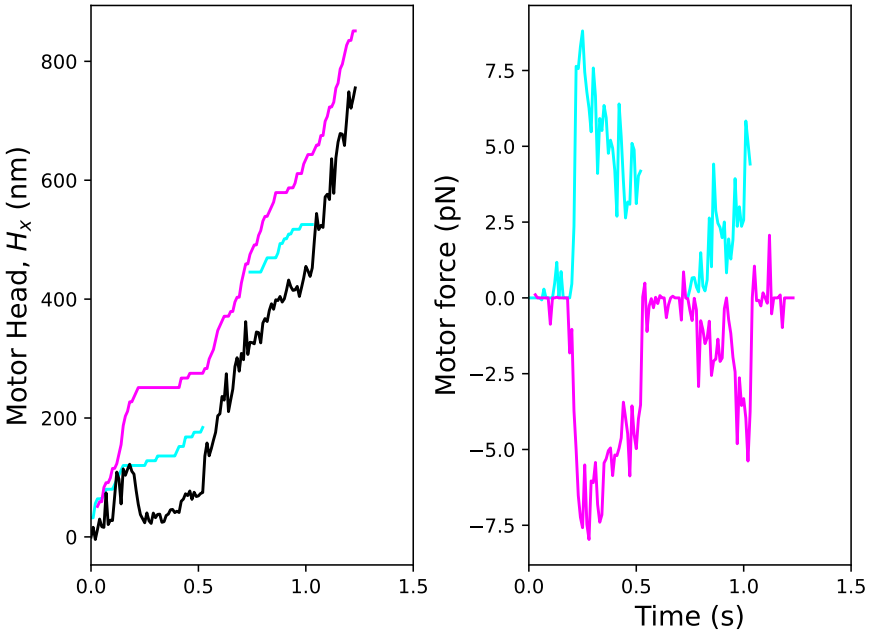

(a) Rigid Cargo

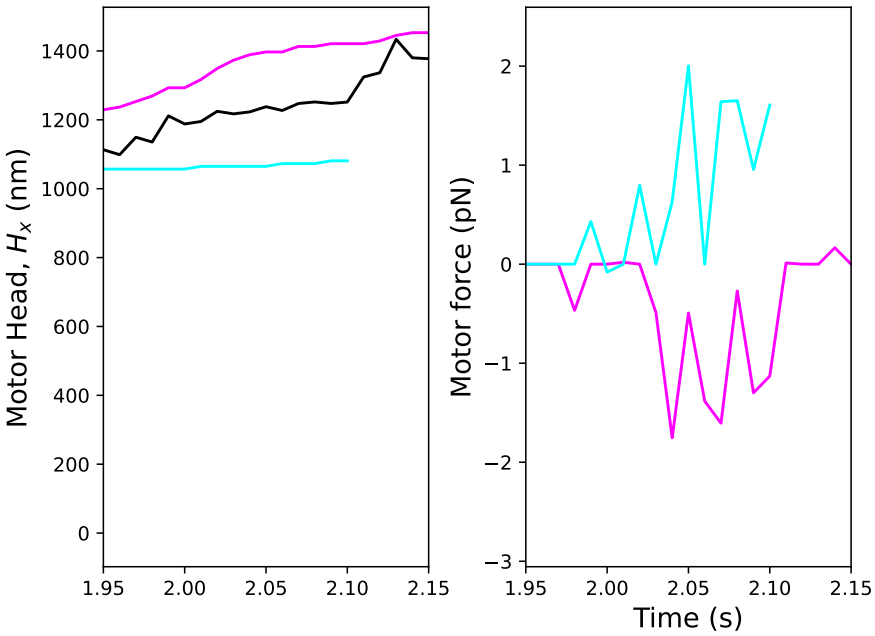

(b) Lipid Cargo ($D = 1\,\mu m^2 s^{-1}$)

Figure 4.A.4: **Position and forces of motors in rigid and lipid cargoes.** Fast motors are colored in magenta; slow motors are colored in cyan. The black line represents the center of mass of the cargo. Negative force values indicate hindering forces, and positive force values indicate that the motor is experiencing assistive forces. The data were collected from cargo transport simulations with a data sampling rate of 100 s^{-1}. From these data, we selected a window where a fast and slow motor are simultaneously bound. The single motor velocities were 800 $nm\,s^{-1}$ (fast) and 350 $nm\,s^{-1}$ (slow) at a population ratio of 0.7:0.3.

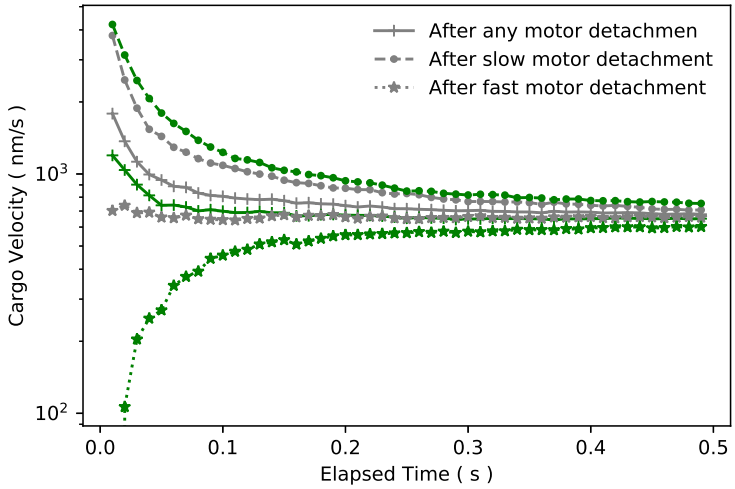

Figure 4.A.5: **Average cargo velocity as a function of the time elapsed from motor detachment.** We ran simulations with N=16 motors at [ATP]=2 mM and recorded cargo and motor position data for 200 cargo runs each for lipid and rigid cargoes at a sampling rate of 100 s^{-1}. In this time series data, we identified time points where a motor detached and measured the mean displacement of cargo Δx_d, in a time window Δt after such time points. Then we measured velocity as $v_c = \Delta x_d / \Delta t$.

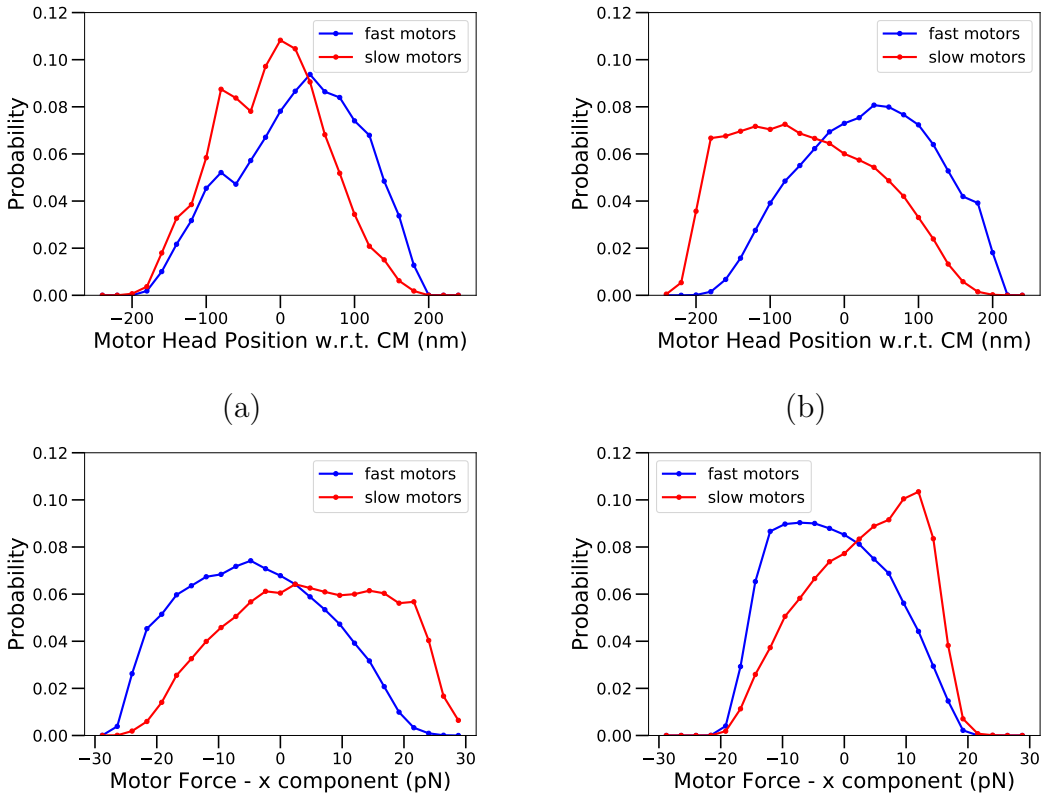

Figure 4.A.6: **Distributions of motor head positions relative to the center of mass of the cargo.** (a) Rigid cargo and (b) Lipid cargo. Distribution of x-component of motor force in (c) Rigid and (d) Lipid cargoes. Data obtained from cargo simulations performed at high ATP with 16 motors. Population ratio of fast (800 nm s^{-1}):slow (350 nm s^{-1}) is 0.7:0.3

Chapter 5

Cargo transport across roadblocks

This chapter discusses how lipid membranes could impact cargo transport across roadblocks on microtubules. We perform simulations of cargo transport across a variety of roadblocks and analyze the probability of passing, the duration of pauses near roadblocks, etc. as a function of the cargo surface fluidity. We find that lipid membranes increase pass probabilities of cargo under certain physiologically relevant conditions. These results have implications for research on cures for several pathologies that involve a breakdown in transport.

5.1 Introduction

Genetic studies show that the enrichment of amyloid plaques and neurofibrillary tangles leads to the onset of neurodegenerative diseases like Alzheimer's [107, 56, 68]. There are also separate pieces of evidence for deficits in transport in brain cells of patients with such diseases [107]. Such molecules, specifically tau protein is known to disrupt cargo transport by acting as a roadblock on the microtubule path [145]. Hence the disruption in transport due to the presence of different roadblocks on microtubule paths is linked to diseases like Alzheimer's. There can be different kinds of roadblocks on microtubule lattice in cells, which include Microtubule Associated Proteins (MAPs) such as the tau protein. More generally, a variety of decorating proteins, stalled cargo or other structures in the crowded cytoplasm can act as roadblocks. Intracellular environment is crowded with proteins and other

molecules which cover more than 20-30 % of the cellular volume. In addition to that the environment is composed of cytoskeletal networks and vesicles, organnels which hinder the cargo transport [102, 65]. Typical mesh size of cytoskeletal networks is $\approx$ 50 nm [102] whereas typical cargo sizes are in the range of 50-1000 nm. Cargoes in the size range 50-250 nm may not experience intracellular environments as a continuous medium. In addition, the cytoskeletal filaments themselves may have elements that hinder transport such as protein aggregates, missing tubulin sites along protofilaments, and defect sites between annealed microtubules [52].

Because of these reasons, extensive research has been done to understand the effect of roadblocks on cargo transport. In vitro experiments found that a given concentration of tau affects multiple kinesin-based transports more than dynein-based transport suggesting that tau concentration on microtubules may be used to regulate anterograde and retrograde transport of cargoes [146, 144]. However several issues still remain. One unanswered question is whether the lipid membrane on a cargo offers it any advantage in navigating around different roadblocks. We seek to answer this question for two different kinds of roadblocks - (a) roadblocks of the size of a single binding site, such as microtubule-associated proteins (MAPs), inert microtubule-associated motors, defect sites, etc., and (b) roadblocks that cover microtubules as a ring, referred as *hurdles* hereafter. Examples of hurdle like roadblocks are regions where microtubules with two different protofilament number anneal, regions where microtubule protofilament number changes, etc. These two roadblocks are fundamentally different in that the former one can be avoided by sidestepping of motor or in the case of multi-motor transport by a new motor binding to neighboring protofilaments. Later one can be navigated only by multi-motor cargoes by new motor binding to regions beyond the roadblock. In this chapter, we discuss lipid membrane-associated physical mechanisms that help cargoes to navigate over these different roadblocks on microtubules.

5.2 Results and Discussions

5.2.1 Lipid membranes have negligible influence on the probability of small kinesin teams crossing single-binding-site-sized roadblocks.

Microtubules are hollow cylindrical shells made up of tubulin dimers. Each tubulin dimer is made up of repeating subunits named α and β subunits. Tubulin dimers have two kinds of interaction with each other. First, a longitudinal interaction between tubulin dimers that leads to a linear protofilament, and second, a lateral interaction that results in these protofilaments organizing into a tubular structure.

It is observed that kinesins track a single protofilament as they move along the microtubule [120]. Motors often find that the next tubulin dimer in their path is not available for binding, either because it is occupied by some MAPs like tau protein, other molecular motors or it is missing due to defects [95]. Such roadblocks which are of the size of one tubulin dimer are particularly important for cargo transport *in vivo*. The behavior of motors on these roadblocks depends on the nature of roadblocks. The binding rate of kinesins to MT was observed to decrease in the presence of MAPs and other kinesins [138]. Kinesins encountering such small roadblocks were observed to stop and wait there without detaching [80, 39], leading to lowered average motor velocity [80]. Other interesting behaviors in special cases were also reported. For example, single-headed kinesin monomers encountering such roadblocks were observed to detach more readily than pause at the roadblock [138]. Here, roadblocks impact the runlength of kinesins, but the kinesin velocity is not affected.

While the behavior of single kinesins at roadblocks and intersections is well characterized, the effect of roadblocks on transport when multiple kinesins are coupled together is less well-understood. Some studies suggested that multiple motors have a higher probability of crossing roadblocks than single kinesins [46, 139].

Mechanisms that lead to this higher probability of passing remain to be explained. Interestingly, even though individual kinesin motors were observed to have a low but finite probability of protofilament switching [138], two kinesins coupled to cargo were found to have significant protofilament switching rate [6]. Furthermore, the effect of lipid membrane in this process of crossing over roadblocks is not addressed theoretically.

Here we implement roadblocks of the size of one tubulin dimer to our Brownian dynamics model by considering that a microtubule-bound motor encounters a roadblock with some probability, P each time it makes a step. When a motor encounters a roadblock, we assume that it stays there until it detaches from the filament stochastically. Firstly, we investigated how the variation in roadblock probability, P affects the run length, velocity, and lifetime of cargoes for different diffusion constants of motors on the cargo surface, D. The results are shown in Fig. 5.2.1. Cargo simulations were performed for $[ATP] = 2$ mM and $N = 4$. The runlength of cargo decreases non-linearly as a function of P. We show using analytical calculations that the dependence of runlength with P can be shown to be

$$r = \frac{1}{(P/\delta + k_{off}/v)} \tag{5.1}$$

δ is the step-size of motor. k_{off} is the mean detachment rate of motors. (See Appendix 5.A for derivation). There is no noticeable variation in runlength as a function of the diffusion constant (See 5.2.1). The velocities of cargoes also show a similar trend as the run length. The lifetimes of cargoes are found to be independent of P and D (See Fig. 5.C.1 in Appendix). Overall these results indicate that lipid membranes don't influence the ability of the cargoes to navigate roadblocks of the size of a single binding site when carried by small teams of kinesins at saturating ATP conditions.

We wanted to explore further to see if the lipid membranes have any subtle effect in navigating across roadblocks. Probability of cargo pausing is an indicator of the degree to which roadblocks affect transport. We were curious to know if lipid

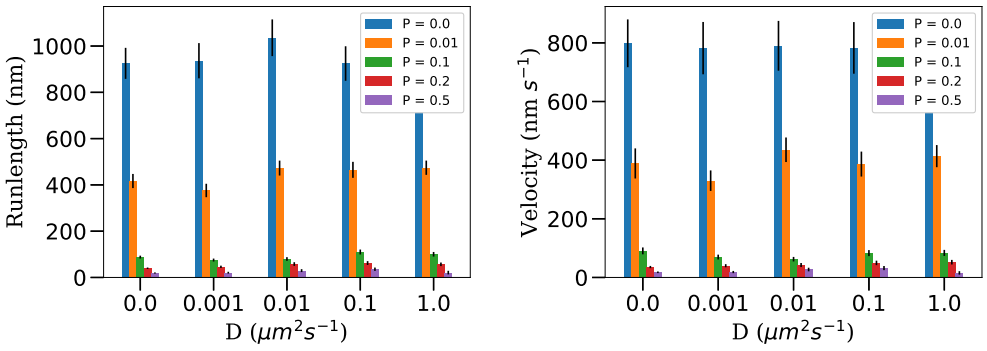

(a) (b)

Figure 5.2.1: **Cargo transport across roadblocks of the size of a single binding site.** (a) Runlength, and (b) Cargo velocity as a function of the probability of encountering a roadblock on the next site (P) and diffusion constant of motors on the cargo surface (D). Values were averages over 200 cargo runs. $[ATP] = 2$ mM (staurating ATP) and $N = 4$. Error bars represent the standard errors of means.

membrane changes this probability of pausing at roadblocks, possibly by faster rescue using new motor bindings. We plotted the distribution of the displacements of the cargoes and extracted the probability of cargo pausing from this distribution. We observed that the probability distributions of displacements (Fig. 5.2.2(a)) have two peaks, a peak centered at $\Delta x = 0$ corresponds to trapping due to the roadblock (pause state), and a peak centered around $\Delta x \approx 0.8\,\mu m$ corresponds to the motion due to motor activity. It is hard to quantify the changes in the pause and motile states as a function of the diffusion constant from this plot because with a change in D, the width of the peak also changes in addition to the peak height because lipid membrane allows for more fluctuation about the mean.

To quantify how variables P and D affect the probability of pause and motile states, we measure pause probability from the step distribution defined as the area under the probability distribution curve for $\Delta x < 0.4\,\mu m$ (Fig. 5.2.2 (b)). It can be observed that the pause probability increases with an increase in P and

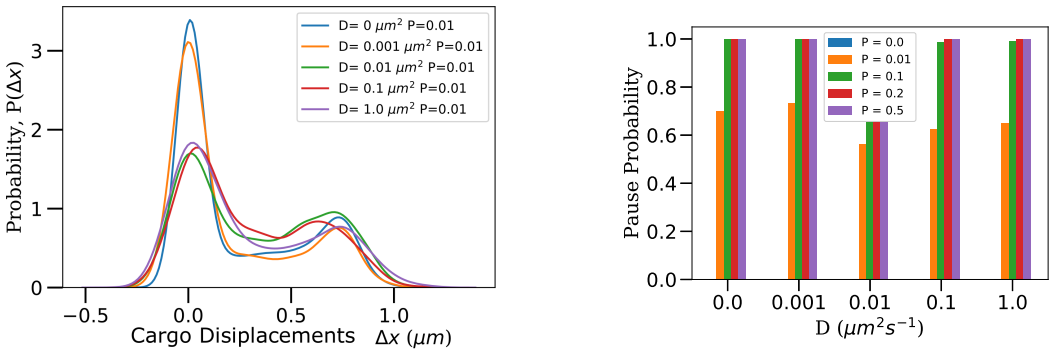

(a) (b)

Figure 5.2.2: **Analysis of cargo interaction with roadblocks.**(a) Probability distribution of displacements Δx (displacements along x-axis) of a cargo in Δt= 1 s for P=0.01. The number of displacement samples collected were 8000. The curves are the kernel density estimates (kde) obtained using distplot method of seaborn module in python. (b) Pause probability as a function of the diffusion constant and roadblock probability (P). Pause probability was estimated as the area under the probability distribution curve for $\Delta x < 0.4\,\mu m$. Data was from cargo transport at saturating ATP conditions, [ATP] = 2 mM with N=4.

decreases with an increase in D. Pause probability is 0 for P=0 while Pause probability is one for P>0.1. For P=0.01, Pause probability is more for D=0 and D=0.01 compared to higher diffusion constants. Another quantity of interest is the mean time cargo spends being stuck at a roadblock (pause state). Using our simulation model, we explored how this pause time varies as a function of D and P. We defined the pause state as the state where at least one motor is trapped by a roadblock in simulation. We first plotted the distributions of pause times (Fig. 5.2.3(a)) and then obtained mean pause time from these distributions (Fig. 5.2.3 (b)).

Although currently, we don't consider roadblocks that increase the detachment rate of kinesin, it might be interesting to include that in our model. Some physiologically relevant roadblocks like tau protein could potentially increase the

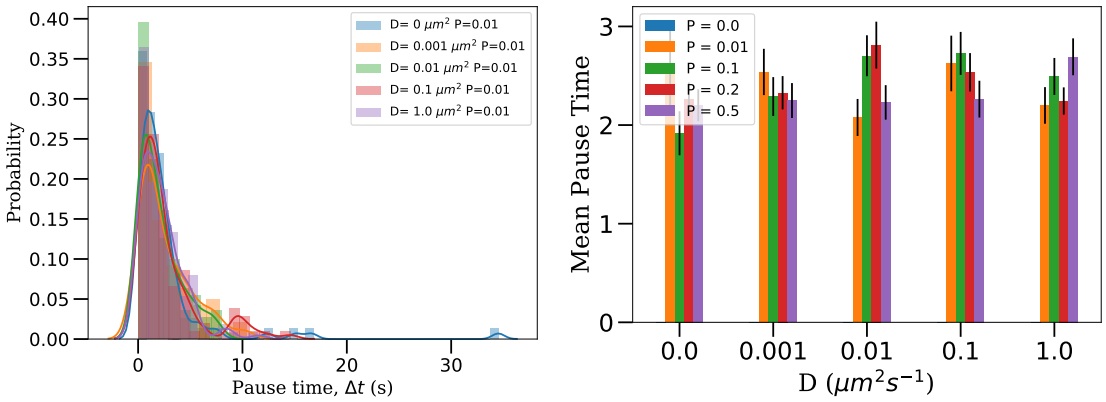

(a) (b)

Figure 5.2.3: **Pause time statistics.** (a) Distribution of pause times for different diffusion constants for P=0.01. Pause state is defined as the state in which at least one motor is stuck at a roadblock (b) Mean pause time as a function of P and D. The same parameters were used for cargo transport simulation as in the previous figure.

detachment rate of kinesins [138]. Including this parameter of detachment rate in our model will explain whether premature detachment of motors at the roadblock is helpful for cargo transport. Another possible direction of improvement to the model is including the possibility of motor avoiding the roadblock by side-stepping to a different protofilament. It is observed that even though single kinesins don't have a significant protofilament switching rate when two kinesins are bound to the same cargo, they seem to have a significant protofilament switching rate [6]. Other motors, like dyneins are known to have much higher side-stepping probability [26].

Overall our results suggest that lipid membranes may not influence cargo navigation across roadblocks of the size of a single binding site when carried by small teams of kinesins at saturating ATP conditions. However, as described in Chapter 3, the runlength of kinesin motor teams generally increases with a decrease in the ATP concentration and an increase in the number of motors on the cargo, and lipid cargoes have higher runlength than rigid cargoes in these regimes. Hence, one would expect lipid cargoes to navigate roadblocks better than rigid cargoes at

lower ATP concentrations or when there is more number of motors on the cargo, but this is just because of the general increase in runlength due to the fact that $\tau_{bind} < \tau_{off}$ condition is satisfied as described in Chapter 3 and not because of any new emergent effect.

5.2.2 Lipid membranes enhance the probability of crossing ringlike roadblocks around microtubules.

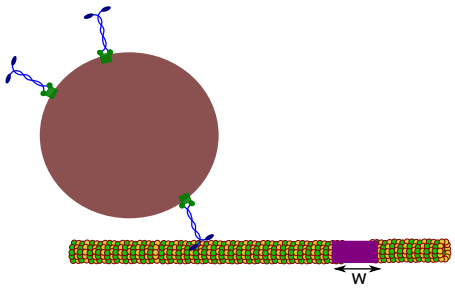

Figure 5.2.4: **Schematic diagram of a hurdle.** Hurdles are ringlike roadblocks around microtubules. They are modeled as a region of width w that is unavailable for motor binding and transport. A motor that walks up to this region gets stuck there until it's stochastic detachment.

The size of roadblocks on microtubules can be greater than the size of tubulin dimers. For example, consider defect sites between two microtubules of different protofilament number annealed together [52]. Such roadblocks are fundamentally different from the roadblocks that cover single-binding sites. We expect cargoes to adopt a different strategy to navigate around these kinds of roadblocks which we refer to as hurdles.

To analyze the mechanisms cargoes use to navigate around hurdles, we implemented these roadblocks in our model by considering that a specific region of the microtubule of width w (Fig 5.2.4), is unavailable for motor binding and transport. Upon encountering the left edge of this region, a motor stops moving and waits until it is unbound. As soon as cargoes bind to a microtubule with one motor, they are typically rapidly taken to the hurdle (See Fig. 5.2.5(a)), then get stuck there

until a new motor binds to a region next to the hurdle and takes the cargo out of the hurdle. The probability of crossing hurdle depends on the number of motors on the cargo N, ATP concentration and the cargo surface fluidity (as quantified by the diffusion constant D). The pass probability increases with diffusion constant at a high number of motors on the cargo, or low ATP concentrations, or both. This is because, as described in Chapter 3, when ATP concentration is low, or the number of motors is high, the mean binding time for a new motor τ_{bind} is low compared to the mean unbinding time of an already bound motor τ_{off}. In this parameter regime, a new motor binds to the microtubule before an already bound motor unbinds in lipid cargoes. This new motor that is bound can bind to a region next to the hurdle and rescue the cargo out of the hurdle. A more careful analysis of this theory and estimation of pass probability is given in Appendix 5.B.

The time to pass hurdle indicates fundamentally different mechanisms employed by rigid and lipid cargoes in crossing hurdle (Fig. 5.2.6). The mean time to pass the hurdle varies non-monotonically with an increase in cargo surface fluidity (Fig. 5.2.6(a)). We refer to this time time as the pause time since it is essentially equal to the time cargo spends being stuck at the roadblock. This is interesting since so far the behavior of transport properties with surface fluidity has been monotonic. The distribution of pause time, Fig. 5.2.6(b) indicates a heavier tail for lipid cargoes consistent with the higher average value of lipid cargoes in Fig. 5.2.6(a). Distribution of mean pause times has a non-monotonic behavior with peak between 5 - 10 s for both rigid and lipid cargoes. The typical cargo trajectories corrsponding to events with this pause time is quite simple (see Fig. 5.2.6(b) i). The cargo is rapidly taken to the hurdle there it waits until a new motor binds to a region next to the roadblock and the new motor(s) take the cargo out of the roadblock and the stuck motor detaches. However, events corresponding to extreme pause times are qualitatively different between rigid and lipid cargoes. In the case of rigid cargoes, trajectories corresponding to extremely long wait times (Fig. 5.2.6(b) ii) indicate the unavailability of motors. But when a new motor binds the cargo quickly goes out of the hurdle. In the case of lipid cargoes, trajectories corresponding to ex-

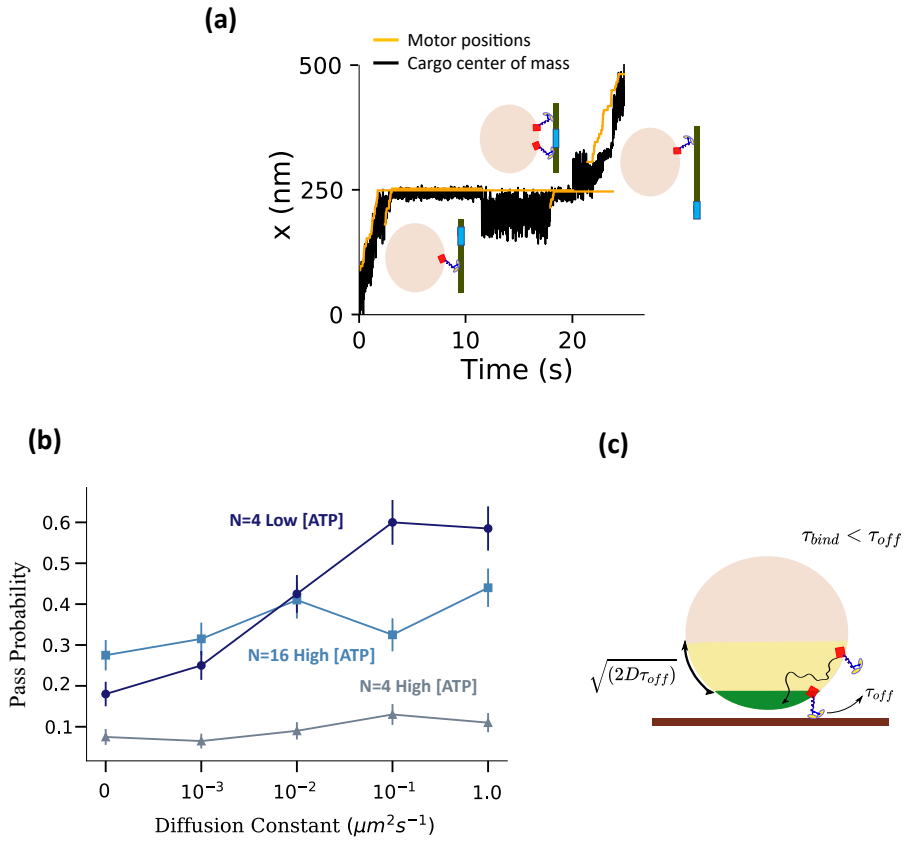

Figure 5.2.5: **Probability of crossing hurdle increases with increase in cargo surface fluidity.** (a) Typical cargo trajectory. Black line: x-position of the center of mass of the cargo. Yellow lines: positions of motor heads along the microtubule. The hurdle is at position $x = 250$ nm. Cargo is said to have crossed the hurdle when no motor can access region below the hurdle, *i.e* when the center of mass of the cargo covers one radius distance beyond hurdle, $x = R + 250$ nm. (b) Probability of crossing the hurdle for cargo with a singly bound motor. Average was over 200 cargo runs. Error bars represent standard error of means. (c) Schematic to illustrate parameter dependence of sensitivity of pass prbability to cargo surface fluidity. Pass probability is sensitive to cargo surface fluidity when mean binding time for a new motor τ_{bind} is less than mean unbinding time τ_{off}, *i.e.* when the number of motors on the cargo N is high or when ATP concentration in the medium is low or both.

tremely long wait times (Fig. 5.2.6(b) iii) indicate failed events. New motors bind multiple times but they are unable to pull the cargo out of the hurdle.

As seen in Chapter 3, the lipid membrane reduces negative intereference between motors. It seems that this interefernce between motors is necessary for motors to pull cargo out of roadblocks. In case of rigid cargo, when a new motor binds to a region next to hurdle, it has good chance of taking the cargo out of hurdle. Because this new motor exerts a force on the stuck motors, and increases it's detachment rate because it is in assistive configuration. Whereas, in lipid cargo, when a new motor binds to region next to hurdle, it cannot always pull the cargo out of hurdle since the effective decoupling of motors due to the presence of membrane makes it difficult for motors in the front to pull the stuck motors out of the hurdle.

So far we considered cargoes that approach hurdle immediately after binding to microtubule. Thus predominantly cargoes had single microtubule bound motors when they approach hurdles. *In vivo* it is also possible that cargoes encounter hurdles with different number of bound motors (initial_bound). The hurdle of width, $w = 16$ nm is located at $x = 250$ nm. The center of mass of each cargo was initialized at $x = 0$. So the hurdle is right at the edge of the cargo (cargo radius is 250 nm). Cargoes are said to have passed only if their CM crosses $x = 500$ nm which is one radius away from the roadblock. We performed simulations for three cargo-motor systems, (i) N=4 at High ATP (2m M), (ii) N=16 at High ATP (2 mM), and (iii) N=4 at Low ATP (4 μ M) for an initial number of motors ranging from 1 to 4 and measured the probability of crossing the hurdle and mean time taken by the cargo to cross the hurdle (Fig. 5.14).

It can be observed from Fig. 5.14 that the pass probability for initial_bound=1 case increases with an increase in the fluidity of the cargo whereas, for initial_bound > 1, it decreases with increase in fluidity although by different amounts depending on the N and ATP values. In general for a given diffusion constant, pass proba-

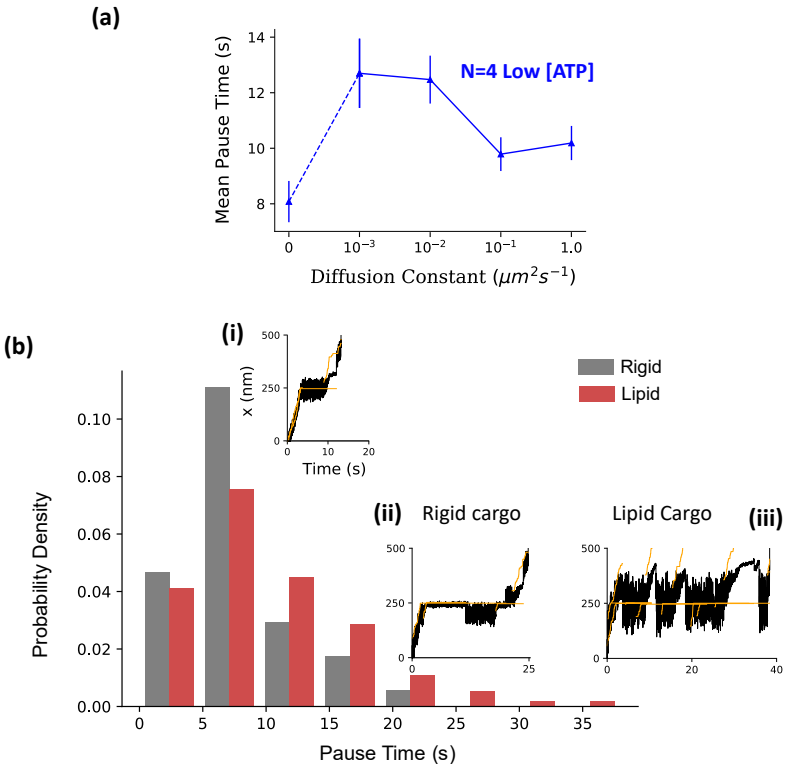

Figure 5.2.6: **Pause time analysis reveals distinct mechanisms used by lipid and rigid cargoes in navigating hurdles.** (a) Mean pause time at the hurdle for cargoes that crossed. Mean was over 200 cargo runs, at $N = 4$ and [ATP] $= 4$ μM. (b) Distribution of pause time for extreme diffusion constant cases, Rigid ($D = 0$) and Lipid ($D = 1\,\mu m^2 s^{-1}$). Insets show the cargo trajectories. (i) Typical cargo trajectory of rigid and lipid cargoes that have pause time near the peak of the distribution (ii) Trajectory of rigid cargo with Pause time about 20 s (iii) Trajectory of lipid cargo with pause time about 35 s.

bility increases with an increase in the initial number of bound motors. The pass probability of rigid cargoes changes only slightly with changes in N or ATP which indicates that the pass probability for rigid cargo has only to do with the motors

available in the access region. However, pass probability of lipid cargoes with high diffusivity significantly varies with changes in N and ATP. It seems that the rebinding rate of motors governs the pass probability. In rigid cargo this ratio this rebinding rate very high in case of initial_bound > 1 since at the motors can't diffuse away as in case of lipid cargo.

Mean time to pass increases with an increase in the diffusion constant for a given initial_bound. For a given diffusion constant, mean time decreases with an increase in the initial_bound for rigid cargo and increases for lipid cargo. This difference in the behavior for rigid and lipid cargoes might be because of different kinds of pass mechanisms in rigid and lipid cargoes.

In cells, cargo may encounter a roadblock at any stage during the transport process. So we calculated the effective probability of passing the hurdles as the weighted average of pass probabilities for individual initial bound motors weighted by the appropriate probability distribution of bound motors (Fig. 5.2.8). (The probability distribution of bound motors was obtained from simulations of Chapter 3.). It can be observed that in High ATP cases the pass probability is independent of cargo surface fluidity. However, for the Low ATP case, pass probability increases with cargo surface fluidity.

5.3 Conclusion

In this chapter, we developed models of cargo transport across roadblocks of the size of a single tubulin dimer and more larger ring-like roadblocks (*hurdles*) on microtubules and more attention was given to hurdle because of relatively less studies in this area. We find that lipid membranes increase the probability of crossing hurdles when they approach roadblocks with single microtubule-bound motors. We also identify qualitatively distinct mechanisms that lipid and rigid cargoes use to cross hurdles. In the case of rigid cargoes, binding of a new motor to a region next to the hurdle mostly leads to the rescue of cargo out of the hurdle. However, rigid cargoes are limited by the lack of availability of motors; for example, if a rigid

cargo has only one motor in the access region, it cannot cross the roadblock. Lipid cargoes however have a much larger availability of motors because of diffusion. Hence there will be much more frequent binding of motors to the region next to hurdle. But membranes reduce force coupling between motors, and new motors that are bound to the region next to hurdles cannot always pull cargoes out of hurdles. Interestingly, simulations also show that the effect of increased availability dominates and lipid cargoes have an overall higher probability of crossing hurdles. We also develop simple analytical estimations of the probability of crossing hurdles. These estimations agree with simulations. They also allow us to predict pass probability under various values of single motor properties, cargo sizes, etc as needed for future experiments. We find that the pass probabilities of rigid cargoes are high compared to lipid cargoes in the case of a high number of initially bound motors. This is because in the case of rigid cargo with many bound motors, as the motors dissociate they can immediately rebind to microtubules. They don't diffuse away like in the case of lipid cargo.

We analyzed only hurdles of specific width $w = 16$ nm. It would be interesting to vary the width, w of the hurdle, and analyze changes in pass probabilities. We expect that lipid cargoes may be more efficient than rigid cargoes in crossing wide hurdles whose width is of the order of cargo radius, independent of the initial number of bound motors. Because on lipid cargoes, diffusion of motors on the surface, combined with the diffusion of the bead itself is expected to aid the motor in exploring wider regions on the microtubule. Hence motors on lipid cargoes have a higher chance of binding to regions next to the hurdle. Thus lipid cargoes may be more efficient than rigid cargoes when the width of the hurdle is significantly larger.

Related future works also include understanding the dynamics of cargo navigation around large roadblocks like stalled cargoes. Cargoes are found to rotate around such roadblocks. We believe addressing this question would involve significant improvements to our model specifically by incorporating a three-dimensional lattice structure into microtubules and modifying the mechanical model of the

motor. We will discuss this more in the next chapter.

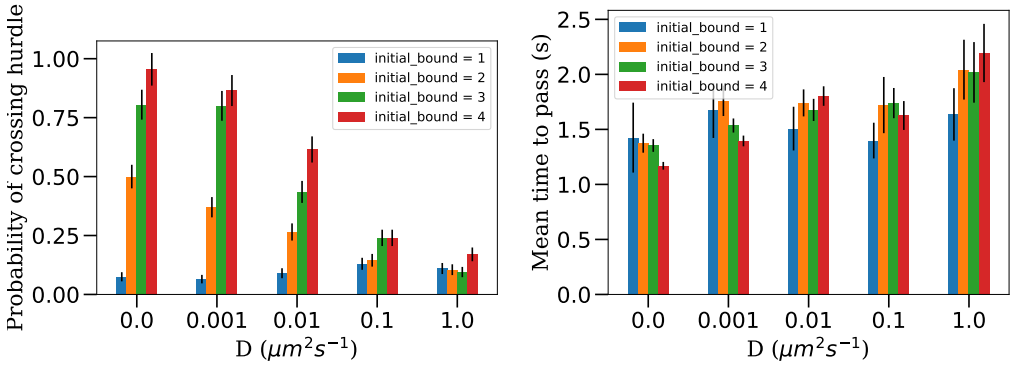

(a) N=4 High ATP (b) N=4 High ATP

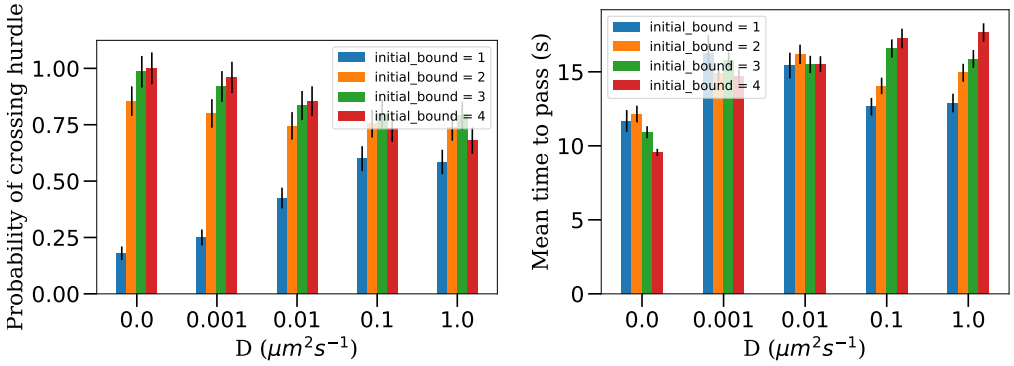

(c) N=4 Low ATP (d) N=4 Low ATP

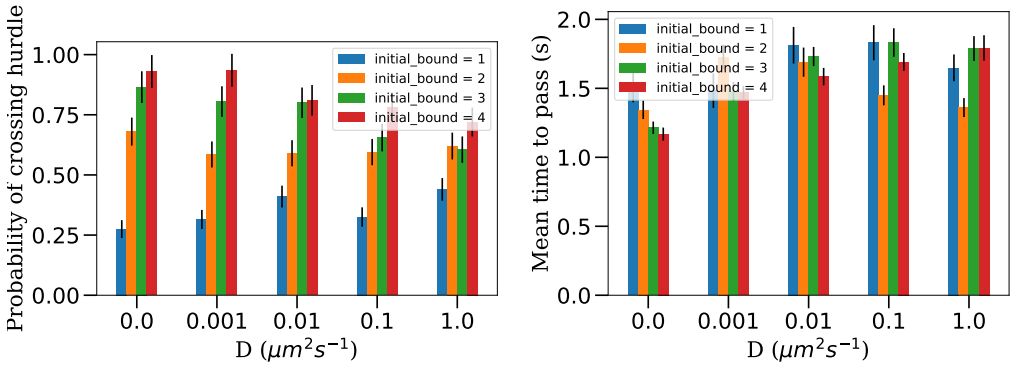

(e) N=16 High ATP (f) N=16 High ATP

Figure 5.2.7: **Pass probability and Mean Time to pass.** For three different parameter sets as a function of the initial number of bound motors (initial_bound) on the cargo and cargo surface fluidity (D). Pass probability increases with increase in D for initial_bound=1. Pass probability decreases with increase in D for initial_bound>1. Pass probability increases with increase in the number of bound motors. The hurdle of width, w=16 nm is located at x=250 nm. The center of mass of each cargo was initialized at x=0. So the hurdle is right at the edge of the cargo (cargo radius is 250 nm). cargoes are said to have passed only if their CM crosses x=500 nm which is one radius away from roadblock. 200 cargoes were considered for each case. Error bars represent the standard error of the mean.

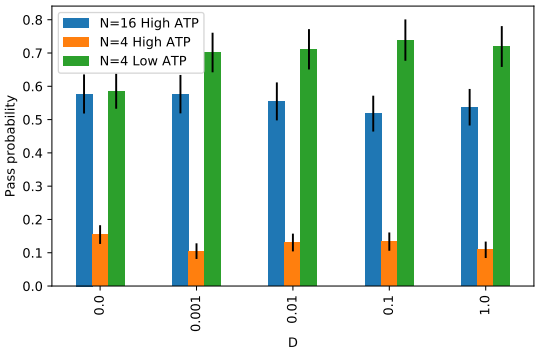

Figure 5.2.8: **Effective pass probability of cargoes increases significantly as a function of the cargo surface fluidity for multimotor transport at low [ATP].** Effective probability was calculated as an average of the pass probabilities for different number of bound motors (Fig. 5.B) weighted by the probability distributions of the number of bound motors for three-different parameter sets.

Notes

5.A Runlength decreases non-linearly as a function of roadblock probability P

We assume that the cargo stops moving the instant it encounters a roadblock. This assumption is justified from our simulation. Let P be the probability of encountering a roadblock per kinesin step (δ). Then the probability of encountering a roadblock in a small distance Δx is

$$p = \frac{P\Delta x}{\delta} \tag{5.2}$$

Probability of observing exactly n roadblocks in a distance D is

$$\mathcal{P} = \frac{\mu^n e^{-\mu}}{n!} \tag{5.3}$$

where $\mu = P\,D/\delta$. Probability of observing no roadblock in a distance D

$$\mathcal{P}_r = e^{-P\,D/\delta} \tag{5.4}$$

Probability of travelling a distance D without detaching stochastically

$$\mathcal{P}_t = e^{-k_{off}D/v} \tag{5.5}$$

Probability that the cargo travels a distance D without unbinding and without getting stuck is

$$\mathcal{P} = \mathcal{P}_r\mathcal{P}_t \tag{5.6}$$

$$\mathcal{P} = e^{-P\,D/\delta - k_{off}D/v} \tag{5.7}$$

Runlength is the mean distance travelled

$$r = \int_0^\infty D\mathcal{P}dD \tag{5.8}$$

It can be shown that

$$r = \frac{1}{(P/\delta + k_{off}/v)} \tag{5.9}$$

Thus runlength decreases non-linearly as a function of roadblock probability if we make the above assumptions.

5.B Approximate Probability of Crossing Hurdle

Let us look at the case where a cargo encounters a hurdle immediately after binding to a microtubule. The cargo is likely to have just 1 bound motor. In order for the cargo to escape the hurdle, at least 1 motor has to bind to a region on the microtubule next to the hurdle before all the microtubule-bound motors unbind.

Let us first look at the probability that a new motor binds (to some site on microtubule regardless of whether it is in front or to the back of the hurdle) before an already bound motor unbinds.

- Probability that the initially bound motor doesn't unbind upto time t is $e^{-t/\tau_{off}}$, where τ_{off} is the mean unbinding time of motor.
- Probability that a new motor doesn't bind until time t is $e^{-t/\tau_{bind}}$ where τ_{bind} is the mean time for new motor binding which we compute as $\frac{\tau_{bind}^{single}}{(N-1)}$. τ_{bind}^{single} is the mean binding time for a motor randomly placed on the cargo surface. $(N-1)$ is the number of free motors.
- Probability that a new motor binds in time $t \to t + dt$ is $\frac{dt}{\tau_{bind}}$

Therefore, the probability that the initially bound motor doesn't unbind, a new motor doesn't bind until time t but a new motor binds within $t + dt$ is

$$e^{-t/\tau_{off}} e^{-t/\tau_{bind}} \frac{dt}{\tau_{bind}} \tag{5.10}$$

Thus the total probability that a new motor binds before a current microtubule bound motor unbinds is

$$p_1 = \frac{1}{\tau_{bind}} \int_0^\infty e^{-t\left(\frac{1}{\tau_{off}}+\frac{1}{\tau_{bind}}\right)} dt \tag{5.11}$$

$$p_1 = \frac{\tau_{off}}{\tau_{bind} + \tau_{off}} \tag{5.12}$$

But the new motor can bind to region next to hurdle or region before the hurdle. We assume an equal probability for each case. If the motor binds to region next to hurdle, it escapes the trap. If it binds to region before the hurdle then the cargo remains bound to MT with two motors with the possibility of third motor binding to MT and rescuing the cargo from the hurdle.

Probability that third motor binds before two motors unbind is given by

$$p_2 = \frac{2\tau_{off}}{\tau'_{bind} + 2\tau_{off}} \tag{5.13}$$

where

$$\tau'_{bind} = \frac{\tau_{bind}^{single}}{N-2}$$

Overall probability of escape is

$$\tilde{p} = p_s\, p_1 + p_s^2\, p_2 + p_s^3\, p_3 \tag{5.14}$$

where $p_i = \frac{i \times \tau_{off}}{\frac{\tau_{bind}^{single}}{N-i} + i \times \tau_{off}}$ and p_s is the probability with which new motor binds to region in front of hurdle.

There are other possibilities like a 2-bound cargo state going back to 1-bound state and again to 2-bound state with new motor in front of hurdle. In case of N=16, higher number of bound motors are possible. But the probability of observing higher number of bound motors is small and hence we neglect these possibilities in this calculation.

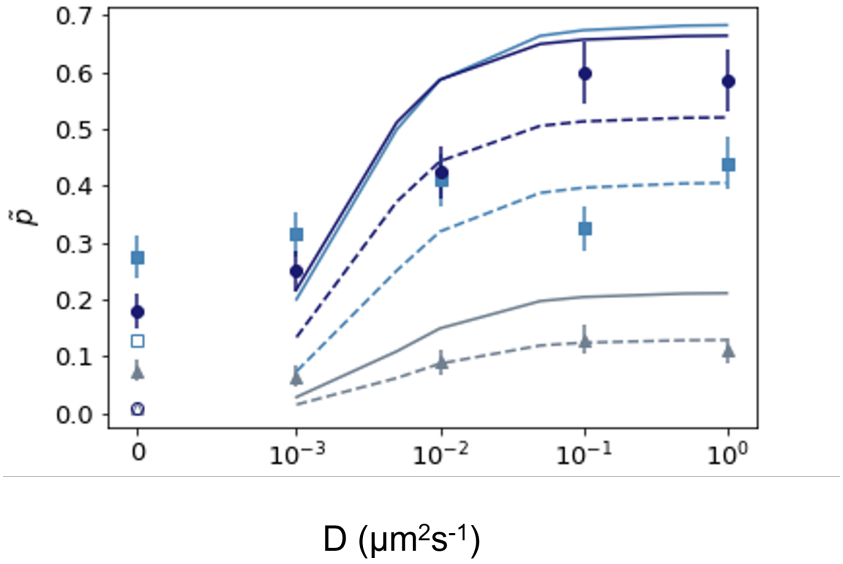

Figure 5.B.1: **Analytical estimation agrees with the measured value of pass probability.** Sold markers: Simulation values. Hollow Markers: Analytical estimation specifically for rigid cargoes taking into account the probability of different numbers of motors in the access region.Solid lines: Analytical approximation.

5.C Supplementary Figures

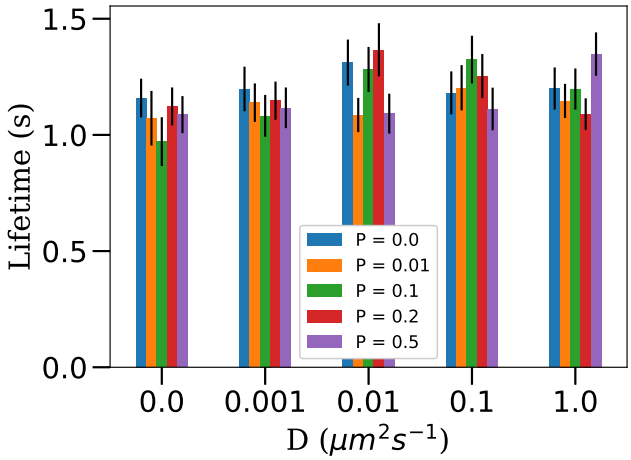

Figure 5.C.1: Mean lifetime is independent of D and P. Data was obtained from transport of cargo with 4 motors at high ATP concentration of 2 mM. 200 cargo runs were considered for calculating the mean. Error bars represent the standard error of the mean.

Chapter 6

Three-dimensional microtubule structure and motor properties

This chapter discusses further improvements to the computational model by incorporating a three-dimensional lattice structure for the microtubule and an updated mechanical model of kinesin motors. We discuss why these improvements are necessary and the preliminary results from these improvements. This is ongoing work.

6.1 Introduction

The model we developed in Chapter 2 and used so far considers the microtubule as a one-dimensional line along the x-axis. The only three-dimensional aspect of microtubule is the steric interaction between microtubule and cargo. In reality, microtubules are three-dimensional cylindrical structures made by repeating units called tubulin dimers. Each tubulin dimer comprises subunits named α and β subunits. Tubulin dimers have two kinds of interaction with each other. First, a longitudinal interaction between tubulin dimers that leads to a linear protofilament, and second, a lateral interaction that results in these protofilaments organizing into a tubular structure (See Fig. 6.1.1).

Even though microtubules have this three-dimensional structure, the questions

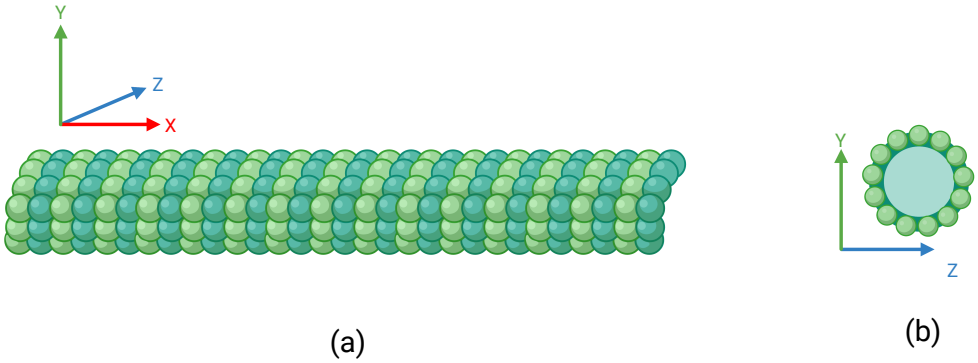

Figure 6.1.1: **Schematic of a three-dimensional microtubule lattice structure.** (a) lengthwise view and (b) cross-sectional view. This microtubule has 13 protofilaments. Created with BioRender.com

we addressed so far and the properties of motors allowed us to work with the approximation of microtubules as single lines. It is observed that kinesins track a single protofilament as they move along the microtubule [120], and there are multiple such protofilaments (typically 12-15) that cover the entire microtubule. Hence it is safe to neglect the three-dimensional lattice structure of microtubules for many problems of cargo transport, which involve small teams of motors as in most physiologically relevant examples.

However, studies have shown that this lattice structure can be important in specific scenarios, like when we analyze the accessibility of motors to microtubules [153]. It was also shown that the cylindrical surface geometry allows for a maximum number of bound motors when one considers site exclusion (that no two kinesin motors can occupy the same binding site) [153], highlighting the relevance of microtubule geometry on cargo transport. Interestingly, if we don't consider site exclusion, then the line microtubule geometry, as well as cylindrical structure, have the same number of microtubule-bound motors [153]. This confirms that our calculations of the number of bound motors in Chapter 3 will not be affected by the geometry of the microtubule since we had consistent assumptions of no site exclusion and line geometry. However, more detailed physical models of transport

call for site exclusion hence it is necessary to consider the cylindrical structure of the lattice.

Such models allow one to answer more complex questions. One such question is how teams of motors navigate around large roadblocks, and do lipid membranes help motor teams navigate better? Previous experiments observed cargoes rotate around microtubules to avoid large roadblocks [46, 49]. The mechanisms that cargoes follow in this process are not well understood, and it is not possible to answer this using models of microtubule as a one-dimensional line. Another question is how the accessibility of motors to microtubules impact their binding to microtubules. It is surprising to know that in spite of several studies on single-motor functioning, the binding rate of a motor to a microtubule is not well characterized. To characterize this process, it is important to consider a three-dimensional lattice of microtubules.

6.2 Results and Discussion

6.2.1 Implementation of 3d microtubule lattice

We consider the microtubule as a perfect cylindrical crystal with α and β subunits repeated alternatively along the x-axis [4]. It is seen that the exact structure of microtubule lattice depends on the number of protofilaments and the start of the helix. Depending on these values, the protofilaments may be straight or helical [4]. The microtubules are straight only when the number of protofilaments is 13. We estimated that even when we have higher or lower protofilaments, the helical nature of protofilaments may not impact transport since typical values of pitch lengths (distance at which the helical path of protofilament completes one revolution around cylindrical surface) are larger (6 μ m) compared to typical cargo runlength. Independent of what this pitch length is, the helical nature of protofilaments is expected to have minimal influence on relative dynamics of motors in the team.

Hence we implement the three-dimensional structure of microtubule in our model by considering a surface with 13 protofilaments that are straight and each with lattice sites 4 nm apart (that corresponds to the size of a tubulin dimer [4])

6.2.2 Dependence of on-rate with distance from microtubule is sensitive to the mechanical model of kinesin.

The process of motor binding to microtubules and how the accessibility of motor changes with on-rate is not well understood in spite of several interesting studies [45]. It was measured that the kinesin binding rate to microtubule was about 5 s^{-1} in an experiment on membrane tube extraction from lipid vesicles [88] and later computational models used these values for various geometries due to lack of newer experimental findings [45]. It is very challenging to measure on-rates in experiments. In optical trap-based experiments typically used for measuring motor properties, it is hard to identify when the motor has bound to microtubules. Only when the cargo experiences some force due to motors can one detect the motor binding. This doesn't tell how much time has elapsed since the motor was bound. Efforts have been made in this direction. For example, researchers have managed to measure the on-rate of kinesin as a function of distance from the microtubule (Prof. Steven Block Group, Private Communication). Additionally, modeling could contribute to this effort as well. In our simulations, it is straightforward to identify when the motor has bound and then connect this with macroscopic quantities easily measured in an experiment to compute on-rates.

We present preliminary studies on the dependence on on-rate as a function of distance from microtubules. Our simulations allow us to use simple assumptions about kinesin motors and predict how the on-rate depends on geometry and distance from microtubules. We hold cargo (with $N = 16$ kinesin motors) at different distances from the microtubule and measure the mean time it takes to bind to the microtubule Fig. 6.2.1. The inverse of this meantime is the on-rate of cargo to the microtubule. On-rate of individual motors is equal to the on-rate of cargoes divided by the number of motors. Kinesin motors have a specific mechanical model

that indicates the energy cost to reach a lattice site and influences the on-rate. For example, if we assume kinesin is a spring of rest length L_{mot}, then the energy cost to reach a site L distance away is $E = 1/2k_{mot}(L - L_{mot})^2$. The probability of reaching this site is proportional to the Boltzmann weight, e^{-E/k_BT}. The higher the energy cost lower is the accessibility.

The mechanical model of kinesin considered in our model described in Chapter 2 had resistance only for extension beyond rest length L_{mot} and no resistance when compressed below L_{mot}. This is the model used in most other modeling studies as well [84, 25]. Our simulations predict that the cargo binding rate to microtubule decreases monotonically with increasing distance when we assume this model of no compressive resistance. Recent studies have shown that kinesins might have a small compressive resistance that saturates at 1 pN [70]. Our simulations with this mechanical model suggest that on-rate of motors is approximately independent of the distance from microtubules upto a distance of about 30 nm from microtubule and then decays as in the previous mechanical model Fig. 6.2.1. We also verified this independence of on-rate as a function of distance near the microtubule using numerical computation of sites accessible to motors (Fig 6.2.2). We define the number of accessible sites as the cumulative sum of Boltzmann weights of all sterically accessible sites for a given model.

Our predictions of on-rate when compared with experimental data can help us identify appropriate mechanical models of kinesins for future computational studies.

6.3 Conclusions

Our previous studies, particularly cargo transport across roadblocks, highlighted the importance of having a three-dimensional microtubule structure for proper treatments of cargo transport across large roadblocks. Here we implemented a lattice structure to microtubules and also considered different models of

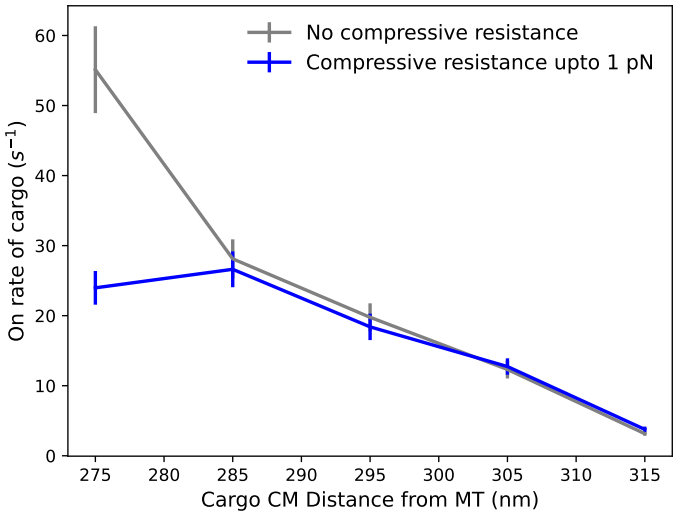

Figure 6.2.1: **On-rate of cargo held at specific distances from microtubules.** Cargo is rigid with $N = 16$ motors. The microscopic on-rate of motors was scaled up to get a shorter mean-binding time for computational convenience. Motor models used: No compressive resistance: One-sided spring that exerts resistance to extension with force constant, k_{mot}=0.32 pN/nm but no resistance to compression (grey line). Compressive force up to 1 pN: For extension, exerts a linear force with a force constant, k_{mot}=0.32 pN/nm and for compression exerts a linear force with force constant of k_{mot}=0.05 pN/nm and saturates at compressive force of 1 pN (blue line).

motors such as cable, double-sided spring, and double-sided spring with compressive resistance up to 1 pN [70]. Using simulations and numerical computations, we identified that the on-rates of motors are sensitive to the mechanical model of kinesin that we use. These on-rate results when compared with experimental data could inform the best mechanical model for future predictive models of cargo transport.

In our simulations measuring on-rate, we assumed that any sites that are sterically inaccessible to motors (defined as any sites beyond tangential planes from the motor anchor points to the microtubule surface) for computational convenience.

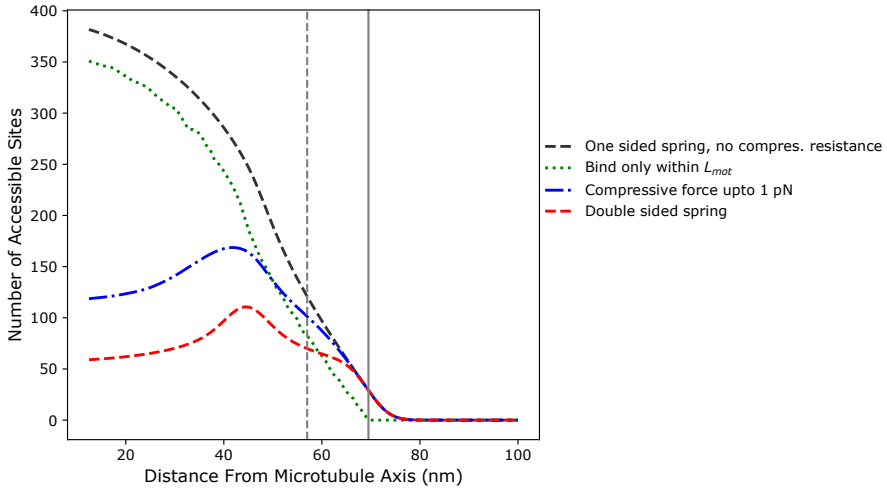

Figure 6.2.2: **The number of accessible sites defined as the number of microtubule sites weighted by Boltzmann weights based on motor's energy cost to access sites.** Data was from numerical computations, a motor was held at specific distances away from the microtubule axis, and the sum of Boltzmann weights over all lattice points was computed. Different models of motors: (a) One-sided spring: exerts resistance to extension with force constant, k_{mot}=0.32 pN/nm but no resistance to compression (brown dashed line). (b) Double-sided spring: resists both compression and extension linearly with force constant of k_{mot}=0.32 pN/nm (red dashed line), (c) Bind only within L_{mot}: No resistance to compression but also no binding to any points beyond the rest length of motor L_{mot} (green dotted line), (d) Compressive force up to 1 pN: For extension, exerts a linear force with a force constant, k_{mot}=0.32 pN/nm and for compression exerts a linear force with force constant of k_{mot}=0.05 pN/nm and saturates at compressive force of 1 pN (blue dash-dotted line).

However, this assumption is not consistent with the mechanical models of kinesins which have low or no energy cost to motor compression. Hence kinesin motor must be able to buckle and bind to regions that are behind the tangential planes. To be consistent with these mechanical models, we plan to allow motors to bind to any site on the microtubule with appropriate energy cost. However, if we allow motors to bind to regions on the other side of microtubules as shown in Fig. 6.3.1,

it is important to compute the exact force exerted by the motor on the cargo (See schematic in Fig. 6.3.1).

If we assume kinesin is a polymer with one end fixed at the microtubule as

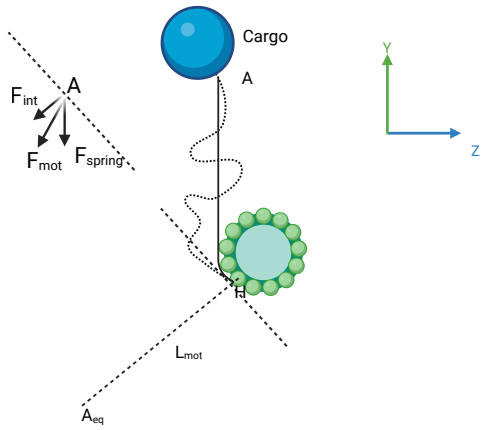

Figure 6.3.1: **Schematic of the planned motor force computations in complex binding geometries.** A is the motor anchor position on cargo. H is the head position on the microtubule. The motor linker is treated like a Gaussian chain. F_{int} is the entropic force due to the grafting of the chain to the microtubule surface. This entropic force tends to align the motor perpendicular to the surface, equilibrium position A_{eq}. F_{spring} is the spring-like force of free chain with end positions at H and A, also due to entropy. F_{mot} is the resultant motor force. Created with BioRender.com

shown in Fig. 6.3.1, then there is an entropic force that tends to align the motor perpendicular to the microtubule[18]

$$F_{int} = \frac{k_B T}{a} \exp\left(-\frac{a^2}{4R_g^2}\right) \tag{6.1}$$

where a is the monomer distance, typical value for an amino acid is 0.3 nm. R_g is the radius of gyration, $R_g = L_{mot} = 57$ nm. F_{int} at room temperature is therefore about 13.8 pN. One can show that the time it takes for cargo to rotate by 90^o around the microtubule with this force is just about 100 μs (See Appendix 6.A) which is fast compared to the typical lifetime of cargo (about 1 s). Hence one cannot neglect this force in our simulations. Hence we plan to take this force F_{int}

also into the motor dynamics in our future simulations.

With all these improvements, we plan to make more careful predictions of on-rate as a function of distance from microtubules. We would also like to analyze the effect of different mechanical models of kinesins on the run length and collective force generated by motor teams. Finally, we would like to use our improved model of cargo transport with three-dimensional microtubule lattice and updated mechanical models of kinesins to investigate the effect of membranes on cargo navigation across large roadblocks.

Notes

6.A Time taken for cargo to rotate by 90^o around microtubule due to entropic force of motor.

The velocity of motor anchor position is

$$\frac{d\vec{A}_i}{dt} = \frac{\vec{F}_{mot}}{\gamma} \tag{6.2}$$

γ is the friction coefficient. This is dominated by the friction coefficient of cargo, $\gamma = \gamma_c = 18\pi\eta r$. The angular velocity of motor about grafted point on microtubule,

$$R_g \frac{dA_\theta}{dt} = \frac{F_{int}}{\gamma} \tag{6.3}$$

We assume there is only $F_{int} = 13.8$ pN in this direction. When we substitute typical values in our simulation (Chapter 2, and $R_g = L_{mot} = 57$ nm, the time taken by the motor to rotate by 90^o comes out to be about 100 μs.

Chapter 7

Conclusion and Future Directions

Molecular motors are essential components of Eukaryotic cells that are involved in the transport of cargo like mRNA, mitochondria, chromosome separation during cell division, cell migration, etc. In this dissertation, we studied the cooperativity between multiple molecular motors and how that is influenced by fluidities of cargo surface. This has relevance *in vivo* since most intracellular cargoes are bound by lipid bilayers. The motivation for this investigation was the observation that even though molecular motors work together well in cells, they don't work well when coupled rigidly in *in vitro* experiments. We investigated physical mechanisms that could help increase motor cooperativity in cells and also addressed broader questions on cargo transport by teams of motors under various complex physiological conditions. We used a Brownian dynamics model to answer these questions.

We consider cargo as a sphere and explicitly simulate the motion of motor anchor positions by allowing free diffusion for unbound motors and diffusion biased by exerted forces for bound motors. The diffusion constant for this motion is determined by the cargo surface fluidity. We also accounted for the force and ATP dependence of the bound motor's off-rate and stepping rate. The spherical cargo's position was then updated by an overdamped Langevin equation depending on the net force exerted by all bound motors.

Next, applied the computational model to understand cargo transport by teams

of identical molecular motors and the effect of lipid membrane coupling on them. We found that surface fluidity leads to the reduction in negative mechanical interference between kinesins, as quantified by lower forces on individual motors and a significant drop in antagonistic forces between motors. This allows teams of fluid-coupled motors to exploit load sharing without inter-motor interference. This decreases single motor off-rates and increases processivity. Our simulations also showed that the fluid surface allows for the clustering of motors at a well-defined location on the surface relative to the microtubule and that the fluid-coupled motors can exert more collective force per motor against loads. Interestingly, increasing the number of bound motors pulls the cargo closer to the microtubule, increasing the on-rates of unbound motors, and resulting in a cooperative increase in bound motor numbers for lipid cargoes. Taken together, these effects can cooperatively result in increased processivity and collective mechanical force production against load with an increase in fluidity for teams of molecular motors. This has both biological and technological implications.

Previous experimental observations [94, 113] showed that membrane-bound cargoes (or lipid cargoes) have higher velocity than membrane-free cargoes when carried by teams of molecular motors. Even though a couple of mechanisms were proposed to explain this higher velocity of lipid cargoes, a clear quantitative explanation of the mechanisms was lacking. In this study, we show using a computational model that underlying heterogeneities in single motor velocities are crucial to observe higher velocities of lipid cargoes. When motors have different velocities, they develop tension between them as they walk along microtubules reducing the velocity of the team. If the motors are coupled to the membrane, the rate of this strain buildup is slower resulting in higher velocity. Additionally, heterogeneity in velocity increases cargo run length in both rigid and lipid cargoes. Interestingly, we find that the run length of lipid cargoes increases more than the rigid cargoes with an increase in the fraction of slow motors. Thus lipid cargoes can traverse a given distance with a lower fraction of slower motors or higher overall cargo velocity. We also estimated the runlength of cargoes with a modified version of

previously established analytical equation [76, 125]. This analytical model seemed to adequately predict the runlengths of rigid and lipid cargoes allowing us to extend the predictions to various other parameter regimes in future studies. Overall, our work elucidates the emergence of cooperativity between heterogeneous teams of motors in cells because of purely physical mechanisms arising from how they are coupled together. We also illustrate that the degree of heterogeneity can be used as a tunability parameter to achieve desired runlength and velocity. These predictions need to be verified with experiments of membrane-bound cargo transport by teams of motors with varying levels of heterogeneity.

We then focused on understanding cargo transport across single tubulin dimer and larger ring-like roadblocks on microtubules. We discovered that lipid membranes increase the likelihood of passing hurdles when cargoes with single microtubule-bound motors approach them. Lipid and rigid cargoes employ distinct mechanisms to cross hurdles. New motor binding in rigid cargoes often results in passing the hurdle but rigid cargos suffer from limited motor availability. In contrast, lipid cargoes have a larger motor availability due to diffusion, leading to more frequent motor binding near hurdles. Despite membranes reducing force coupling, increased availability means lipid cargoes have a higher overall probability of passing hurdles. Our analytical estimations of pass probabilities align with simulations and allow for predictions under various conditions. We noted cargoes with lower surface fluidity with many bound motors have higher pass probabilities than cargos with high surface fluidity due to immediate rebind capability after detachment. This could be used as a sorting or filtering mechanism in cells. These results could inform research into breakdowns in transport in various pathologies.

We then improved the computational model by incorporating advanced mechanical models of motors and a three-dimensional lattice structure for microtubules. Using simulations and numerical computations, we identified that the on-rates of motors are sensitive to the mechanical model of kinesin that we use.

Future directions

Our results on the transport properties of fluid cargo over a wide range of surface fluidity, ATP concentration, motor number, and cargo size offer quantitative guidelines for the design of artificial cargo driven by kinesin teams. In this dissertation, we used parameters for kinesin motors to generate the results, but they can be generalized to other systems with different geometries of cargos with different motors coupled by a fluid surface with simple modifications and parameter tuning. Thus one could address different questions on cargo transport with this model.

For example, in the case of cargo transport by heterogeneous teams of motors, the central assumption in our model was that the detachment rates of motors decrease with a decrease in motor velocities. We assumed that all the motors are kinesin-I motors, and the rate of the detachment of motors from microtubules is expected to be directly proportional to the velocity of motors. However, cellular cargoes can have motors teams that are made up of different motor types. We can make simple modifications to motor properties in simulations and explore how such heterogeneities impact transport by teams of motors. A more detailed study of cargo transport by teams of motors with different complexity, such as mixtures of different types of kinesins, kinesin, myosin, and dynein together and other heterogeneities, will help discover the functional relevance of all these heterogeneities in cell and could unveil novel regulatory mechanisms for cargo transport in cell.

Another important future direction is understanding the effect of lipid membranes on cargo transport across large roadblocks like stalled cargo. What mechanisms do teams of motors employ to navigate around large roadblocks? Is it because motors side step and rotate the cargo or because motors unbind and new motors bind to neighboring protofilaments effectively rotating the cargo?

It would also be interesting to explore the interaction of motor teams with microtubules at intersections between microtubules. It is not clear how lipid membranes could influence the probability of cargo switching at intersections. We are

also curious to know how the discontinuous nature of the cytoplasm impact transport, and how we can update the model to take into account the viscoelastic nature of the cytoplasm.

This and similar computational models could complement experiments for a more comprehensive analysis of data. This model could complement ongoing experimental studies on membrane-bound cargo transport on single and network of filaments. It is exciting to note that this modeling approach could be used to understand how molecular motor-based transport impacts fission and fusion processes between mitochondria, (and other organelles) which are crucial to maintaining proper neuronal functioning.

Bibliography

[1] The Feynman Lectures on Physics Vol. I Ch. 46: Ratchet and pawl.

[2] Coordination of kinesin motors pulling on fluid membranes. *Biophysical Journal*, 94(12):5009–5017, 2008.

[3] Shabeen Ally, Adam G Larson, Kari Barlan, Sarah E Rice, and Vladimir I Gelfand. Opposite-polarity motors activate one another to trigger cargo transport in live cells. *J. Cell Biol.*, 187(7):1071–82, dec 2009.

[4] Linda A Amos and Keiko Hirose. Studying the structure of microtubules by electron microscopy. *Microtubule Protocols*, pages 65–91, 2007.

[5] D. Ando, M.K. Mattson, J. Xu, and A. Gopinathan. Cooperative protofilament switching emerges from inter-motor interference in multiple-motor transport. *Sci. Rep.*, 4:7255, 2014.

[6] David Ando, Michelle K. Mattson, Jing Xu, and Ajay Gopinathan. Cooperative protofilament switching emerges from inter-motor interference in multiple-motor transport. *Scientific Reports*, 4(1):1–8, 12 2014.

[7] Johan O. L. Andreasson, Bojan Milic, Geng-Yuan Chen, Nicholas R. Guydosh, William O. Hancock, and Steven M. Block. Examining kinesin processivity within a general gating framework. *eLife*, 4, 2015.

[8] Johan Oscar Lennart Andreasson. *Single-Molecule Biophysics of Kinesin Family Motor Proteins*. PhD thesis, Stanford University, Stanford,CA, 2013.

[9] Goker Arpag, Shankar Shastry, William O. Hancock, and Erkan Tüzel. Transport by populations of fast and slow kinesins uncovers novel family-dependent motor characteristics important for in vivo function. *Biophysical Journal*, 107(8):1896–1904, 2014.

[10] Goker Arpag, Shankar Shastry, William O. Hancock, and Erkan Tüzel. Transport by populations of fast and slow kinesins uncovers novel family-dependent motor characteristics important for in vivo function. *Biophys. J.*, 107(8):1896–1904, 2014.

[11] A. Ashkin, Karin Schütze, J. M. Dziedzic, Ursula Euteneuer, and Manfred Schliwa. Force generation of organelle transport measured in vivo by an infrared laser trap. *Nature*, 348(6299):346–348, 1990.

[12] Daniel S. Banks and Cécile Fradin. Anomalous diffusion of proteins due to molecular crowding. *Biophysical Journal*, 89(5):2960–2971, 11 2005.

[13] Kari Barlan, Molly J Rossow, and Vladimir I Gelfand. The journey of the organelle: teamwork and regulation in intracellular transport. *Curr. Opin. Cell Biol.*, 25(4):483–488, 2013. Cell organelles.

[14] J. Beeg, S. Klumpp, R. Dimova, R. S.Garcia, and E. Unger. Transport of beads by several kinesin motors. *Biophys. J.*, 94(2):532–541, 2008.

[15] George I. Bell. Models for the specific adhesion of cells to cells. *Science*, 200(4342):618–627, May 1978.

[16] Florian Berger, Corina Keller, Stefan Klumpp, and Reinhard Lipowsky. Distinct transport regimes for two elastically coupled molecular motors. *Phys. Rev. Lett.*, 108:208101, May 2012.

[17] Jared P. Bergman, Matthew J. Bovyn, Florence F. Doval, Abhimanyu Sharma, Manasa V. Gudheti, Steven P. Gross, Jun F. Allard, and Michael D. Vershinin. Cargo navigation across 3d microtubule intersections. *Proc. Natl. Acad. Sci. U.S.A.*, 115(3):537–542, 2018.

[18] Thomas Bickel, C Jeppesen, and CM Marques. Local entropic effects of polymers grafted to soft interfaces. *The European Physical Journal E*, 4:33–43, 2001.

[19] R Byron Bird, Warren E Stewart, and Edwin N Lightfoot. *Transport Phenomena*. John Wiley & Sons, Chichester, England, November 2006.

[20] S. M. Block, C. L. Asbury, J. W. Shaevitz, and M. J. Lang. Probing the kinesin reaction cycle with a 2D optical force clamp. *Proc. Natl. Acad. Sci. U.S.A.*, 100(5):2351–2356, 2003.

[21] S. M. Block and M. J. Schnitzer. Kinesin hydrolyses one ATP per 8-nm step. *Nature*, 388(6640):386–390, 1997.

[22] Steven M. Block. Kinesin motor mechanics: Binding, stepping, tracking, gating, and limping. *Biophys. J.*, 92(9):2986–2995, May 2007.

[23] Sebastin Bouzat and Fernando Falo. Tug of war of molecular motors: The effects of uneven load sharing. *Phys. Biol.*, 8(6), 12 2011.

[24] Sebastián Bouzat and Fernando Falo. The influence of direct motor-motor interaction in models for cargo transport by a single team of motors. *Phys. Biol.*, 7(4), 2010.

[25] Matthew Bovyn, Babu Reddy Janakaloti Narayanareddy, Steven Gross, and Jun Allard. Diffusion of kinesin motors on cargo can enhance binding and run lengths during intracellular transport. *Mol. Biol. Cell.*, 32(9):984–994, 2021. PMID: 33439674.

[26] John T Canty, Ruensern Tan, Emre Kusakci, Jonathan Fernandes, and Ahmet Yildiz. Structure and mechanics of dynein motors. *Annual review of biophysics*, 50:549–574, 2021.

[27] N. J. Carter and R. A. Cross. Mechanics of the kinesin step. *Nature*, 435(7040):308–312, 2005.

[28] Kejie Chen, Woochul Nam, and Bogdan I. Epureanu. Effects of neighboring microtubules on the microscopic dynamics of kinesin transport. *Phys. Rev. E*, 98:052412, Nov 2018.

[29] Kejie Chen, Woochul Nam, and Bogdan I. Epureanu. Collective intracellular cargo transport by multiple kinesins on multiple microtubules. *Phys. Rev. E*, 101:052413, May 2020.

[30] Xuequn Chen and John A. Williams. Exocytosis. In *Encyclopedia of Gastroenterology*. 2004.

[31] Erica Chevalier-Larsen and Erika L.F. Holzbaur. Axonal transport and neurodegenerative disease. *Biochim. Biophys. Acta Mol. Basis Dis.*, 1762(11):1094 – 1108, 2006. Molecular Basis of Amyotrophic Lateral Sclerosis.

[32] Praveen D. Chowdary, Luke Kaplan, Daphne L. Che, and Bianxiao Cui. Dynamic clustering of dyneins on axonal endosomes: Evidence from high-speed darkfield imaging. *Biophysical Journal*, 115(2):230–241, July 2018.

[33] C M Coppin, J T Finer, J A Spudich, and R D Vale. Detection of sub-8-nm movements of kinesin by high-resolution optical-trap microscopy. *Proc. Natl. Acad. Sci. U.S.A.*, 93(5):1913–1917, 1996.

[34] Chris M. Coppin, Daniel W. Pierce, Long Hsu, and Ronald D. Vale. The load dependence of kinesin's mechanical cycle. *Proc. Natl. Acad. Sci. U.S.A.*, 94(16):8539–8544, 1997.

[35] David L. Coy, Michael Wagenbach, and Jonathon Howard. Kinesin takes one 8-nm step for each ATP that it hydrolyzes. *J. Biol. Chem.*, 274(6):3667–3671, 1999.

[36] Robert A Cross. Intracellular Transport. In *eLS*. John Wiley and Sons, Ltd, 2006.

[37] Imre Derényi, Frank Jülicher, and Jacques Prost. Formation and interaction of membrane tubes. *Phys. Rev. Lett.*, 88:238101, May 2002.

[38] Markus Deserno. Elastic deformation of a fluid membrane upon colloid binding. *Phys. Rev. E*, 69:031903, Mar 2004.

[39] Kerstin Dreblow, Nikolina Kalchishkova, and Konrad J. Böhm. Kinesin passing permanent blockages along its protofilament track. *Biochemical and Biophysical Research Communications*, 395(4):490–495, 2010.

[40] Jonathan W. Driver, Arthur R. Rogers, D. Kenneth Jamison, Rahul K. Das, Anatoly B. Kolomeisky, and Michael R. Diehl. Coupling between motor proteins determines dynamic behaviors of motor protein assemblies. *Phys. Chem. Chem. Phys.*, 12(35):10398, aug 2010.

[41] Artem K. Efremov, Anand Radhakrishnan, David S. Tsao, Carol S. Bookwalter, Kathleen M. Trybus, and Michael R. Diehl. Delineating cooperative responses of processive motors in living cells. *Proc. Natl. Acad. Sci. U.S.A.*, 111(3):E334–E343, 2014.

[42] R. John Ellis. Macromolecular crowding: Obvious but underappreciated. *Trends in Biochemical Sciences*, 26(10):597–604, 10 2001.

[43] Robert P. Erickson, Zhiyuan Jia, Steven P. Gross, and Clare C. Yu. How molecular motors are arranged on a cargo is important for vesicular transport. *PLoS Comput. Biol.*, 7(5):e1002032, 2011.

[44] E. Evans and K. Ritchie. Dynamic strength of molecular adhesion bonds. *Biophysical Journal*, 72(4):1541–1555, April 1997.

[45] Qingzhou Feng, Keith J Mickolajczyk, Geng-Yuan Chen, and William O Hancock. Motor reattachment kinetics play a dominant role in multimotor-driven cargo transport. *Biophysical journal*, 114(2):400–409, 2018.

[46] Luke S Ferro, Sinan Can, Meghan A Turner, Mohamed M ElShenawy, and Ahmet Yildiz. Kinesin and dynein use distinct mechanisms to bypass obstacles. *eLife*, 8:e48629, sep 2019.

[47] Ken'ya Furuta, Akane Furuta, Yoko Y. Toyoshima, Misako Amino, Kazuhiro Oiwa, and Hiroaki Kojima. Measuring collective transport by defined numbers of processive and nonprocessive kinesin motors. *Proceedings of the National Academy of Sciences*, 110(2):501–506, 2013.

[48] Yuan Gao, Stephen M. Anthony, Yanqi Yu, Yi Yi, and Yan Yu. Cargos rotate at microtubule intersections during intracellular trafficking. *Biophysical Journal*, 114(12):2900–2909, 2018.

[49] Yuan Gao, Stephen M Anthony, Yanqi Yu, Yi Yi, and Yan Yu. Cargos rotate at microtubule intersections during intracellular trafficking. *Biophysical journal*, 114(12):2900–2909, 2018.

[50] Ido Golding and Edward C. Cox. Physical nature of bacterial cytoplasm. *Physical Review Letters*, 96(9):098102, 3 2006.

[51] Raymond E. Goldstein and Jan Willem van de Meent. A physical perspective on cytoplasmic streaming. *Interface Focus*, 5(4), 5 2015.

[52] Michael W. Gramlich, Leslie Conway, Winnie H. Liang, Joelle A. Labastide, Stephen J. King, Jing Xu, and Jennifer L. Ross. Single molecule investigation of kinesin-1 motility using engineered microtubule defects. *Scientific Reports*, 7(1):1–12, 3 2017.

[53] Steven P. Gross, Michael A. Welte, Steven M. Block, and Eric F. Wieschaus. Coordination of opposite-polarity microtubule motors. *Journal of Cell Biology*, 156(4):715–724, 2 2002.

[54] Rahul Grover, Janine Fischer, Friedrich W. Schwarz, Wilhelm J. Walter, Petra Schwille, and Stefan Diez. Transport efficiency of membrane-anchored kinesin-1 motors depends on motor density and diffusivity. *Proceedings of the National Academy of Sciences*, 113(46):E7185–E7193, 2016.

[55] Rahul Grover, Janine Fischer, Friedrich W Schwarz, Wilhelm J Walter, Petra Schwille, and Stefan Diez. Transport efficiency of membrane-anchored kinesin-1 motors depends on motor density and diffusivity. *Proc. Natl. Acad. Sci. U.S.A.*, 113(46):E7185–E7193, nov 2016.

[56] I. Grundke-Iqbal, K. Iqbal, Y. C. Tung, M. Quinlan, H. M. Wisniewski, and L. I. Binder. Abnormal phosphorylation of the microtubule-associated protein tau (tau) in Alzheimer cytoskeletal pathology. *Proc. Natl. Acad. Sci. U.S.A.*, 83(13):4913–4917, 7 1986.

[57] Braulio Gutiérrez-Medina, Adrian N. Fehr, and Steven M. Block. Direct measurements of kinesin torsional properties reveal flexible domains and occasional stalk reversals during stepping. *Proc. Natl. Acad. Sci. U. S. A.*, 106(40):17007–17012, 2009.

[58] Braulio Gutiérrez-Medina, Adrian N. Fehr, and Steven M. Block. Direct measurements of kinesin torsional properties reveal flexible domains and occasional stalk reversals during stepping. *Proc. Natl. Acad. Sci. U. S. A.*, 106(40):17007–17012, 2009.

[59] William O. Hancock. Bidirectional cargo transport: moving beyond tug of war. *Nature Reviews Molecular Cell Biology*, 15(9):615–628, August 2014.

[60] D. B. Hill, M. J. Plaza, K. Bonin, and G. Holzwarth. Fast vesicle transport in PC12 neurites: Velocities and forces. *European Biophysics Journal*, 33(7):623–632, 11 2004.

[61] Nobutaka Hirokawa. Kinesin and dynein superfamily proteins and the mechanism of organelle transport. *Science*, 279(5350):519–526, 1 1998.

[62] Erika LF Holzbaur and Yale E Goldman. Coordination of molecular motors: from in vitro assays to intracellular dynamics. *Curr. Opin. Cell Biol.*, 22(1):4–13, feb 2010.

[63] J. Howard. *Mechanics of motor proteins and the cytoskeleton*. Sinauer Associates (OUP), 2001.

[64] Jonathon Howard. *Mechanics of Motor Proteins and the Cytoskeleton*. Sinauer, Sunderland, MA, 2001.

[65] Jiliang Hu, Somaye Jafari, Yulong Han, Alan J. Grodzinsky, Shengqiang Cai, and Ming Guo. Size- and speed-dependent mechanical behavior in living mammalian cytoplasm. *Proceedings of the National Academy of Sciences*, 114(36):9529–9534, August 2017.

[66] K.C. Huang, C. Vega, and A. Gopinathan. Conformational changes, diffusion and collective behavior in monomeric kinesin-based motility. *J. Phys. Condens. Matter*, 23(37):374106, 2011.

[67] Gary L. Hunter, Kazem V. Edmond, Mark T. Elsesser, and Eric R. Weeks. Tracking rotational diffusion of colloidal clusters. *Optics Express*, 19(18):17189, August 2011.

[68] K. Iqbal, F. Liu, C.-X. Gong, and I. Grundke-Iqbal. Tau in Alzheimer Disease and Related Tauopathies. *Curr. Alzheimer Res.*, 7(8):656–664, 12 2010.

[69] D. Kenneth Jamison, Jonathan W. Driver, Arthur R. Rogers, Pamela E. Constantinou, and Michael R. Diehl. Two kinesins transport cargo primarily via the action of one motor: Implications for intracellular transport. *Biophys. J.*, 99(9):2967–2977, 2010.

[70] Sylvia Jeney, Ernst H. K. Stelzer, Helmut Grubmüller, and Ernst-Ludwig Florin. Mechanical properties of single motor molecules studied by three-dimensional thermal force probing in optical tweezers. *ChemPhysChem*, 5(8):1150–1158, 2004.

[71] Rui Jiang, Steven Vandal, SooHyun Park, Sheereen Majd, Erkan Tüzel, and William O. Hancock. Microtubule binding kinetics of membrane-bound kinesin-1 predicts high motor copy numbers on intracellular cargo. *Proc. Nat. Acad. Sci. U.S.A.*, 116(52):26564–26570, 2019.

[72] Ryan P Joyner, Jeffrey H Tang, Jonne Helenius, Elisa Dultz, Christiane Brune, Liam J Holt, Sebastien Huet, Daniel J Müller, and Karsten Weis. A glucose-starvation response regulates the diffusion of macromolecules. *eLife*, 5:e09376, mar 2016.

[73] Colin James Stockdale Klaus, Krishnan Raghunathan, Emmanuele DiBenedetto, and Anne K. Kenworthy. Analysis of diffusion in curved surfaces and its application to tubular membranes. *Mol. Biol. Cell*, 27(24):3937–3946, 2016. PMID: 27733625.

[74] Peter E. Kloeden, Eckhard Platen, and Peter E. Kloeden. *Numerical solution of stochastic differential equations*. Springer Berlin / Heidelberg, 2011.

[75] Dieter R. Klopfenstein, Michio Tomishige, Nico Stuurman, and Ronald D. Vale. Role of phosphatidylinositol(4, 5)bisphosphate organization in membrane transport by the unc104 kinesin motor. *Cell*, 109(3):347–358, May 2002.

[76] S. Klumpp and R. Lipowsky. Cooperative cargo transport by several molecular motors. *Proc. Natl. Acad. Sci. U.S.A.*, 102(48):17284–17289, 2005.

[77] S. Klumpp, T. M. Nieuwenhuizen, and R. Lipowsky. Movements of molecular motors: ratchets, random walks and traffic phenomena. *Physica E*, 29(1–2):380–389, 2005.

[78] Stefan Klumpp and Reinhard Lipowsky. Cooperative cargo transport by several molecular motors. *Proceedings of the National Academy of Sciences of the United States of America*, 102(48):17284–17289, 11 2005.

[79] Stefan Klumpp and Reinhard Lipowsky. Cooperative cargo transport by several molecular motors. *Proceedings of the National Academy of Sciences*, 102(48):17284–17289, 2005.

[80] Till Korten and Stefan Diez. Setting up roadblocks for kinesin-1: mechanism for the selective speed control of cargo carrying microtubules. *Lab Chip*, 8:1441–1447, 2008.

[81] H A Kramers. Brownian motion in a field of force and the diffusion model of chemical reactions. *Physica*, 7(4):284–304, 1940.

[82] Ambarish Kunwar and Alexander Mogilner. Robust transport by multiple motors with nonlinear force– velocity relations and stochastic load sharing. *Phys. Biol.*, 7(1):16012, 2010.

[83] Ambarish Kunwar, Suvranta K. Tripathy, Jing Xu, Michelle K. Mattson, Preetha Anand, Roby Sigua, Michael Vershinin, Richard J. McKenney, Clare C. Yu, Alexander Mogilner, and Steven P. Gross. Mechanical stochastic tug-of-war models cannot explain bidirectional lipid-droplet transport. *Proc. Natl. Acad. Sci. U.S.A.*, 108(47):18960–18965, 2011.

[84] Ambarish Kunwar, Michael Vershinin, Jing Xu, and Steven P. Gross. Stepping, Strain Gating, and an Unexpected Force-Velocity Curve for Multiple-Motor-Based Transport. *Curr. Biol.*, 18(16):1173–1183, 8 2008.

[85] Comert Kural, Hwajin Kim, Sheyum Syed, Gohta Goshima, Vladimir I. Gelfand, and Paul R. Selvin. Cell Biology: Kinesin and dynein move a peroxisome in vivo: A tug-of-war or coordinated movement? *Science*, 308(5727):1469–1472, 6 2005.

[86] Melike Lakadamyali. Navigating the cell: how motors overcome roadblocks and traffic jams to efficiently transport cargo. *Phys Chem Chem Phys*, 16:5907, 2014.

[87] G. M. Langford. Actin- and microtubule-dependent organelle motors: interrelationships between the two motility systems. *Curr. Opin. Cell. Biol.*, 7(1):82–88, 1995.

[88] C. Leduc, O. Campàs, K.B. Zeldovich, A. Roux, P. Jolimaitre, L. Bourel-Bonnet, B. Goud, J.-F. Joanny, P. Bassereau, and J. Prost. Cooperative extraction of membrane nanotubes by molecular motors. *Proc. Natl. Acad. Sci. U.S.A.*, 101(49):17096–17101, 2004.

[89] Cécile Leduc, Otger Campàs, Konstantin B. Zeldovich, Aurélien Roux, Pascale Jolimaitre, Line Bourel-Bonnet, Bruno Goud, Jean-François Joanny, Patricia Bassereau, and Jacques Prost. Cooperative extraction of membrane nanotubes by molecular motors. *Proc. Natl. Acad. Sci. U.S.A.*, 101(49):17096–17101, 2004.

[90] Christina Leidel, Rafael A. Longoria, Franciso Marquez Gutierrez, and George T. Shubeita. Measuring molecular motor forces in vivo: Implications for tug-of-war models of bidirectional transport. *Biophysical Journal*, 103(3):492–500, August 2012.

[91] Valeria Levi, Anna S. Serpinskaya, Enrico Gratton, and Vladimir Gelfand. Organelle transport along microtubules in xenopus melanophores: Evidence for cooperation between multiple motors. *Biophysical Journal*, 90(1):318–327, 2006.

[92] Qiaochu Li, James T Ferrare, Jonathan Silver, John O Wilson, Luis Arteaga-Castaneda, Weihong Qiu, Michael Vershinin, Stephen J King, Keir C Neuman, and Jing Xu. Cholesterol in the cargo membrane amplifies tau inhibition of kinesin-1-based transport. *Proceedings of the National Academy of Sciences*, 120(3):e2212507120, 2023.

[93] Qiaochu Li, Stephen J. King, Ajay Gopinathan, and Jing Xu. Quantitative Determination of the Probability of Multiple-Motor Transport in Bead-Based Assays. *Biophys. J.*, 110(12):2720–2728, 2016.

[94] Qiaochu Li, Kuo-Fu Tseng, Stephen J. King, Weihong Qiu, and Jing Xu. A fluid membrane enhances the velocity of cargo transport by small teams of kinesin-1. *J. Chem. Phys.*, 148(12):123318, mar 2018.

[95] Winnie H. Liang, Qiaochu Li, K.M. Rifat Faysal, Stephen J. King, Ajay Gopinathan, and Jing Xu. Microtubule defects influence kinesin-based transport in vitro. *Biophysical Journal*, 110(10):2229–2240, 2016.

[96] Kathryn L Lipson, Sonya G Fonseca, Shinsuke Ishigaki, Linh X Nguyen, Elizabeth Foss, Rita Bortell, Aldo A Rossini, and Fumihiko Urano. Regulation of insulin biosynthesis in pancreatic beta cells by an endoplasmic reticulum-resident protein kinase ire1. *Cell metabolism*, 4(3):245–254, 2006.

[97] Andrew T. Lombardo, Shane R. Nelson, M. Yusuf Ali, Guy G. Kennedy, Kathleen M. Trybus, Sam Walcott, and David M. Warshaw. Myosin va molecular motors manoeuvre liposome cargo through suspended actin filament intersections in vitro. *Nature Communications*, 8(1), June 2017.

[98] Joseph Lopes, David A. Quint, Dail E. Chapman, Melissa Xu, Ajay Gopinathan, and Linda S. Hirst. Membrane mediated motor kinetics in microtubule gliding assays. *Sci. Rep.*, 9(1), July 2019.

[99] K. Luby-Phelps, P. E. Castle, D. L. Taylor, and F. Lanni. Hindered diffusion of inert tracer particles in the cytoplasm of mouse 3T3 cells. *Proceedings of the National Academy of Sciences of the United States of America*, 84(14):4910–4913, 7 1987.

[100] K. Luby-Phelps, D. L. Taylor, and F. Lanni. Probing the structure of cytoplasm. *Journal of Cell Biology*, 102(6):2015–2022, 6 1986.

[101] Katherine Luby-Phelps. Cytoarchitecture and physical properties of cytoplasm: Volume, viscosity, diffusion, intracellular surface area. *International Review of Cytology*, 192:189–221, 1 1999.

[102] Katherine Luby-Phelps. Cytoarchitecture and physical properties of cytoplasm: Volume, viscosity, diffusion, intracellular surface area. In Harry Walter, Donald E. Brooks, and Paul A. Srere, editors, *Microcompartmentation*

and Phase Separation in Cytoplasm, volume 192 of *International Review of Cytology*, pages 189–221. Academic Press, 1999.

[103] Sandra Maday, Alison E. Twelvetrees, Armen J. Moughamian, and Erika L.F. Holzbaur. Axonal transport: Cargo-specific mechanisms of motility and regulation. *Neuron*, 84(2):292–309, 2014.

[104] R. Mallik and S. P. Gross. Molecular motors: strategies to get along. *Curr. Biol.*, 14(22):R971–R982, 2004.

[105] R. Tyler McLaughlin, Michael R. Diehl, and Anatoly B. Kolomeisky. Collective dynamics of processive cytoskeletal motors. *Soft Matter*, 12(1):14–21, dec 2016.

[106] Fereshteh L. Memarian, Joseph D. Lopes, Fabian Jan Schwarzendahl, Madhuvanthi Guruprasad Athani, Niranjan Sarpangala, Ajay Gopinathan, Daniel A. Beller, Kinjal Dasbiswas, and Linda S. Hirst. Active nematic order and dynamic lane formation of microtubules driven by membrane-bound diffusing motors. *Proceedings of the National Academy of Sciences*, 118(52), 2021.

[107] Stéphanie Millecamps and Jean-Pierre Julien. Axonal transport deficits and neurodegenerative diseases. *Nature Reviews Neuroscience*, 14(3):161–176, 2013.

[108] Stéphanie Millecamps and Jean-Pierre Julien. Axonal transport deficits and neurodegenerative diseases. *Nat. Rev. Neurosci.*, 14(3):161–176, January 2013.

[109] Robert H. Miller and Raymond I. Lasek. Cross-bridges mediate anterograde and retrograde vesicle transport along microtubules in squid axoplasm. *Journal of Cell Biology*, 101(6):2181–2193, 12 1985.

[110] Saurabh S Mogre, Aidan I Brown, and Elena F Koslover. Getting around the cell: physical transport in the intracellular world. *Physical Biology*, 17(6):061003, October 2020.

[111] Melanie J. I. Müller, Stefan Klumpp, and Reinhard Lipowsky. Tug-of-war as a cooperative mechanism for bidirectional cargo transport by molecular motors. *Proc. Natl. Acad. Sci. U.S.A.*, 105(12):4609–4614, 2008.

[112] Melanie J.I. Müller, Stefan Klumpp, and Reinhard Lipowsky. Bidirectional transport by molecular motors: Enhanced processivity and response to external forces. *Biophys. J.*, 98(11):2610–2618, Jun 2010.

[113] S. R. Nelson, K. M. Trybus, and D. M. Warshaw. Motor coupling through lipid membranes enhances transport velocities for ensembles of myosin Va. *Proc. Natl. Acad. Sci. U.S.A.*, 111(38):E3986–E3995, 2014.

[114] C. M. O'Connor and J. U. Adams. *Essentials of cell biology*. NPG Education, Cambridge, MA, 2010.

[115] Guangshuo Ou, Oliver E. Blacque, Joshua J. Snow, Michel R. Leroux, and Jonathan M. Scholey. Functional coordination of intraflagellar transport motors. *Nature*, 436(7050):583–587, July 2005.

[116] Xiaoyu Pan, Guangshuo Ou, Gul Civelekoglu-Scholey, Oliver E. Blacque, Nicholas F. Endres, Li Tao, Alex Mogilner, Michel R. Leroux, Ronald D. Vale, and Jonathan M. Scholey. Mechanism of transport of IFT particles in C. elegans cilia by the concerted action of kinesin-II and OSM-3 motors . *Journal of Cell Biology*, 174(7):1035–1045, 09 2006.

[117] Itay Peker and Rony Granek. Multimotor Driven Cargos: From Single Motor under Load to the Role of Motor-Motor Coupling. *J. Phys. Chem. B*, 120(26):6319–6326, 2016.

[118] Thomas R. Powers, Greg Huber, and Raymond E. Goldstein. Fluid-membrane tethers: Minimal surfaces and elastic boundary layers. *Phys. Rev. E*, 65:041901, Mar 2002.

[119] Ashim Rai, Divya Pathak, Shreyasi Thakur, Shampa Singh, Alok Kumar Dubey, and Roop Mallik. Dynein clusters into lipid microdomains on phagosomes to drive rapid transport toward lysosomes. *Cell*, 164(4):722–734, February 2016.

[120] Sanghamitra Ray, Edgar Meyhöfer, Ronald A. Milligan, and Jonathon Howard. Kinesin follows the microtubule's protofilament axis. *Journal of Cell Biology*, 121(5):1083–1093, 1993.

[121] Babu J.N. Reddy, Suvranta Tripathy, Michael Vershinin, Marvin E. Tanenbaum, Jing Xu, Michelle Mattson-Hoss, Karim Arabi, Dail Chapman, Tory Doolin, Changbong Hyeon, and Steven P. Gross. Heterogeneity in kinesin function. *Traffic*, 18(10):658–671, 2017.

[122] Arthur R. Rogers, Jonathan W. Driver, Pamela E. Constantinou, D. Kenneth Jamison, and Michael R. Diehl. Negative interference dominates collective transport of kinesin motors in the absence of load. *Phys. Chem. Chem. Phys.*, 11(24):4800–4803, 2009.

[123] T. Roopa and G. V. Shivashankar. Nanomechanics of membrane tubulation and dna assembly. *Appl. Phys. Lett.*, 82(10):1631–1633, 2003.

[124] Vidur Sabharwal and Sandhya P. Koushika. Crowd Control: Effects of Physical Crowding on Cargo Movement in Healthy and Diseased Neurons. *Front Cell Neurosci*, 13:470, 10 2019.

[125] Niranjan Sarpangala and Ajay Gopinathan. Cargo surface fluidity can reduce inter-motor mechanical interference, promote load-sharing and enhance processivity in teams of molecular motors. *PLOS Computational Biology*, 18(6):1–32, 06 2022.

[126] Erik Schäffer, Simon F Nørrelykke, and Jonathon Howard. Surface forces and drag coefficients of microspheres near a plane surface measured with optical tweezers. *Langmuir*, 23(7):3654–3665, 2007.

[127] Manfred Schliwa. Molecular Motors. In *Encyclopedic Reference of Genomics and Proteomics in Molecular Medicine*, pages 1160–1174. Springer Berlin Heidelberg.

[128] Manfred Schliwa and Gunther Woehlke. Molecular motors. *Nature*, 422(17):759–765, 2003.

[129] Mark J. Schnitzer, Koen Visscher, and Steven M. Block. Force production by single kinesin motors. *Nat. Cell. Biol.*, 2(10):718–723, 2000.

[130] Arne Seitz and Thomas Surrey. Processive movement of single kinesins on crowded microtubules visualized using quantum dots. *EMBO J.*, 25(2):267–277, 2006.

[131] James R Sellers and Claudia Veigel. Walking with myosin v. *Curr. Opin. Cell Biol.*, 18(1):68 – 73, 2006. Cell structure and dynamics.

[132] Belongie Serge. Rodrigues' rotation formula.

[133] George T. Shubeita, Susan L. Tran, Jing Xu, Michael Vershinin, Silvia Cermelli, Sean L. Cotton, Michael A. Welte, and Steven P. Gross. Consequences of Motor Copy Number on the Intracellular Transport of Kinesin-1-Driven Lipid Droplets. *Cell*, 135(6):1098–1107, dec 2008.

[134] Joshua J. Snow, Guangshuo Ou, Amy L. Gunnarson, M. Regina S. Walker, H. Mimi Zhou, Ingrid Brust-Mascher, and Jonathan M. Scholey. Two anterograde intraflagellar transport motors cooperate to build sensory cilia on c. elegans neurons. *Nature Cell Biology*, 6(11):1109–1113, October 2004.

[135] Virupakshi Soppina, Arpan Kumar Rai, Avin Jayesh Ramaiya, Pradeep Barak, and Roop Mallik. Tug-of-war between dissimilar teams of microtubule motors regulates transport and fission of endosomes. *Proceedings of the National Academy of Sciences*, 106(46):19381–19386, November 2009.

[136] Karel Svoboda and Steven M. Block. Force and velocity measured for single kinesin molecules. *Cell*, 77(5):773–784, 1994.

[137] Anjneya Takshak, Nirvantosh Mishra, Aditi Kulkarni, and Ambarish Kunwar. Effect of fuel concentration on cargo transport by a team of kinesin motors. *Physica A: Statistical Mechanics and its Applications*, 467:395–406, 2017.

[138] Ivo A. Telley, Peter Bieling, and Thomas Surrey. Obstacles on the microtubule reduce the processivity of kinesin-1 in a minimal in vitro system and in cell extract. *Biophysical Journal*, 96(8):3341–3353, 2009.

[139] Marco Tjioe, Saurabh Shukla, Rohit Vaidya, Alice Troitskaia, Carol S Bookwalter, Kathleen M Trybus, Yann R Chemla, and Paul R Selvin. Multiple kinesins induce tension for smooth cargo transport. *eLife*, 8:e50974, oct 2019.

[140] Andrei A Tokarev, Aixa Alfonso, and Nava Segev. Overview of Intracellular Compartments and Trafficking Pathways. 2013.

[141] Mehmet Can Uçar and Reinhard Lipowsky. Collective force generation by molecular motors is determined by strain-induced unbinding. *Nano Letters*, 20(1):669–676, 2020. PMID: 31797672.

[142] Ronald D. Vale. The molecular motor toolbox for intracellular transport. *Cell*, 112(4):467–480, 2003.

[143] Claudia Veigel and Christoph F. Schmidt. Moving into the cell: single-molecule studies of molecular motors in complex environments. *Nature Reviews Molecular Cell Biology*, 12(3):163–176, February 2011.

[144] Michael Vershinin, Brian C. Carter, David S. Razafsky, Stephen J. King, and Steven P. Gross. Multiple-motor based transport and its regulation by Tau. *Proceedings of the National Academy of Sciences of the United States of America*, 104(1):87–92, 1 2007.

[145] Michael Vershinin, Brian C Carter, David S Razafsky, Stephen J King, and Steven P Gross. Multiple-motor based transport and its regulation by tau. *Proceedings of the National Academy of Sciences*, 104(1):87–92, 2007.

[146] Michael Vershinin, Jing Xu, David S. Razafsky, Stephen J. King, and Steven P. Gross. Tuning microtubule-based transport through filamentous maps: The problem of dynein. *Traffic*, 9(6):882–892, 2008.

[147] Koen Visscher, Mark J. Schnitzer, and Steven M. Block. Single kinesin molecules studied with a molecular force clamp. *Nature*, 400(6740):184–189, 1999.

[148] Hanumantha Rao Vutukuri, Masoud Hoore, Clara Abaurrea-Velasco, Lennard van Buren, Alessandro Dutto, Thorsten Auth, Dmitry A. Fedosov, Gerhard Gompper, and Jan Vermant. Active particles induce large shape deformations in giant lipid vesicles. *Nature*, 586(7827):52–56, September 2020.

[149] Malte Wachsmuth, Waldemar Waldeck, and Jörg Langowski. Anomalous diffusion of fluorescent probes inside living cell investigated by spatially-resolved fluorescence correlation spectroscopy. *Journal of Molecular Biology*, 298(4):677–689, 5 2000.

[150] Matthias Weiss, Markus Elsner, Fredrik Kartberg, and Tommy Nilsson. Anomalous subdiffusion is a measure for cytoplasmic crowding in living cells. *Biophysical Journal*, 87(5):3518–3524, 11 2004.

[151] John O. Wilson, David A. Quint, Ajay Gopinathan, and Jing Xu. Cargo diffusion shortens single-kinesin runs at low viscous drag. *Sci. Rep.*, 9(1):1–12, 2019.

[152] Jing Xu, Zhanyong Shu, Stephen J. King, and Steven P. Gross. Tuning Multiple Motor Travel via Single Motor Velocity. *Traffic*, 13(9):1198–1205, 2012.

[153] Saumya Yadav, Aritra Sen, and Ambarish Kunwar. Cargo transport properties are enhanced by cylindrical microtubule geometry and elliptical contact zone on cargo surface. *Journal of Theoretical Biology*, 565:111466, 2023.

[154] Junichiro Yajima, Maria C. Alonso, Robert A. Cross, and Yoko Y. Toyoshima. Direct Long-Term Observation of Kinesin Processivity at Low Load. *Curr. Biol.*, 12(4):301–306, 2002.

[155] Ahmet Yildiz, Michio Tomishige, Ronald D. Vale, and Paul R. Selvin. Kinesin walks hand-over-hand. *Science*, 303(5658):676–678, 2004.

[156] Yunxin Zhang. Cargo transport by several motors. *Phys. Rev. E*, 83(1):011909, 1 2011.